Terminal, Open-shell Mo Carbide and Carbyne Complexes: Spin Delocalization and Ligand Noninnocence

Gwendolyn A. Bailey, Joshua A. Buss, Paul H. Oyala, and Theodor Agapie

Division of Chemistry and Chemical Engineering, California Institute of Technology, 1200 E. California Blvd. MC 127-72, Pasadena CA 91125, USA

Supporting Information

EXPERIMENTAL DETAILS

General Considerations.

Unless otherwise specified, all operations were carried out in an MBraun glovebox under a N_2 atmosphere. Solvents for air- and moisture-sensitive reactions were dried over sodium benzophenone ketyl, or by the method of Grubbs.[1] Solvents, once dried and degassed, were vacuum-transferred prior to use and stored under an inert atmosphere over 4 Å molecular sieves. Carbides **1** and **1-$^{13}C_2$**,[2] methylidyne **2** and **2-$^{13}C_2$**,[2] silylcarbynes **3** and **3-$^{13}C_2$**,[3] and [Fc][$BAr^F{}_4$][4] were prepared according to literature procedures. Solutions of potassium naphthalenide ([K][$C_{10}H_8$]) were prepared in THF or 2-MeTHF by vigorously stirring solutions of naphthalene (30-50 mM) over a potassium mirror (ca. 1.2 equiv) for 1 h. Pre-reduced, Teflon-coated stir bars were prepared by stirring in naphthalenide solutions for 16 h followed by rinsing three times with THF. Pre-reduced stir bars were used in reactions involving [K][$C_{10}H_8$]. Attenuated total reflectance infrared (ATR-IR) spectra were collected on a Bruker Alpha II FTIR spectrometer equipped with an ATR sampling accessory house in an MBraun glovebox. Transmission IR spectra were collected on a Thermo Fischer Nicolet 6700 FTIR spectrometer. Elemental analysis was performed using a PerkinElmer 2400 Series II CHN Elemental Analyzer. ^{1}H, ^{13}C{^{1}H}, and ^{31}P{^{1}H} NMR spectra were recorded on a Varian 400 MHz spectrometer. ^{1}H and ^{13}C{^{1}H} NMR spectra are referenced to residual solvent peaks.[5] Multiplicities are abbreviated as follows: s = singlet, d = doublet, t = triplet, m = multiplet, br = broad.

Chart S1–Structures of open-shell carbide and carbyne complexes discussed. [a]

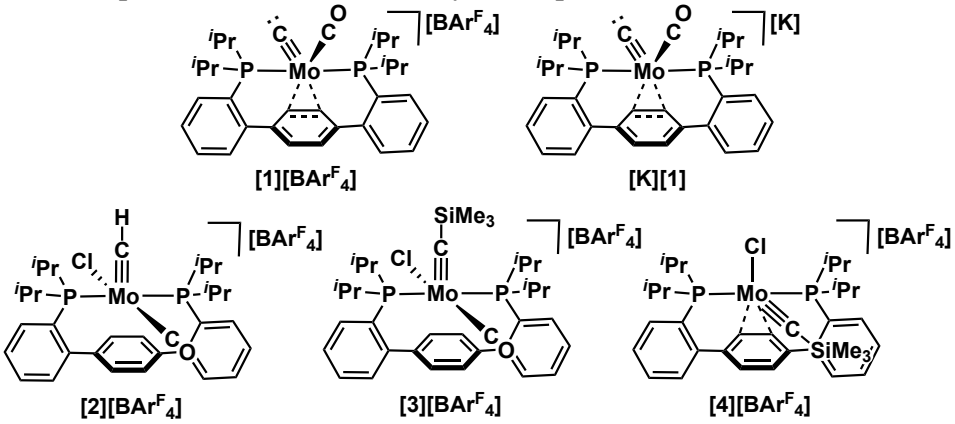

[a] The ^{13}C-labelled derivatives bear isotopic labels at the Mo≡C and CO positions.

Scheme S1–Synthesis of labelled 1-$^{13}C_2$, 2-$^{13}C_2$, and 3-$^{13}C_2$, precursors to [1-$^{13}C_2$][BAr^F_4]–[4-$^{13}C_2$][BAr^F_4] and [K][1-$^{13}C_2$]. Syntheses are reproduced from refs 2 and 3.

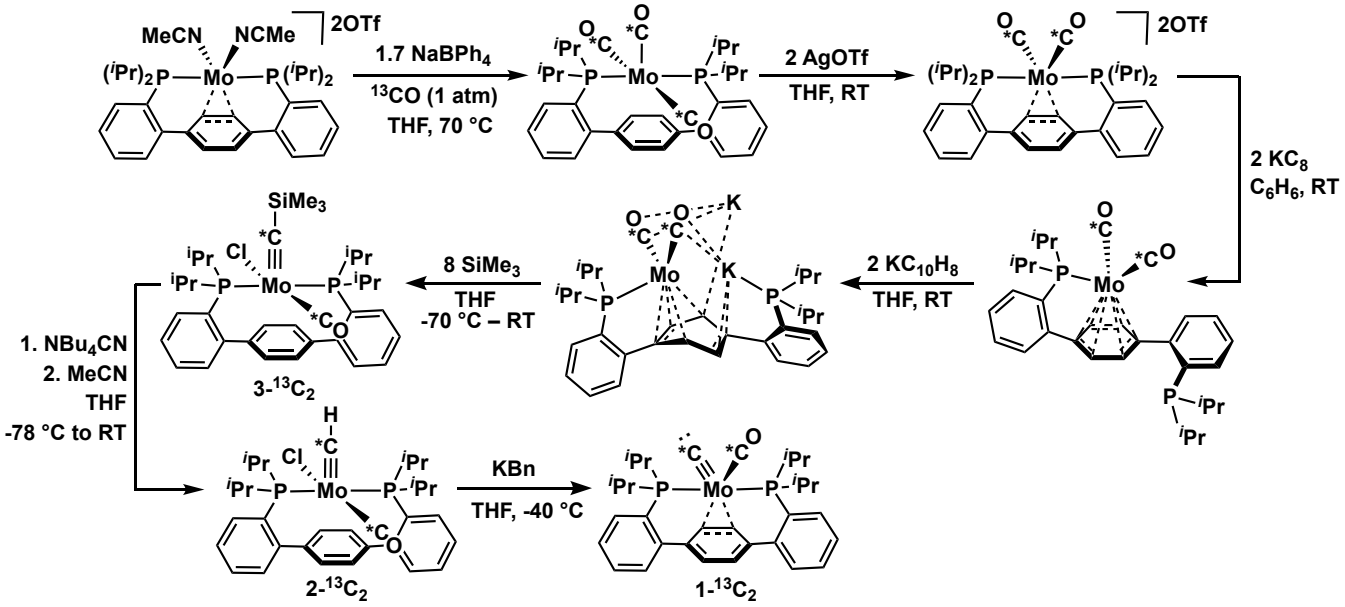

Synthesis of open-shell carbide and carbyne complexes.

Freeze-trapping of [1][BAr^F_4]. Stock solutions of [Fc][BAr^F_4] (49.6 mg, 0.047 mmol) in 2-MeTHF (0.50 mL) and carbide **1** (28.3 mg, 0.047 mmol) in 2-MeTHF (2.0 mL) were prepared. An aliquot of **1** (300 μL, 0.070 mmol, 1 equiv) was transferred to an X-band EPR tube and frozen in the glovebox cold well. Then, 75 μL of [Fc][BAr^F_4] solution (0.070 mmol, 1 equiv) was carefully and slowly dribbled down the inside of the pre-chilled EPR tube, such that the solution froze when or before reaching the bottom. The EPR tube was capped and quickly removed from the glovebox, taking care not to thaw the contents before freeze-trapping in a liquid N_2 bath. The contents were then briefly thawed in a –130 °C bath (pentane / liquid N_2), agitated briefly to mix, immersed for a further 30 s, and refrozen. Upon mixing of the two layers, a color change from red to deep brown was apparent. At this point, the X-band CW-EPR spectrum at 77 K revealed the expected S = ½ signal, which did not increase in intensity on immersing for longer periods at –130 °C. Solutions of **[1-$^{13}C_2$][BAr^F_4]** were prepared analogously starting from **1-$^{13}C_2$**. The extreme thermal sensitivity of **[1][BAr^F_4]** precluded its isolation as a solid.

Synthesis of [K][1]. To a thawing solution of **1** (30 mg, 0.047 mmol) in 2-MeTHF (1 mL) was added dropwise a solution of $KC_{10}H_8$ (0.50 mL of a 9.4 mM solution, 0.047 mmol, 1 equiv). An immediate color change from red to deep teal was apparent. The solution was quickly transferred to a pre-chilled X-band EPR tube, freeze-trapped, and analyzed. The X-band CW-EPR spectrum confirmed generation of the expected S = ½ signal. ^{1}H NMR (THF-h_8, 400 MHz, –10 °C): 7.78 (s, C_7H_8), 7.38 (s, C_7H_8), 7.34–6.97 (m), 2.30 (t), 2.25 (s), 1.34 (m), 1.26 (m), 1.14 (m), 0.93 (m), 0.85 (m). ^{31}P{^{1}H} NMR (THF-h_8, 162 MHz, –10 °C): silent. For analysis by single crystal XRD, 18-crown-6 (11.8 mg, 0.047 mmol, 1 equiv) was added as a thawing solution in 2-MeTHF (0.5 mL) following addition of $KC_{10}H_8$. An aliquot was removed for analysis by CW-EPR, confirming generation of the expected S = ½ signal. The signal appeared identical to that observed in the absence of 18-crown-6. The remaining solution was layered with cold pentane in an NMR tube. Slow mixing of the layers at –40 °C yielded brown, single crystalline blocks of **[K(18-**

crown-6)][1] amenable to analysis by XRD. **[K][1-$^{13}C_2$]** was prepared analogously starting from **1-$^{13}C_2$**. The thermal sensitivity of **[K][1]** precluded its isolation as a pure solid. Addition of thawing pentane to thawing solutions of **[K][1]** led to precipitation of a mixture of paramagnetic compounds, as judged by CW-EPR. Solutions for EPR analysis were therefore prepared freshly and not isolated.

Synthesis of [2][BAr$^F_4$]. To a thawing suspension of **2** (40 mg, 0.063 mmol) in 2-MeTHF (2 mL) was added dropwise a solution of [Fc][BAr$^F_4$] (66 mg, 0.063 mmol, 1 equiv) in 2-MeTHF (1 mL). The reaction mixture was allowed to warm gradually by stirring at ambient temperature for 2 min. During this time, the orange solids dissolved, and a color change to dark green-brown was observed. The reaction was transferred to the freezer (–40 °C) for 30 min, and then added dropwise in equal portions to rapidly stirring and thawing vials of pentane (4x20 mL). Decanting the pale orange solution, washing with cold pentane, and drying afforded **[2][BAr$^F_4$]** as a sticky green-brown solid (73 mg, 81%). ^{1}H NMR (THF-h$_8$, 400 MHz, 23 °C): 7.72 (s, [BAr$^F_4$]$^-$), 7.50 (s, [BAr$^F_4$]$^-$), 7.36 (br s). ^{31}P{^{1}H} NMR (THF-h$_8$, 162 MHz, 23 °C): silent. ^{19}F NMR (THF-h$_8$, 376 MHz, 23 °C): -61.5. ^{11}B NMR (THF-h$_8$, 128 MHz, 23 °C): -8.46 (s). IR (ATR, cm^{-1}): 2070. Elemental analysis results are consistent with retention of 1 equiv 2-MeTHF in the sticky solid. These signals are obscured in the ^{1}H NMR spectra by the solvent peaks. Anal. calcd (%) for $C_{64}H_{53}BClF_{24}MoOP_2 \bullet C_5H_{10}O$ (M_w = 1584.38): C, 52.31; H, 4.01. Found: C, 52.46; H, 3.89. Solid samples of **[2][BAr$^F_4$]** exhibit spontaneous CO loss at RT, and thus should be stored in the freezer (–40 °C). Single crystalline blocks of **[2][BAr$^F_4$]** were grown by vapor diffusion of hexanes into THF at –40 °C. Solid samples of **[2-$^{13}C_2$][BAr$^F_4$]** were prepared analogously starting from **2-$^{13}C_2$**.

Synthesis of [3][BAr$^F_4$]. To a thawing solution of **3** (50 mg, 0.071 mmol) in 2-MeTHF (0.5 mL) was added dropwise a solution of [Fc][BAr$^F_4$] (74 mg, 0.071 mmol, 1 equiv) in 2-MeTHF (0.5 mL). Upon addition of the oxidant, the light red color of **3** darkened to brown. The reaction mixture was allowed to warm gradually by stirring at ambient temperature for 2 min. Then, thawing pentane (20 mL) was added to precipitate a solid. Decanting, rinsing with thawing pentane (2x10 mL), and filtering afforded **[3][BAr$^F_4$]** as a free-flowing tan solid. Material prepared in this fashion contained little or no **[4][BAr$^F_4$]**, as judged by CW or pulse EPR. ^{1}H NMR (THF-h$_8$, 400 MHz, 23 °C): 7.72 (s, [BAr$^F_4$]$^-$), 7.51 (s, [BAr$^F_4$]$^-$) ppm. ^{31}P{^{1}H} NMR (THF-h$_8$, 162 MHz, 23 °C): silent. ^{19}F NMR (THF-h$_8$, 376 MHz, 23 °C): -61.5 ppm. ^{11}B NMR (THF-h$_8$, 128 MHz, 23 °C): -8.50 ppm (s). IR (transmission, thin film, cm^{-1}): 2049, 1971. IR (transmission, THF solution, cm^{-1}): 1967. **[3-$^{13}C_2$][BAr$^F_4$]** was prepared analogously starting from **3-$^{13}C_2$**. Anal. calcd (%) for $C_{67}H_{61}BClF_{24}MoOP_2Si$ (M_w = 1570.43): C, 51.24; H, 3.92. Found: C, 51.36; H, 3.86. Solid-state samples of **[3][BAr$^F_4$]** exhibit spontaneous CO loss at RT, and thus should be stored in the freezer (–40 °C). Brown, single-crystalline blades of **[3][BAr$^F_4$]** were grown by vapor diffusion of pentane into Et_2O at –40 °C.

Synthesis of [4][BAr$^F_4$]. To a thawing solution of **3** (200 mg, 0.282 mmol) in 2-MeTHF (8 mL) was added dropwise a thawing solution of [Fc][BAr$^F_4$] (297 mg, 0.282 mmol, 1 equiv) in 2-MeTHF (4 mL). Upon addition of the oxidant, a color change from light red to brown was observed. After warming to RT, volatiles were removed *in vacuo*, providing a maroon residue. The solids were triturated with Et_2O (4 mL) and pentane (4 mL), washed with hexanes (3 x 10 mL), and then dried in vacuo, providing dark red powder (394 mg, ~89%). The CW and pulse EPR data at this point reveal a mixture that contains both **[4][BAr$^F_4$]** and **[3][BAr$^F_4$]** (see Figure 8b in the main text, for example). Red single crystalline blocks of **[4][BAr$^F_4$]** were grown by vapor diffusion of pentane into a saturated Et_2O solution at –40 °C. XRD analysis of the

blocks reveals co-crystallization of **[4][BAr$^F_4$]** with [P2Mo(CH)(CO)][BAr$^F_4$] (20%), which was not observed spectroscopically and thus may be a product of disproportionation with **[3][BAr$^F_4$]**. Solid-state samples of **[4][BAr$^F_4$]** decompose to a mixture of species at RT (as judged by CW-EPR), and should therefore should be stored in the freezer (–40° C). A sample of **[4-^{13}C][BAr$^F_4$]**, prepared analogously from **3-$^{13}C_2$**, exhibited complete CO loss as judged by CW and pulse EPR spectroscopy. Elemental analysis of **[4][BAr$^F_4$]** was not attempted, owing to challenges in reproducibly obtaining samples that exhibit complete CO loss, without competing decomposition.

C–C coupling reactivity.

[K][1]$_2$[5]. A freshly prepared, thawing solution of **[K][1]** in 2-MeTHF (0.5 mL) was layered with thawing pentane (1 mL) and stored in the freezer at –40 °C for several days, during which time brown blocks crystallized. An X-ray diffraction study of the crystals identified **[K][1]$_2$[5]** as the product; however, the quality of the crystals was insufficient for reliable determination of bond metrics. The high thermal sensitivity of **[K][1]$_2$[5]** precluded recrystallization.

[K][6]. To a freshly-prepared, thawing solution of carbide **1** (0.048 mmol) in THF (1 mL) was added dropwise a solution of $KC_{10}H_8$ (0.048 mmol) in THF (1 mL). The solution was refrozen and set up to crystallize via vapor diffusion of pentane at –40 °C. An X-ray diffraction study identified the crystals as C–C coupled **[K][6].**

Electron Paramagnetic Resonance (EPR) Spectroscopy

CW-EPR spectroscopy. X-band CW-EPR spectra were obtained on a Bruker EMX spectrometer at a temperature of 77 K using a quartz liquid nitrogen immersion dewar on solutions prepared as frozen glasses in 2-MeTHF, unless otherwise noted.

Pulse EPR spectroscopy. All pulse EPR and electron nuclear double resonance (ENDOR) experiments were acquired using a Bruker (Billerica, MA) ELEXSYS E580 pulse EPR spectrometer. All X-band data was acquired using a Bruker MD-4 resonator, while Q-band data was acquired using a Bruker D2 resonator. Temperature control was achieved using an ER 4118HV-CF5-L Flexline Cryogen-Free VT cryostat manufactured by ColdEdge (Allentown, PA) equipped with an Oxford Instruments Mercury ITC.

Pulse X- and Q-band ENDOR was acquired using the Davies pulse sequence ($\pi - T_{RF} - \pi_{RF} - T_{RF} - \pi/2 - \tau - \pi -$ echo), where T_{RF} is the delay between mw pulses and RF pulses, π_{RF} is the length of the RF pulse and the RF frequency is randomly sampled during each pulse sequence.

X and Q-band HYSCORE spectra were acquired using the 4-pulse sequence ($\pi/2 - \tau - \pi/2 - t_1 - \pi - t_2 - \pi/2 -$ echo), where τ is a fixed delay, while t_1 and t_2 are independently incremented by Δt_1 and Δt_2, respectively. The time domain data was baseline-corrected (third-order polynomial) to eliminate the exponential decay in the echo intensity, apodized with a Hamming window function, zero-filled to eight-fold points, and fast Fourier-transformed to yield the 2-dimensional frequency domain. Contour plots of the 2D frequency spectra are plotted in logarithmic scale, with contours plotted in colors ranging from blue → yellow → red in increasing intensity.

In general, the ENDOR spectrum for a given nucleus with spin I= ½ (^{1}H, ^{13}C, ^{31}P) coupled to the S = ½ electron spin exhibits a doublet at frequencies

$$\nu_{\pm} = \left|\frac{A}{2} \pm \nu_N\right| \quad (1)$$

Where ν_N is the nuclear Larmor frequency and A is the hyperfine coupling. For nuclei with $I \geq 1$ (^{14}N, ^{2}H), an additonal splitting of the $\nu_{\pm}$ manifolds is produced by the nuclear quadrupole interaction (P)

$$\nu_{\pm,m_I} = \left|\nu_N \pm \frac{3P(2m_I - 1)}{2}\right| \quad (2)$$

In HYSCORE spectra, these signals manifest as cross-peaks or ridges in the 2-D frequency spectrum which are generally symmetric about the diagonal of a given quadrant. This technique allows hyperfine levels corresponding to the same electron-nuclear submanifold to be differentiated, as well as separating features from hyperfine couplings in the weak-coupling regime ($|A| < 2|\nu_I|$) in the (+,+) quadrant from those in the strong coupling regime ($|A| > 2|\nu_I|$) in the (−,+) quadrant. The (−,−) and (+,−) quadrants of these frequency spectra are symmetric to the (+,+) and (−,+) quadrants, thus only two of the quadrants are typically displayed in literature.

For systems with appreciable hyperfine anisotropy in frozen solutions or solids, HYSCORE spectra typically do not exhibit sharp cross peaks, but show ridges that represent the sum of cross peaks from selected orientations within the excitation bandwidth of the MW pulses at the magnetic field position at which the spectrum is collected. The length and curvature of these correlation ridges can allow for the separation and estimation of the magnitude of the isotropic and dipolar components of the hyperfine tensor, as shown in Fig. S1.

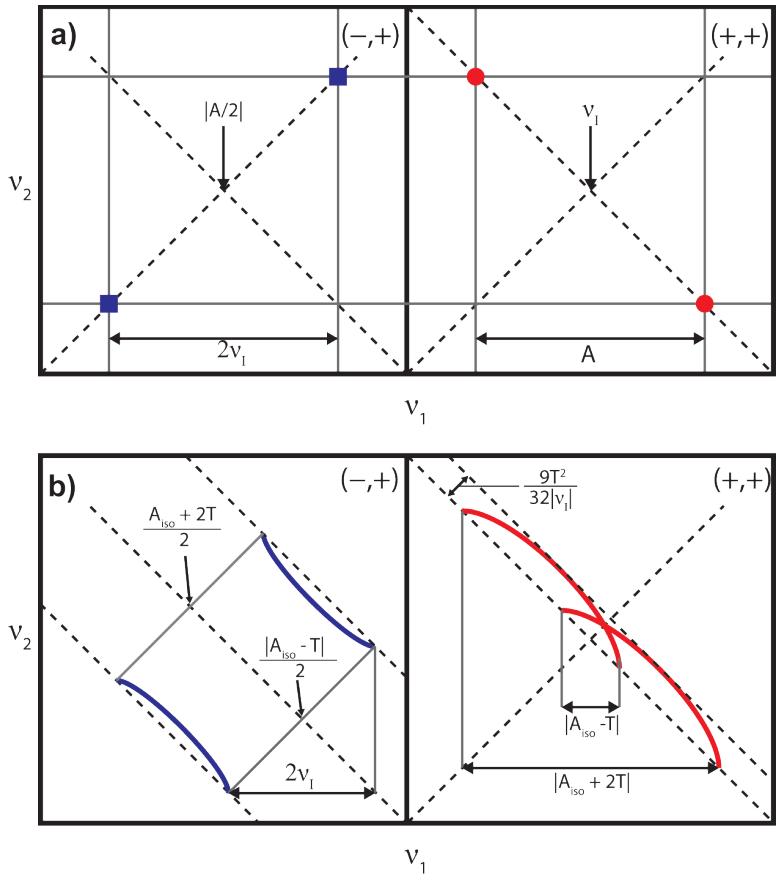

Figure S1—a) HYSCORE powder patterns for an $S = ½$, $I = ½$ spin system with an isotropic hyperfine tensor A. b) HYSCORE powder patterns foran $S = ½$, $I = ½$ spin system with an axial hyperfine tensor that contains isotropic (a_{iso}) and dipolar (T) contributions. Blue correlation ridges represent the strong coupling case; red correlation ridges represent the weak coupling case.

EPR Simulations. Simulations of all CW and pulse EPR data were achieved using the EasySpin simulation toolbox (release 5.2.25)[6] with Matlab 2019a using the following Hamiltonian:

$$\hat{H} = \mu_B \vec{B}_0 g \hat{S} + \mu_N g_N \vec{B}_0 \hat{I} + h\hat{S} \cdot \boldsymbol{A} \cdot \hat{I} + h\hat{I} \cdot \boldsymbol{P} \cdot \hat{I} \qquad (3)$$

In this expression, the first term corresponds to the electron Zeeman interaction term where μ_B is the Bohr magneton, g is the electron spin g-value matrix with principal components g = [g_{xx} g_{yy} g_{zz}], and $\hat{S}$ is the electron spin operator; the second term corresponds to the nuclear Zeeman interaction term where μ_N is the nuclear magneton, g_N is the characteristic nuclear g-value for each nucleus (e.g. ^{1}H, ^{13}C, ^{31}P) and $\hat{I}$ is the nuclear spin operator; the third term corresponds to the electron-nuclear hyperfine term, where $\boldsymbol{A}$ is the hyperfine coupling tensor with principal components $\boldsymbol{A}$ = [A_{xx}, A_{yy}, A_{zz}]; and for nuclei with $I \geq 1$, the final term corresponds to the nuclear quadrupole (NQI) term which arises from the interaction of the

nuclear quadrupole moment with the local electric field gradient (efg) at the nucleus, where $\boldsymbol{P}$ is the quadrupole coupling tensor. In the principal axis system (PAS), $\boldsymbol{P}$ is traceless and parametrized by the quadrupole coupling constant e^2Qq/h and the asymmetry parameter η such that:

$$\boldsymbol{P} = \begin{pmatrix} P_{xx} & 0 & 0 \\ 0 & P_{yy} & 0 \\ 0 & 0 & P_{zz} \end{pmatrix} = \frac{e^2Qq/h}{4I(2I-1)} \begin{pmatrix} -(1-\eta) & 0 & 0 \\ 0 & -(1+\eta) & 0 \\ 0 & 0 & 2 \end{pmatrix} \qquad (4)$$

where $\frac{e^2Qq}{h} = 2I(2I-1)P_{zz}$ and $\eta = \frac{P_{xx}-P_{yy}}{P_{zz}}$. The asymmetry parameter may have values between 0 and 1, with 0 corresponding to an electric field gradient (EFG) with axial symmetry and 1 corresponding to a fully rhombic EFG.

The orientations between the hyperfine and NQI tensor principal axis systems and the g-matrix reference frame are defined by the Euler angles (α, β, γ), with rotations performed within the zyz convention where α rotates xyz counterclockwise about z-axis to give x'y'z', β rotates x'y'z counterclockwise about y'-axis to give x",y",z", γ rotates xyz counterclockwise about z"-axis to give final frame orientation.

Estimation of spin density from hyperfine coupling parameters. Each hyperfine coupling tensor can be considered as the sum of an isotropic term, a_{iso}, which is the average value of the three principal components of the hyperfine tensor, and an anisotopic term, $\boldsymbol{T}_{obs}$. These hyperfine values can be compared to calculated hyperfine values for a unit of spin in an s, p, or d orbital in order to obtain an estimate of the spin density at the nucleus in question.

Decomposition of the $^{95/97}$Mo and ^{13}C hyperfine tensors and estimation of the spin density

[1][BAr$^F_4$]: The $^{95/97}$Mo hyperfine coupling can be decomposed into A(^{95}Mo) = [86, 86, 154] = a_{iso} + A_{aniso} = 109 + [-23, -23, 47] MHz. Comparing to $|a_{iso}{}^0(^{95}\text{Mo})|$ = 1984 MHz, a_{iso} = 109 corresponds to a small 5s orbital density on Mo of $\rho_s \sim 0.05$ e$^-$. This is unsurprising considering that the majority of the unpaired spin resides in a valence orbital of d_{xy} parentage, giving rise to the sizeable dipolar component. Taking a unit of unpaired spin in a d_{xy} orbital of Mo $\mathbf{A}_{dxy}{}^0$ = [-43.1, -43.1, 86.2], the anisotropic term $\boldsymbol{A}_{aniso}(^{95}\text{Mo})$ = [-23, -23, 47] corresponds to a $4d_{xy}$ orbital spin density of $\rho_{dxy} \sim 0.53$ e$^-$. Between these two contributions, the total spin density at Mo is estimated to be $\rho_{Mo} \sim 0.58$ e$^-$, in good agreement with the DFT-predicted Löwdin spin density of 0.55 e$^-$.

The anisotropic ^{13}C hyperfine coupling tensors for the carbide and ^{13}CO ligands can likewise be decomposed following the procedures of Hoffman and coworkers. It is not initially known which hyperfine tensor corresponds to which ^{13}C nucleus, however, and so both possibilities must be considered in turn. Assuming first assume that A(^{13}C) = [15, 11, 9] corresponds to the carbide ligand, we decompose this anisotropic tensor into its constituent *s*- and *p*-orbital origins:

$$A(^{13}\text{C}) = [15, 11, 9]$$

$$= a_{iso} + \boldsymbol{T}_{obs}$$

$$= 11.7 + [3.3, -0.7, -2.7]$$

Taking $a_{iso}^0(^{13}C) = 3777$ MHz for a single electron in a 2*s* orbital, the isotropic hyperfine $a_{iso}(^{13}C) = 11.7$ MHz corresponds to a small 2s orbital density on the carbide of $\rho_s \sim 0.003$ e$^-$, indicating that the terminal carbide can be treated as having a filled 2s orbital with little hybridization with p-orbitals containing the unpaired spin density.

The remaining dipolar term $\boldsymbol{T}_{obs}$ can be decomposed into two separate axial contributions: one local contribution, $\boldsymbol{T}^{x,y}_{loc}$, from spin density at C with its unique axis along an axis (x or y) orthogonal to the Mo–C bond vector, and a second component, $\boldsymbol{T}^{z}_{obs}$, with its unique axis parallel to the Mo–C bond vector. In turn, $\boldsymbol{T}^{z}_{obs}$ is a composite of the nonlocal contribution ($\boldsymbol{T}^{z}_{nloc}$) due to the through-space dipolar interaction between the ^{13}C nucleus and unpaired spin density at the Mo nucleus, and a local contribution ($\boldsymbol{T}^{z}_{loc}$) from spin density at C in a p orbital with its unique axis parallel to the Mo–C bond vector. The nonlocal contribution $\boldsymbol{T}^{z}_{nloc}$ can be estimated using the point-dipole approximation, with the unique axis parallel to the Mo–C axis in the molecular frame:

$$\boldsymbol{T}^{z}_{nloc} = [-a, -a, 2a]; \;\; a = \frac{\rho_{Mo} g_e \mu_b g_n \mu_n}{r^3}$$

Using r = 1.75 Å (the average Mo≡C distance determined crystallographically for the carbyne complexes **[2][BAr$^F_4$]**–**[4][BAr$^F_4$]**) and $\rho_{Mo} \sim 0.58$ e$^-$ determined from the previous section, we find that $\boldsymbol{T}^{z}_{nloc}$ = [–2.2, –2.2, 4.5] MHz. Subtraction of this nonlocal contribution $\boldsymbol{T}^{z}_{nloc}$ from $\boldsymbol{T}_{obs}$ yields the sum of the local contributions:

$$\boldsymbol{T}_{loc} = \boldsymbol{T}_{obs} - \boldsymbol{T}^{z}_{nloc}$$

$$= [5.6, 1.6, -7.1]$$

$\boldsymbol{T}_{loc}$ can be decomposed in turn into two orthogonal axis vectors. Two solutions exist, where $\boldsymbol{T}^{z}_{loc}$ = [–4.2, –4.2, 8.4] and $\boldsymbol{T}^{x,y}_{loc}$ = [–1.3, 2.6, –1.3], or $\boldsymbol{T}^{x}_{loc}$ = [8.4, –4.2, –4.2] and $\boldsymbol{T}^{y}_{loc}$ = [–2.9, 5.8, –2.9]. In the first case, considering a single unit of unpaired spin in the p_y orbital of ^{13}C corresponding to $\boldsymbol{A}^0_{py}$ = [–107.4, 214.8, –107.4], $\boldsymbol{T}^{x,y}_{loc}$ corresponds to a *p*-orbital spin density of $\rho_{py} \sim 0.039$ e$^-$, while $\boldsymbol{T}^{z}_{loc}$ corresponds to a p_z-orbital spin density parallel to the Mo–C axis of $\rho_{pz} \sim 0.012$ e$^-$, for a total spin density (including ρ_s) of ~0.055 e$^-$ distributed primarily across the two p orbitals. In the second case, applying a similar analysis again yields $\rho_{px} \sim 0.039$ e$^-$ and $\rho_{py} \sim 0.027$ e–, for a total spin density of ~0.07 e$^-$. These two solutions are in reasonable agreement with the DFT-computed Löwdin spin population of –0.07 e$^-$.

Proceeding next with A(^{13}C) = [8, 22, 8], we likewise assume that this vector corresponds to the ^{13}CO ligand, which points ~90° perpendicular to the carbide ligand, in the x or y direction of the molecular frame. Both of these two orientations must be considered. The mathematical treatment for this tensor proceeds identically to that for the carbide above, only $\boldsymbol{T}^{z}_{nloc}$ extends either in the x or y direction, respectively, such that $\boldsymbol{T}^{z}_{nloc} = [2a, -a, -a]$ or $\boldsymbol{T}^{z}_{nloc} = [-a, 2a, -a]$, respectively. For calculation of the constant *a*, the average Mo–CO bond distance for **[2][BAr$^F_4$]**–**[4][BAr$^F_4$]** is applied (r = 2.10 Å).

$$A(^{13}C) = [8, 22, 8]$$

$$= a_{iso} + \boldsymbol{T}_{obs}$$

$$= 12.7 + [-4.7, 9.3, -4.7]$$

$\boldsymbol{T}^{z}_{nloc} = [2a, -a, -a]$
= [2.6, -1.3, -1.3]
$\boldsymbol{T}_{loc} = \boldsymbol{T}_{obs} - \boldsymbol{T}^{z}_{nloc}$
= [–7.3, 10.6, –3.4]

Solution 1:
= [–1.3, –1.3, 2.6]
= [–6.0, 12.1, –6.0]
ρ_{pz} ~ 0.012 e⁻ and ρ_{px} ~ 0.056 e⁻

Solution 2:
= [–1.3, –1.3, 2.6]
= [–6.0, 12.1, –6.0]
ρ_{px} ~ 0.012 e⁻ and ρ_{px} ~ 0.043 e⁻

$\boldsymbol{T}^{z}_{nloc} = [-a, 2a, -a]$
= [-1.3, 2.6, -1.3]
$\boldsymbol{T}_{loc} = \boldsymbol{T}_{obs} - \boldsymbol{T}^{z}_{nloc}$
= [–3.4, 6.7, –3.4]

ρ_{py} ~ 0.012 e⁻

$\boldsymbol{T}^{z}_{nloc} = [2a, -a, -a]$ yields two solutions that are in reasonable agreement with the DFT-predicted Löwdin spin population for ^{13}CO of 0.06–0.07 e⁻. Likewise, moving onto the ^{31}P nuclei (A(^{31}P1) = [56, 65, 62]), treating this nucleus as if the Mo–P bond extends orthogonally to the Mo–CO bond in the y direction yields a reasonable spin density of 0.010–0.015 e⁻ (computed Löwdin spin population 0.03 e⁻). Therefore, while we cannot rule out the opposite scenario, we favor an interpretation where the Mo–CO bond extends in the y direction, and the Mo–P bonds are placed along the x axis.

Considering next the alternative scenario whereby A(^{13}C) = [8, 22, 8] corresponds to the carbide ligand and A(^{13}C) = [15, 11, 9] corresponds to the ^{13}CO ligand, and pursuing the same mathematical treatment as above, we find solutions whereby ρ_{tot} (carbide) = 0.07–0.09 e⁻,while ρ_{tot} (^{13}CO) = 0.05 e⁻, this time with the Mo–CO ligand extending in the y direction. Treatment of the ^{31}P hyperfine tensor as if the Mo–P bond extends in the x direction, we again find a reasonable spin density of 0.02-0.025 e⁻.

[3][BAr$^{F}_{4}$], [4][BAr$^{F}_{4}$], and [K][1]: The same mathematical treatment was applied as above. The results are presented in Table S1 below.

Table S1—Hyperfine coupling tensors in MHz measured for open-shell carbide complexes [1][BAr$^{F}_{4}$] and [K][1] along with the corresponding spin populations.

		EPR								
Complex		A_x	A_y	A_z	a_{iso}	T_{obs}			ρ (e⁻)	**orbital**[d]
[1][BAr$^{F}_{4}$]	**$^{95/97}$Mo1**	86	86	154	109	-23	-23	45	0.58	91% d_{xy}
	^{31}P1	75	80	52	69	6	11	-17	-	-
	^{31}P2	45	58	50	51	-6	7	-1	-	-
	$^{13}C_A$	15	11	9	11.7	3	-1	-2	0.06-0.09[a]	>95% p
	$^{13}C_B$	8	22	8	12.7	-5	9	-5	0.05-0.07[b]	>95% p

[K][1]	**$^{95/97}$Mo1**	46	46	59	50.3	-4	-4	9	0.13	80% d_{xy}
	^{31}P1	8.4	3.6	3.6	5.2	3.2	-1.6	-1.6	-	-
	^{31}P2	8.4	3.6	3.6	5.2	3.2	-1.6	-1.6	-	-
	^{13}C31	-0.05	-0.05	4.5	1.5	-1.55	-1.55	3.0	0.06-0.09	>95% p
	^{13}C32	4.6	5.5	5.5	5.2	-0.6	0.3	0.3	0.05-0.07	>95% p

[a] Estimated spin density for the carbide C31. [b] Estimated spin density for the CO ligand C32. [c]Hyperfine coupling parameters were determined through simulations of the CW-EPR spectra - Davies ENDOR and HYSCORE experiments were not performed for this complex. [d] Proportion of localized spin density in d or p orbitals on each nucleus.

Table S2—Hyperfine coupling tensors in MHz measured for open-shell carbyne complexes [2][BAr$^{F}_{4}$], [3][BAr$^{F}_{4}$], and [4][BAr$^{F}_{4}$] along with the corresponding spin populations.

		EPR								
Complex		A_x	A_y	A_z	A_{iso}	T_{obs}			ρ (e^-)	**orbital[d]**
[2][BAr$^{F}_{4}$][c]	**$^{95/97}$Mo1**	95	75	155	107	-12	-32	48	-	-
	^{31}P1	35	72	20	42	-7	30	-22	-	-
	^{31}P2	46	35	20	34	12	1	-14	-	-
	$^{13}C_A$	24	30	20	24	-1	5	-4.7	-	-
	$^{13}C_B$	40	20	35	32	8.3	-12	3.3	-	-
[3][BAr$^{F}_{4}$]	**$^{95/97}$Mo1**	86	86	165	110	-24	-24	55	0.64	91% d_{xy}
	^{31}P1	16	40	9	22	-6	18	-13	-	-
	^{31}P2	9	50	16	22	-13	28	6	-	-
	$^{13}C_A$	27.5	27.5	22.5	26	1.5	1.5	-3.5	0.05-0.07[a]	>85% p
	$^{13}C_B$	31	18	33	27	4	-9	6	0.02-0.24[b]	>87% p
[4][BAr$^{F}_{4}$]	**$^{95/97}$Mo1**	100	100	190	130	-30	-30	60	0.77	91% d_{xy}
	^{31}P1	60	70	60	63	-3	7	-3	-	-
	^{31}P2	60	70	60	63	-3	7	-3	-	-
	^{13}C31	31	31	17	26	5	5	-9	0.08	91% p_z

SPECTRA

EPR spectra
CW-EPR spectra

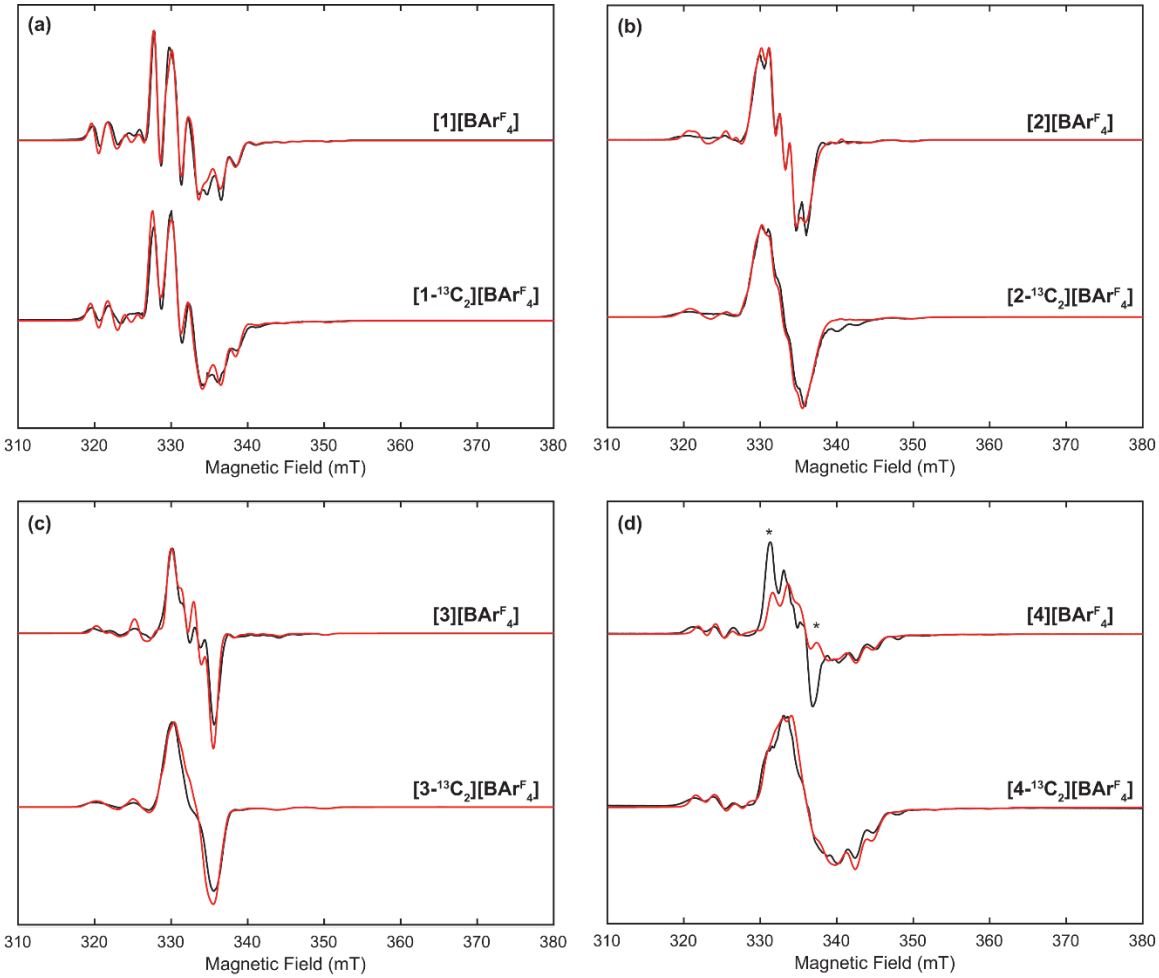

Figure S2—X-band CW-EPR spectra (black) of oxidized natural abundance (top) and ^{13}C-labelled (bottom) complexes at a temperature of 77 K with spectral simulations overlaid (red) using parameters in Table 2. Asterisks above **[4][BAr$^F_4$]** indicate features associated with residual **[3][BAr$^F_4$]** due to incomplete CO loss. Acquisition parameters: MW frequency = 9.324 – 9.385 GHz; MW power = 200 μW; modulation amplitude = 0.2 mT; conversion time = 82 ms.

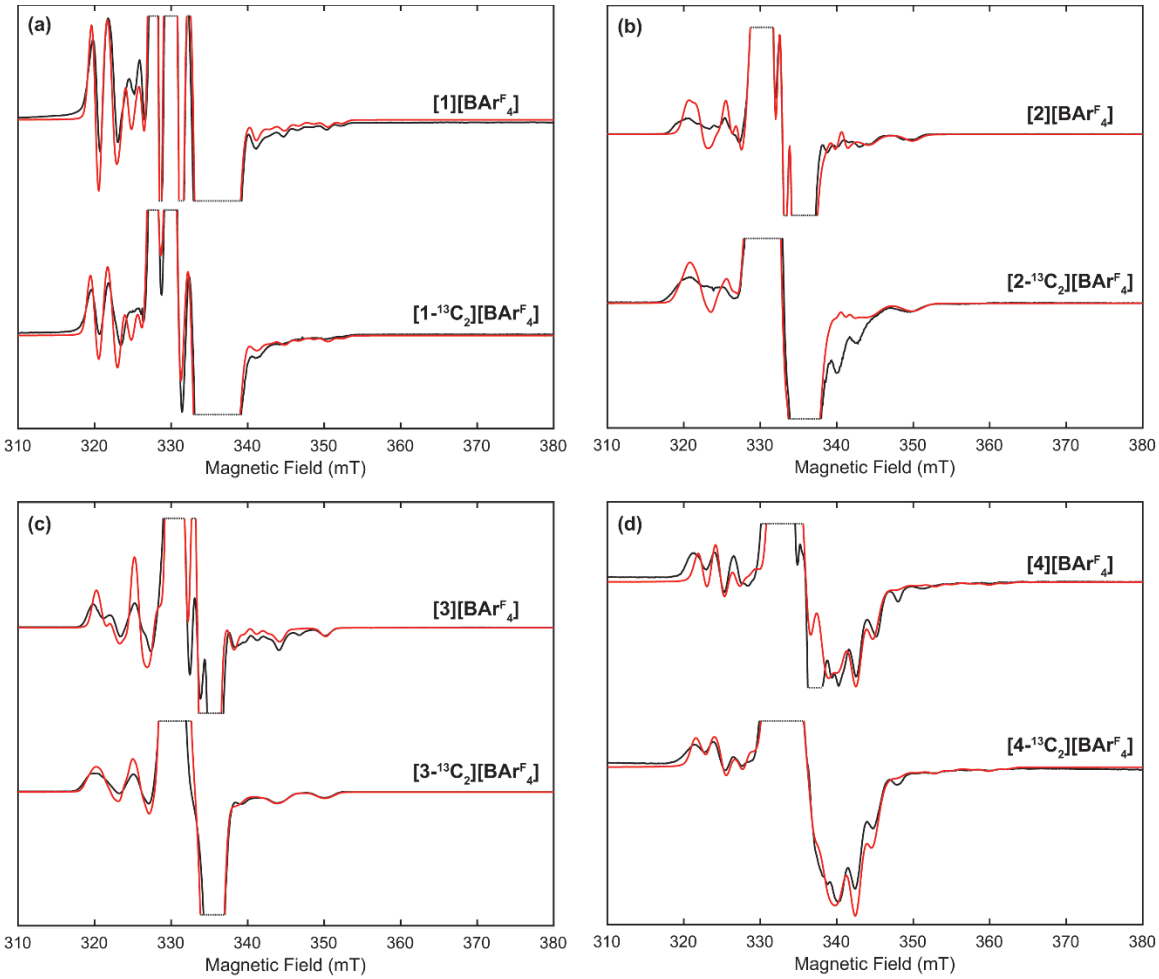

Figure S3—X-band CW-EPR spectra zoomed in on Mo hyperfine satellite peaks (black) of oxidized natural abundance (top) and ^{13}C-labelled (bottom) complexes at a temperature of 77 K with spectral simulations overlaid (red) using parameters in Table 2. Asterisks above **[4][BAr$^F_4$]** indicate features associated with residual **[3][BAr$^F_4$]** due to incomplete CO loss. Acquisition parameters: MW frequency = 9.324 – 9.385 GHz; MW power = 200 μW; modulation amplitude = 0.2 mT; conversion time = 82 ms.

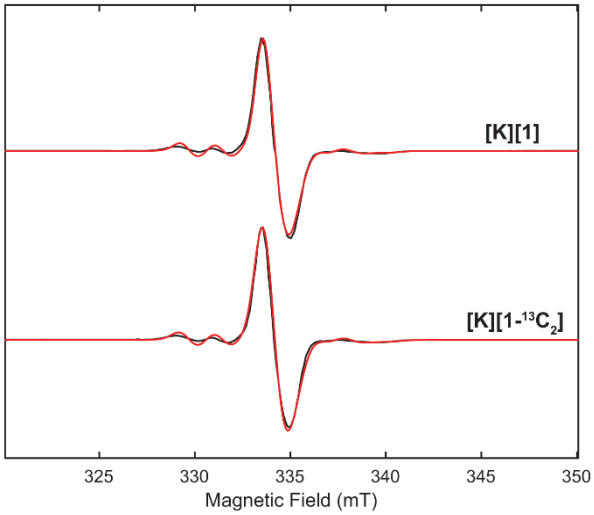

Figure S4—X-band CW-EPR spectra (black) of **[K][1]** with natural abundance (top) and **[K][1-$^{13}C_2$]** (bottom) at a temperature of 77 K with spectral simulations overlaid (red) using parameters in Table 2. Acquisition parameters: MW frequency = 9.366 GHz; MW power = 20 μW; modulation amplitude = 0.2 mT; conversion time = 82 ms.

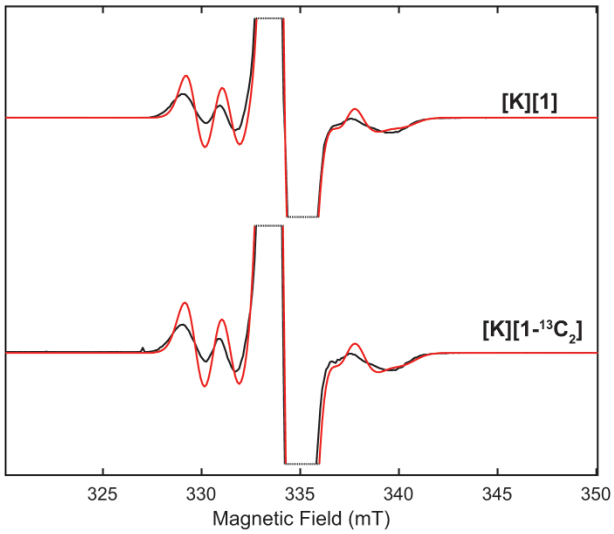

Figure S5—X-band CW-EPR spectra zoomed in on Mo hyperfine satellite peaks (black) of **[K][1]** with natural abundance (top) and **[K][1-$^{13}C_2$]** (bottom) at a temperature of 77 K with spectral simulations overlaid (red) using parameters in Table 2. Acquisition parameters: MW frequency = 9.366 GHz; MW power = 20 μW; modulation amplitude = 0.2 mT; conversion time = 82 ms.

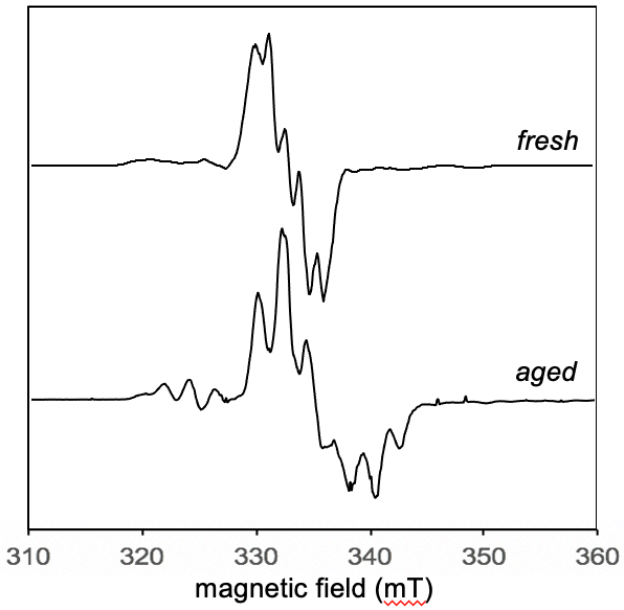

Figure S6—77 K X-band EPR spectra of (top) freshly prepared **[2][BAr$^{F}_{4}$]** and (bottom) an aged sample (stored in the solid state at RT for weeks). An accompanying change in color from green (top) to purple (bottom) is observed. For the corresponding IR spectra, see Figure S32.

Davies ENDOR and HYSCORE spectra

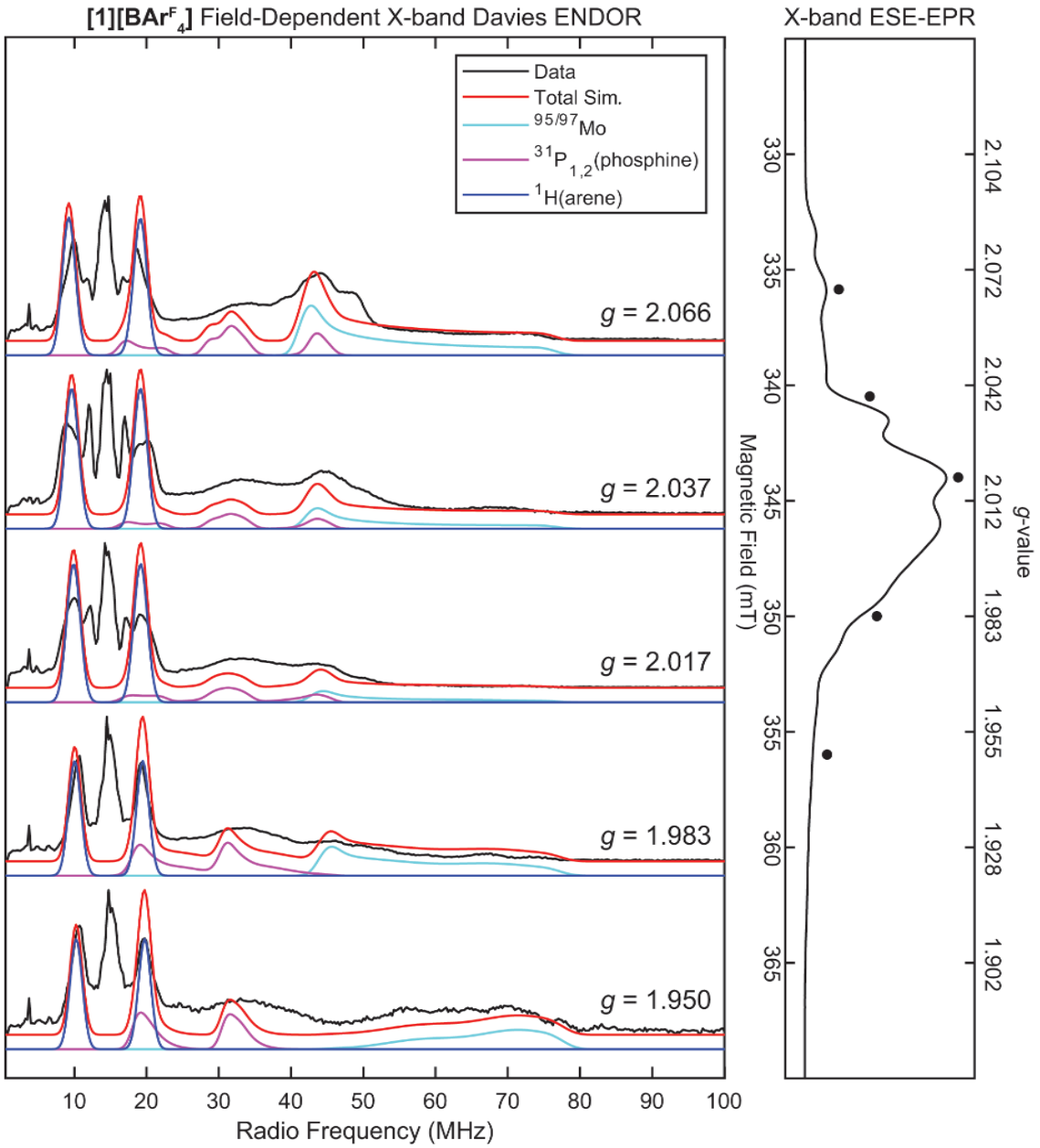

Figure S7—Field-Dependent X-band Davies ENDOR spectra of natural abundance **[1][BAr$^{F}_{4}$]** (black) with simulations overlaid using parameters in Table 2. The electron spin echo (ESE) detected EPR spectrum is shown to the right, with fields at which ENDOR was acquired denoted with black circles. Acquisition parameters: temperature = 25 K; MW frequency = 9.716 GHz; MW π pulse length = 80 ns; interpulse delay τ = 240 ns; π_{RF} pulse length = 15 μs; T_{RF} delay = 2 μs; shot repetition time (srt) = 5 ms. Duplicated from Figure 2 in the main text for the reader's convenience.

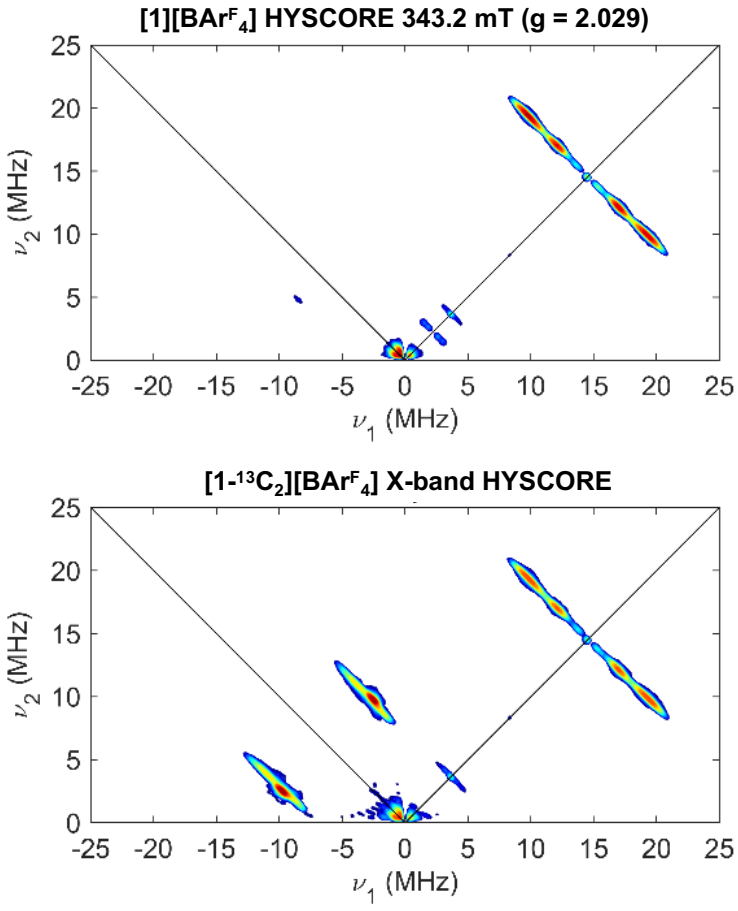

Figure S8—(Top) X-band HYSCORE of natural abundance **[1][BAr$^{F}_{4}$]** collected at 340.8 mT (g = 2.044). (Bottom) X-band HYSCORE of **[1-$^{13}C_2$][BAr$^{F}_{4}$]** collected at 340.8 mT (g = 2.044). Acquisition parameters: temperature = 25 K; MW frequency = 9.715 GHz; MW pulse length ($\pi/2$, π) = 8 ns, 16 ns; τ = 136 ns; $t_1 = t_2$ = 100 ns; $\Delta t_1 = \Delta t_2$ =16 ns; shot repetition time (srt) = 3 ms.

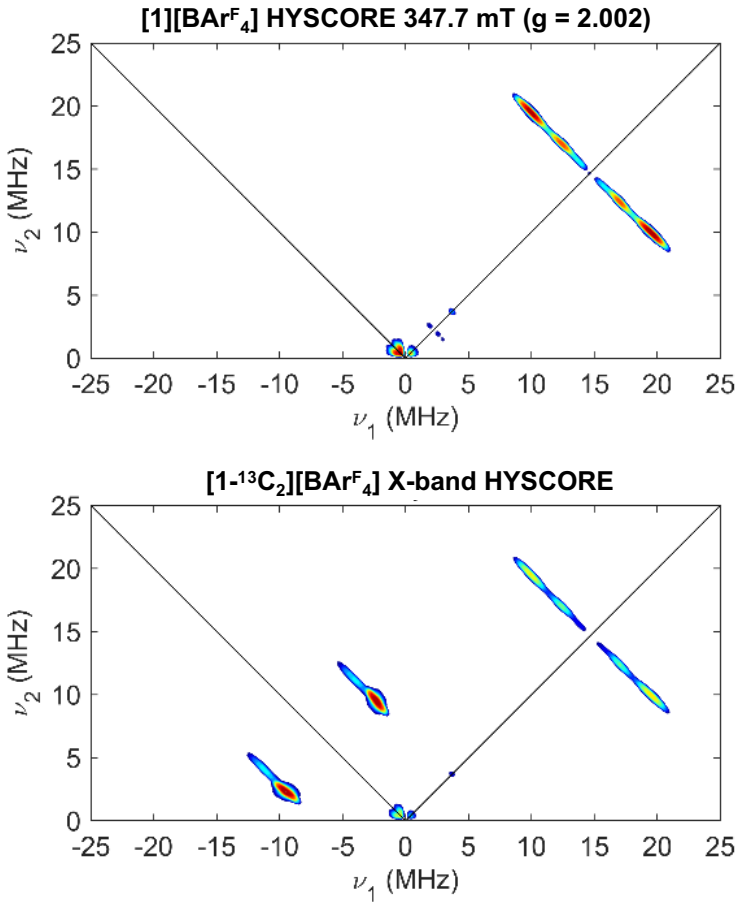

Figure S9—(Top) X-band HYSCORE of natural abundance **[1][BAr$^{F}_{4}$]** collected at 344.2 mT (g = 2.024). (Bottom) X-band HYSCORE of **[1-^{13}C$_2$][BAr$^{F}_{4}$]** collected at 344.2 mT (g = 2.024). Acquisition parameters: temperature = 25 K; MW frequency = 9.715 GHz; MW pulse length ($\pi/2$, π) = 8 ns, 16 ns; τ = 136 ns; $t_1 = t_2$ = 100 ns; $\Delta t_1 = \Delta t_2$ =16 ns; shot repetition time (srt) = 3 ms.

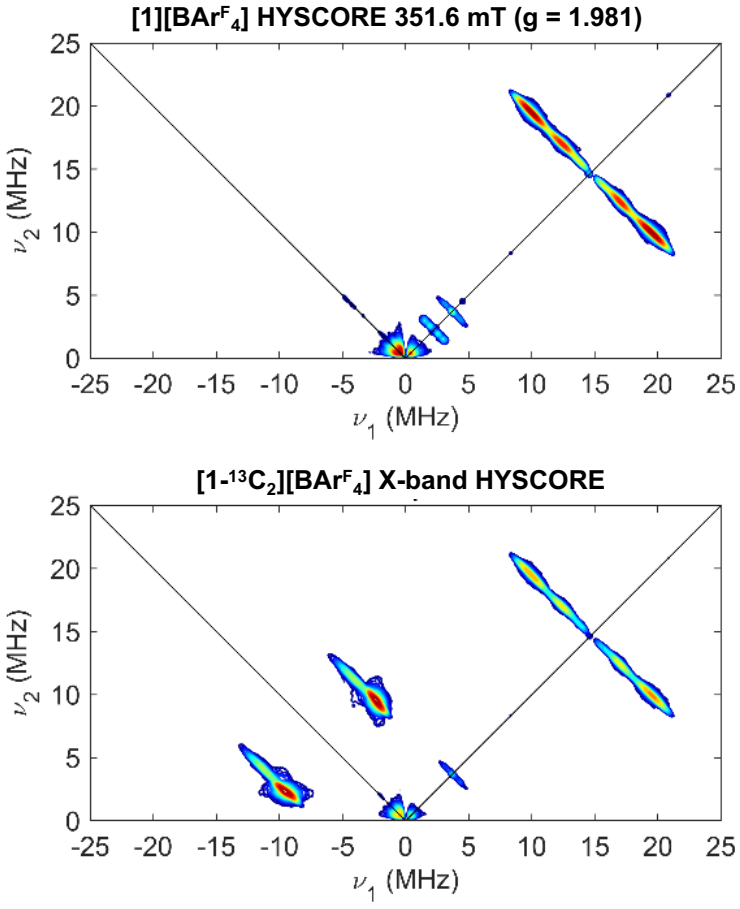

Figure S10—(Top) X-band HYSCORE of natural abundance **[1][BAr$^F_4$]** collected at 350.0 mT (g = 1.991). (Bottom) X-band HYSCORE of **[1-$^{13}C_2$][BAr$^F_4$]** collected at 350.0 mT (g = 1.991)**.** Acquisition parameters: temperature = 25 K; MW frequency = 9.715 GHz; MW pulse length ($\pi/2$, π) = 8 ns, 16 ns; τ = 136 ns; $t_1 = t_2$ = 100 ns; $\Delta t_1 = \Delta t_2$ =16 ns; shot repetition time (srt) = 3 ms.

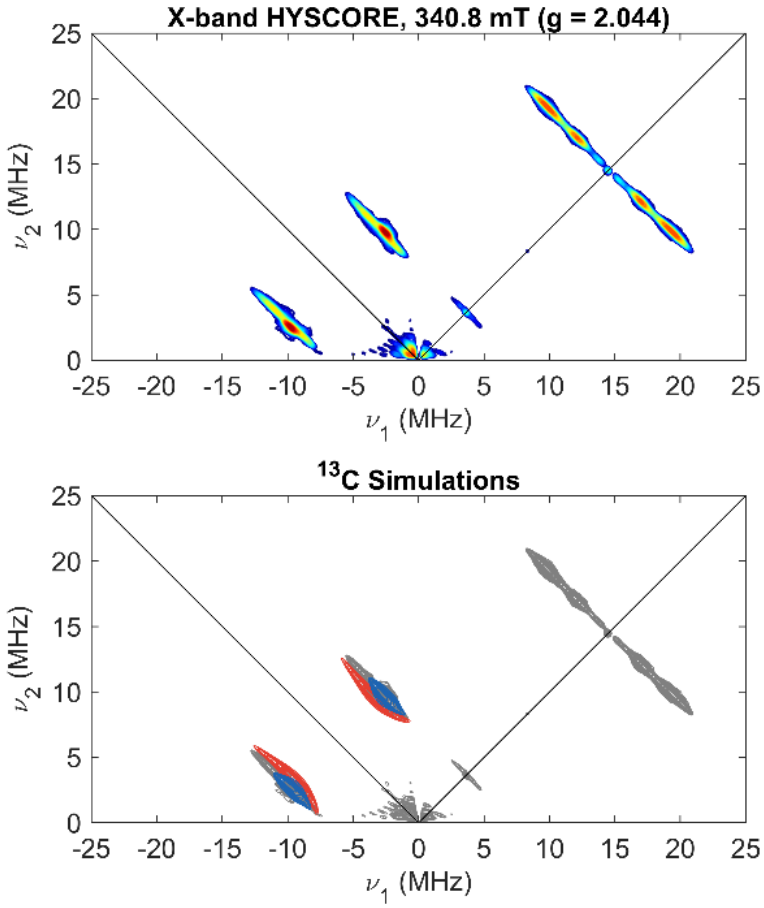

Figure S11—(Top) X-band HYSCORE of **[1-$^{13}C_2$][BAr^F_4]** collected at 340.8 mT (g = 2.044). (Bottom) Monochromatic representations of the HYSCORE data (grey), with simulations using parameters in Table 2 overlaid in red and blue for $^{13}C_A$ and $^{13}C_B$, respectively. Acquisition parameters: temperature = 25 K; MW frequency = 9.715 GHz; MW pulse length ($\pi/2$, π) = 8 ns, 16 ns; τ = 136 ns; $t_1 = t_2$ = 100 ns; $\Delta t_1 = \Delta t_2$ =16 ns; shot repetition time (srt) = 3 ms.

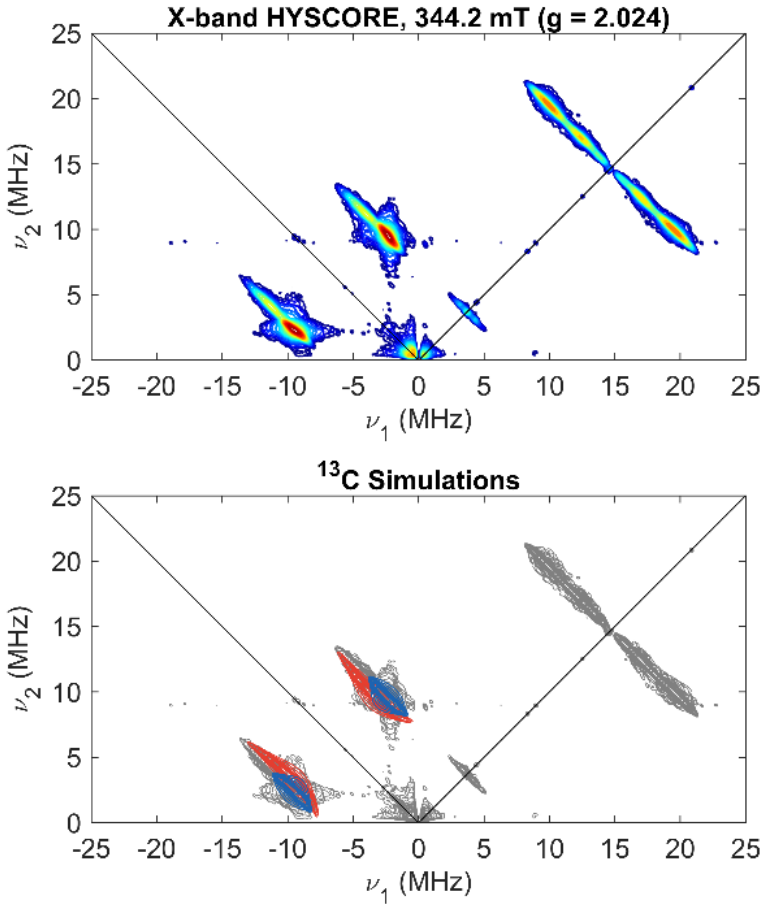

Figure S12—X-band HYSCORE spectrum of **[1-$^{13}C_2$][BAr^F_4]** (top) measured at 344.2 mT (g = 2.024). (Bottom) Monochromatic representations of the HYSCORE data (grey), with simulations using parameters in Table 2 overlaid in red and blue for $^{13}C_A$ and $^{13}C_B$, respectively. Acquisition parameters: temperature = 25 K; MW frequency = 9.715 GHz; MW pulse length ($\pi/2$, π) = 8 ns, 16 ns; τ = 136 ns; $t_1 = t_2$ = 100 ns; $\Delta t_1 = \Delta t_2$ =16ns; shot repetition time (srt) = 3 ms.

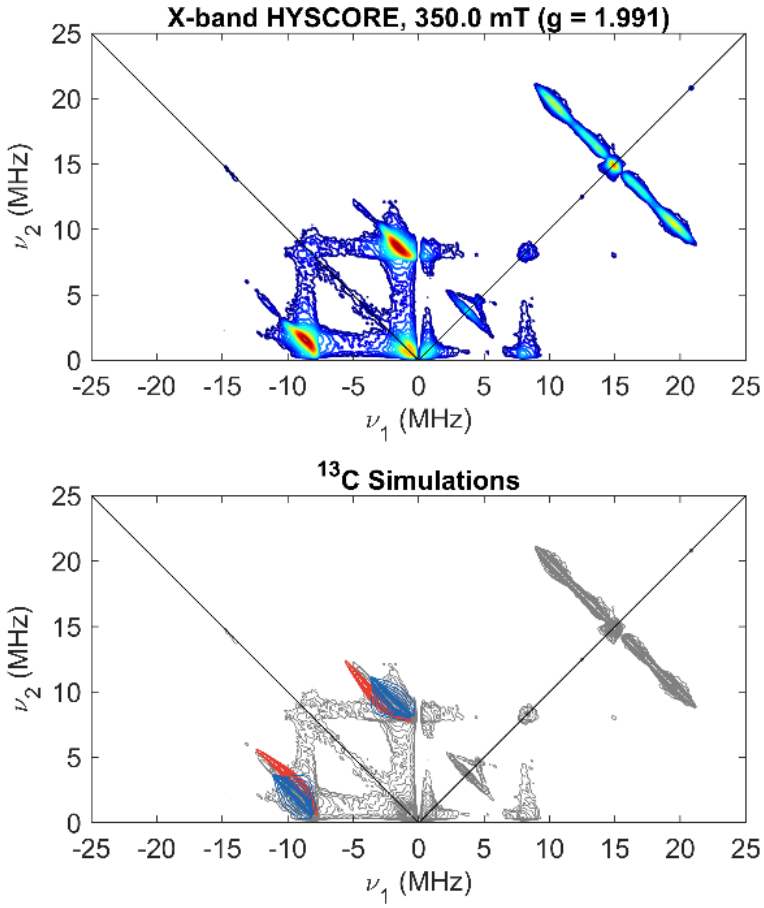

Figure S13—(Top) X-band HYSCORE of **[1-$^{13}C_2$][$BAr^F{}_4$]** collected at 350.0 mT (g = 1.991). (Bottom) Monochromatic representations of the HYSCORE data (grey), with simulations using parameters in Table 2 overlaid in red and blue for $^{13}C_A$ and $^{13}C_B$, respectively. Acquisition parameters: temperature = 25 K; MW frequency = 9.715 GHz; MW pulse length ($\pi/2$, π) = 8 ns, 16 ns; τ = 138 ns, $t_1 = t_2$ = 100 ns; $\Delta t_1 = \Delta t_2$ =16 ns; shot repetition time (srt) = 3 ms.

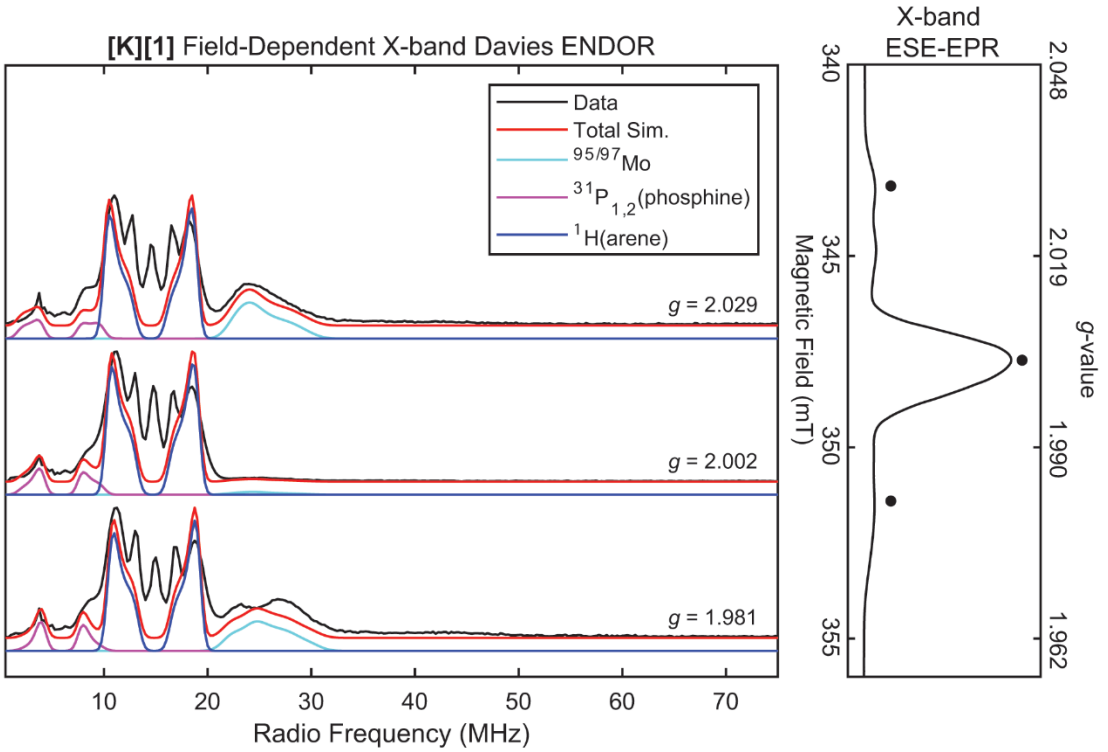

Figure S14—Field-dependent X-band Davies ENDOR of **[K][1]** (black) with simulations using parameters in Table 2 overlaid. The electron spin echo (ESE) detected EPR spectrum is shown to the right, with fields at which ENDOR was acquired denoted with black circles. Acquisition parameters: temperature = 35 K; MW frequency = 9.748 GHz; MW pulse length ($\pi/2$, π) = 40 ns, 80 ns; τ = 240 ns; RF pulse length = 15 μs; T_{RF} = 2 μs; shot repetition time = 5 ms.

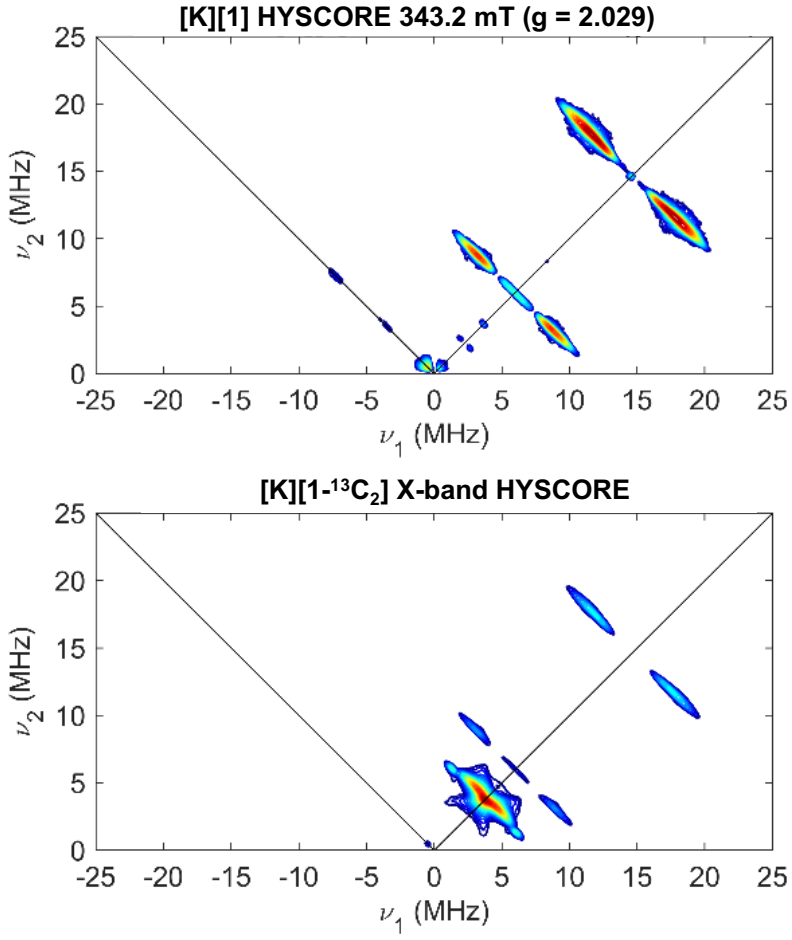

Figure S15—(Top) X-band HYSCORE of natural abundance **[K][1]** collected at 351.6 mT (g = 1.981). (Bottom) X-band HYSCORE of **[K][1-$^{13}C_2$]** collected at 351.6 mT (g = 1.981). Acquisition parameters: temperature = 55 K; MW frequency = 9.747 GHz; MW pulse length ($\pi/2$, π) = 8 ns, 16 ns; τ = 136 ns, $t_1 = t_2$ = 100 ns; $\Delta t_1 = \Delta t_2$ = 16 ns; shot repetition time (srt) = 1 ms.

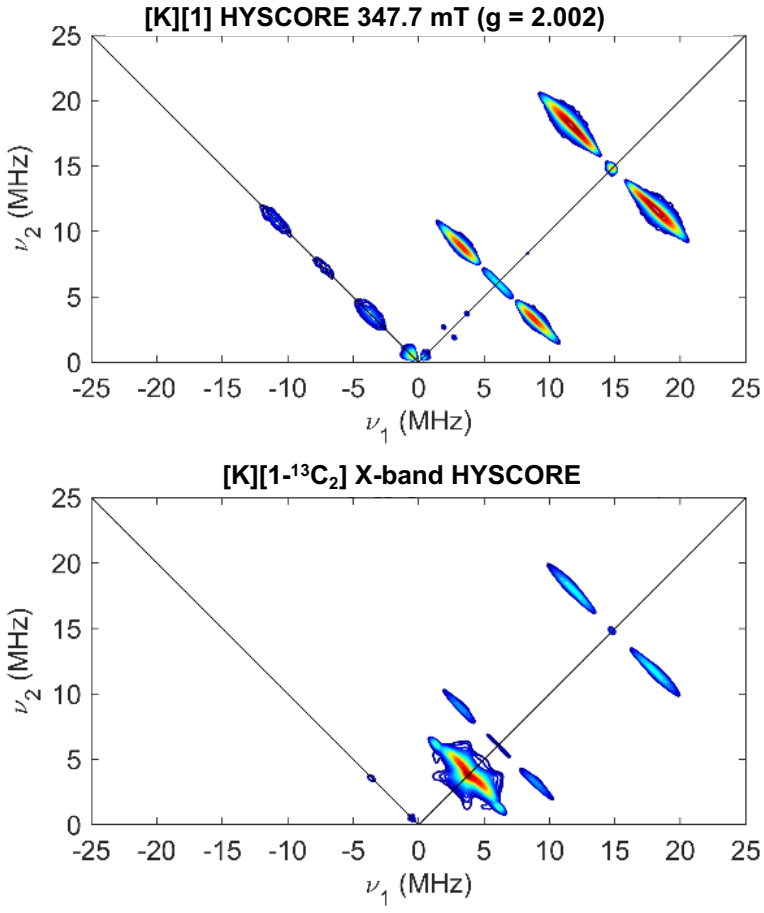

Figure S16—(Top) X-band HYSCORE of **[K][1]** collected at 347.7 mT (g = 2.002). (Bottom) X-band HYSCORE of **[K][1-$^{13}C_2$]** collected at 347.7 mT (g = 2.002). Acquisition parameters: temperature = 55 K; MW frequency = 9.747 GHz; MW pulse length ($\pi/2$, π) = 8 ns, 16 ns; τ = 136 ns, $t_1 = t_2$ = 100 ns; $\Delta t_1 = \Delta t_2$ = 16 ns; shot repetition time (srt) = 1 ms.

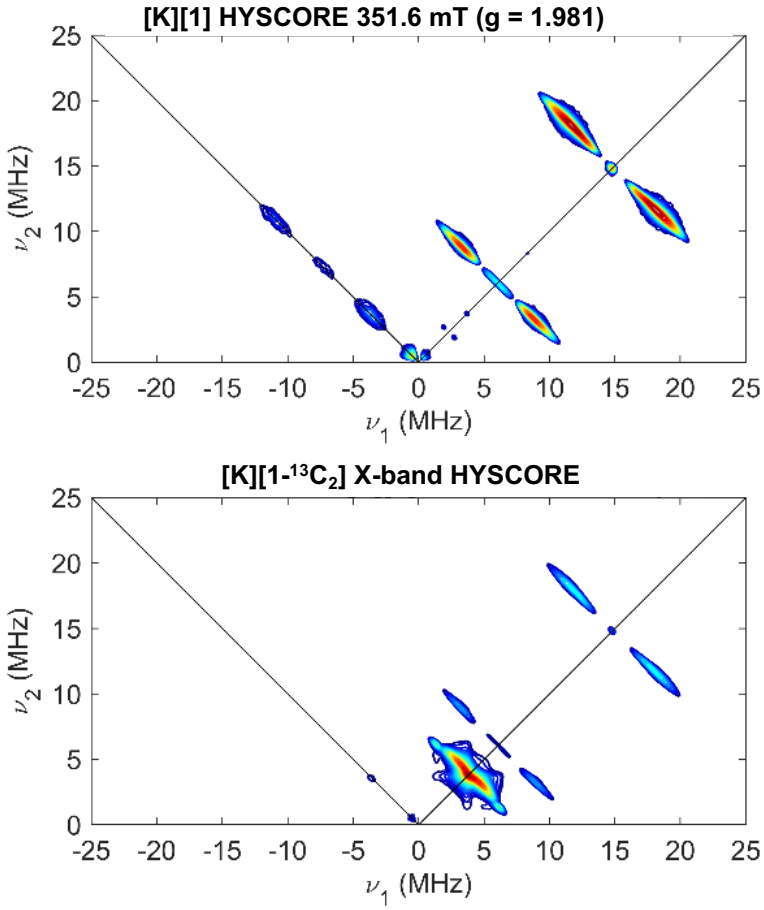

Figure S17—(Top) X-band HYSCORE of **[K][1]** collected at 351.6 mT (g = 1.981). (Bottom) X-band HYSCORE of **[K][1-$^{13}C_2$]** collected at 351.6 mT (g = 1.981). Acquisition parameters: temperature = 55 K; MW frequency = 9.747 GHz; MW pulse length ($\pi/2$, π) = 8 ns, 16 ns; τ = 136 ns, $t_1 = t_2$ = 100 ns; $\Delta t_1 = \Delta t_2$ = 16 ns; shot repetition time (srt) = 1 ms.

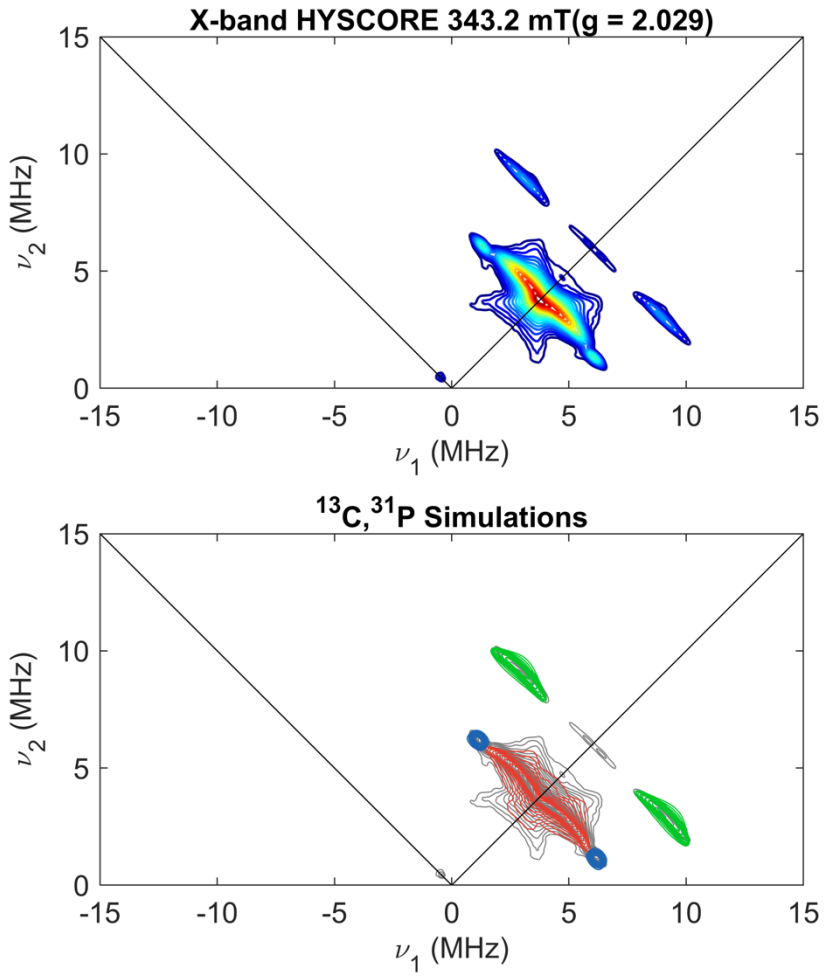

Figure S18—(Top) X-band HYSCORE of **[K][1-$^{13}C_2$]** collected at 343.2 mT (g = 2.029). (Bottom) Monochromatic representations of the HYSCORE data (grey), with simulations using parameters in Table 2 overlaid: (red) $^{13}C_A$, (blue) $^{13}C_B$, (green) $^{31}P_{1,2}$. Acquisition parameters: temperature = 55 K; MW frequency = 9.747 GHz; MW pulse length ($\pi/2$, π) = 8 ns, 16 ns; τ = 136 ns, $t_1 = t_2$ = 100 ns; $\Delta t_1 = \Delta t_2$ = 16 ns; shot repetition time (srt) = 1 ms.

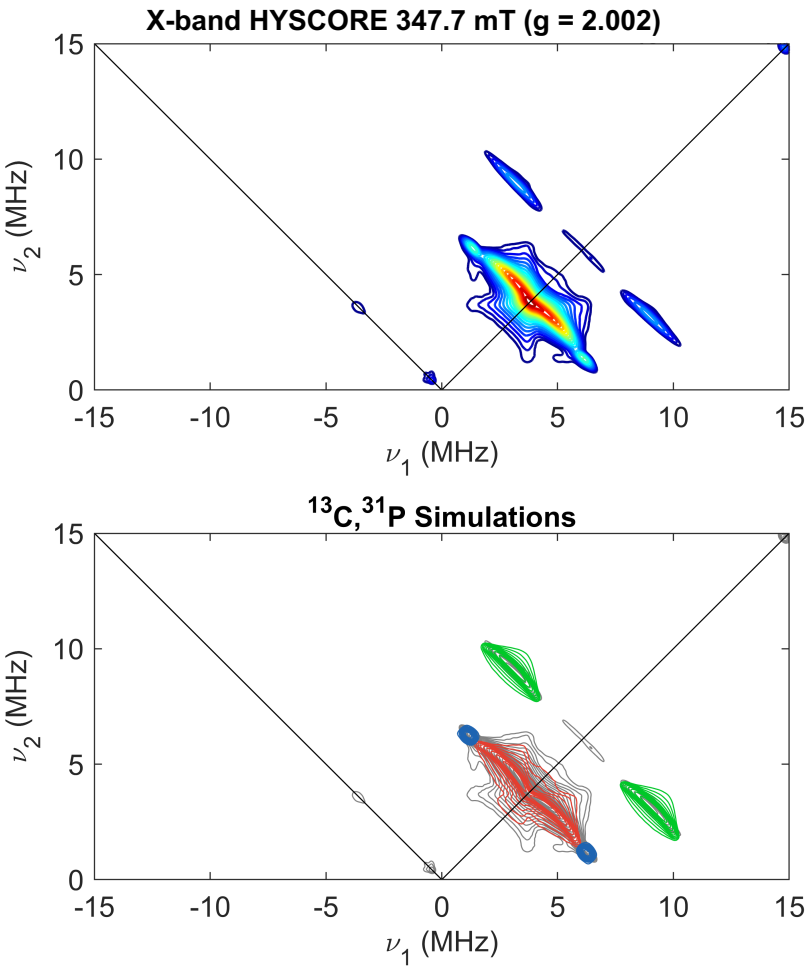

Figure S19—(Top) X-band HYSCORE of **[K][1-$^{13}C_2$]** collected at 347.7 mT (g = 2.002). (Bottom) Monochromatic representations of the HYSCORE data (grey), with simulations using parameters in Table 2 overlaid: (red) $^{13}C_A$, (blue) $^{13}C_B$, (green) $^{31}P_{1,2}$. Acquisition parameters: temperature = 55 K; MW frequency = 9.747 GHz; MW pulse length ($\pi/2$, π) = 8 ns, 16 ns; τ = 136 ns, $t_1 = t_2$ = 100 ns; $\Delta t_1 = \Delta t_2$ = 16 ns; shot repetition time (srt) = 1 ms.

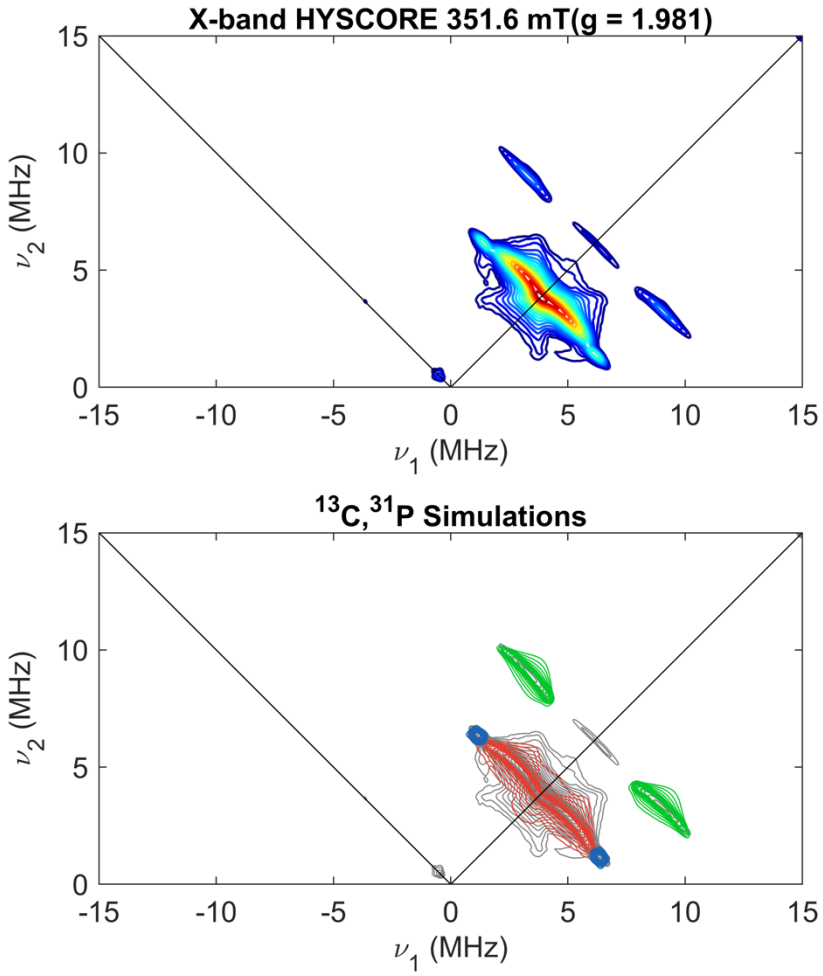

Figure S20—(Top) X-band HYSCORE of **[K][1-$^{13}C_2$]** collected at 351.6 mT (g = 1.981). (Bottom) Monochromatic representations of the HYSCORE data (grey), with simulations using parameters in Table 2 overlaid: (red) $^{13}C_A$, (blue) $^{13}C_B$, (green) $^{31}P_{1,2}$. Acquisition parameters: temperature = 55 K; MW frequency = 9.747 GHz; MW pulse length ($\pi/2$, π) = 8 ns, 16 ns; τ = 136 ns, $t_1 = t_2$ = 100 ns; $\Delta t_1 = \Delta t_2$ = 16 ns; shot repetition time (srt) = 1 ms.

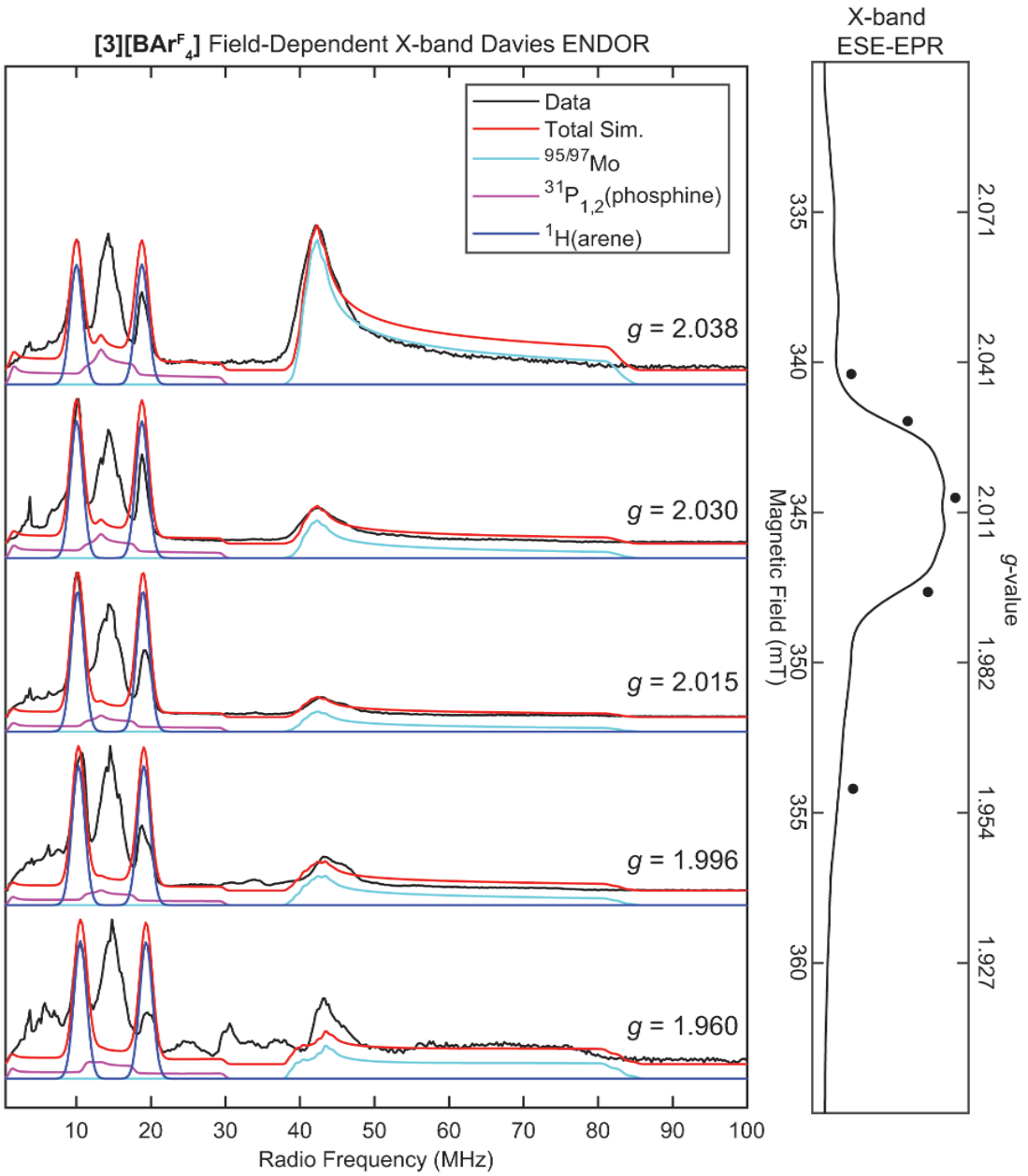

Figure S21—Field-Dependent X-band Davies ENDOR spectra of natural abundance **[3][BAr$^F_4$]** (black) with simulations overlaid using parameters in Table 4. The electron spin echo (ESE) detected EPR spectrum is shown to the right, with fields at which ENDOR was acquired denoted with black circles. Acquisition parameters: temperature = 25 K; MW frequency = 9.708 GHz; MW π pulse length = 80 ns; interpulse delay τ = 240 ns; π_{RF} pulse length = 15 μs; T_{RF} delay = 2 μs; shot repetition time (srt) = 5 ms.

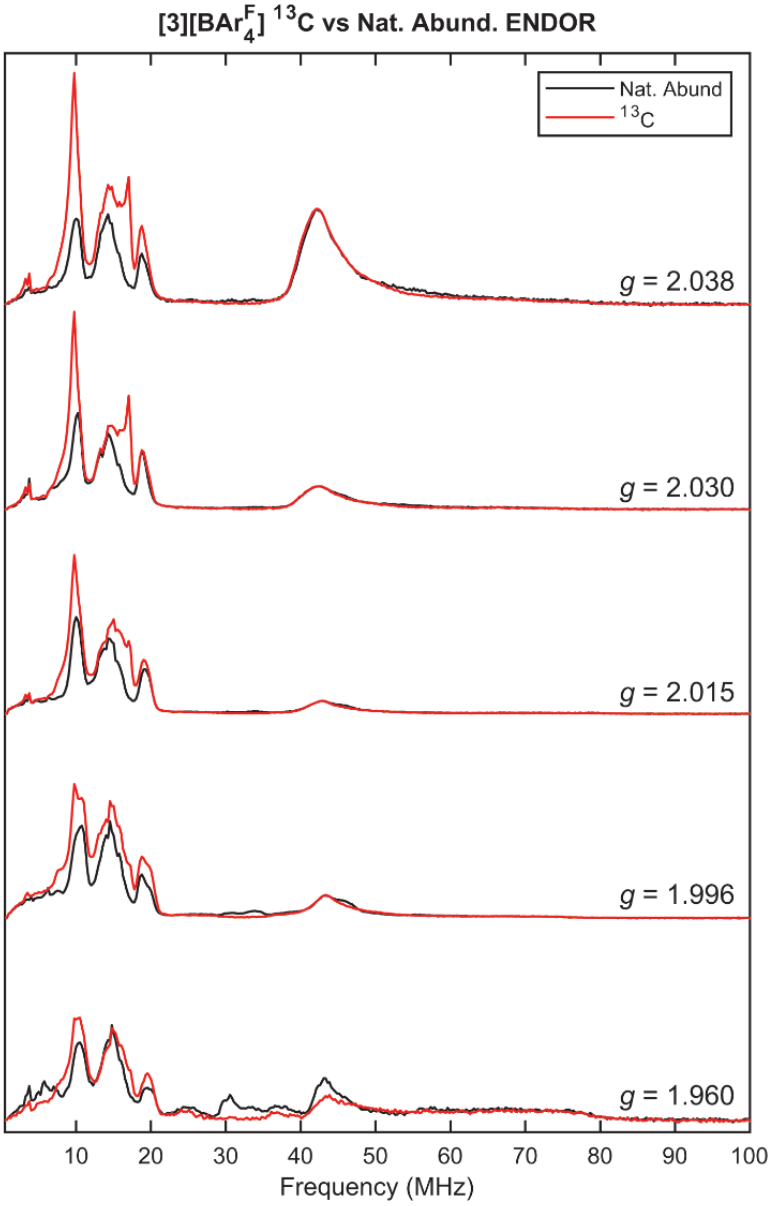

Figure S22—Field-Dependent X-band Davies ENDOR spectra of natural abundance **[3][BAr$^F_4$]** (black) and **[3-$^{13}C_2$][BAr$^F_4$]** (red). Acquisition parameters: temperature = 25 K; MW frequency = 9.708 GHz; MW π pulse length = 80 ns; interpulse delay τ = 240 ns; π_{RF} pulse length = 15 μs; T_{RF} delay = 2 μs; shot repetition time (srt) = 5 ms.

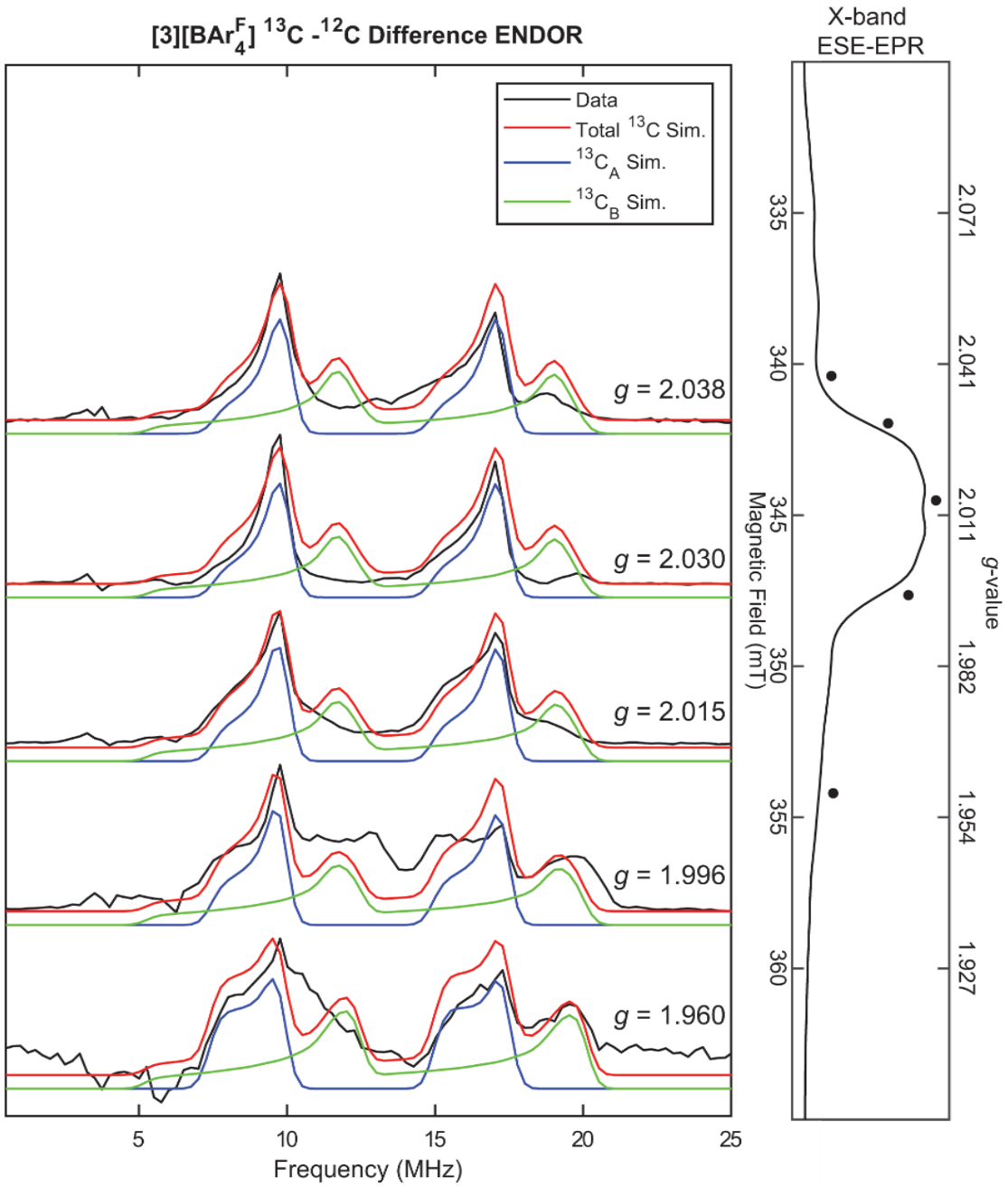

Figure S23—Field-Dependent ^{13}C-minus-natural abundance X-band Davies ENDOR spectra of **[3][BAr$^F_4$]** (black), with simulations of two inequivalent ^{13}C couplings overlaid using parameters in Table 4. The electron spin echo (ESE) detected EPR spectrum is shown to the right, with fields at which ENDOR was acquired denoted with black circles. Acquisition parameters: temperature = 25 K; MW frequency = 9.708 GHz; MW π pulse length = 80 ns; interpulse delay τ = 240 ns; π_{RF} pulse length = 15 μs; T_{RF} delay = 2 μs; shot repetition time (srt) = 5 ms.

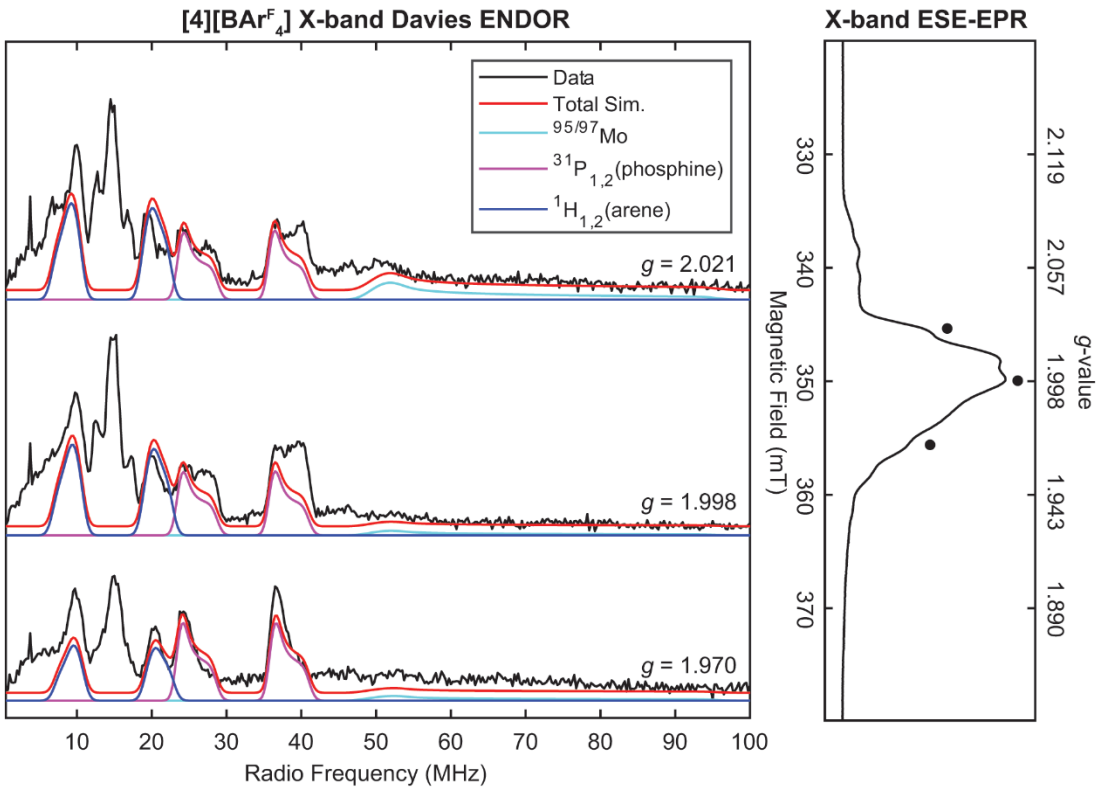

Figure S24—Field-Dependent X-band Davies ENDOR spectra of natural abundance **[4][BAr$^F_4$]** (black) with simulations overlaid using parameters in Table 4. The electron spin echo (ESE) detected EPR spectrum is shown to the right, with fields at which ENDOR was acquired denoted with black circles. Acquisition parameters: temperature = 25 K; MW frequency = 9.708 GHz; MW π pulse length = 80 ns; interpulse delay τ = 240 ns; π_{RF} pulse length = 15 μs; T_{RF} delay = 2 μs; shot repetition time (srt) = 5 ms.

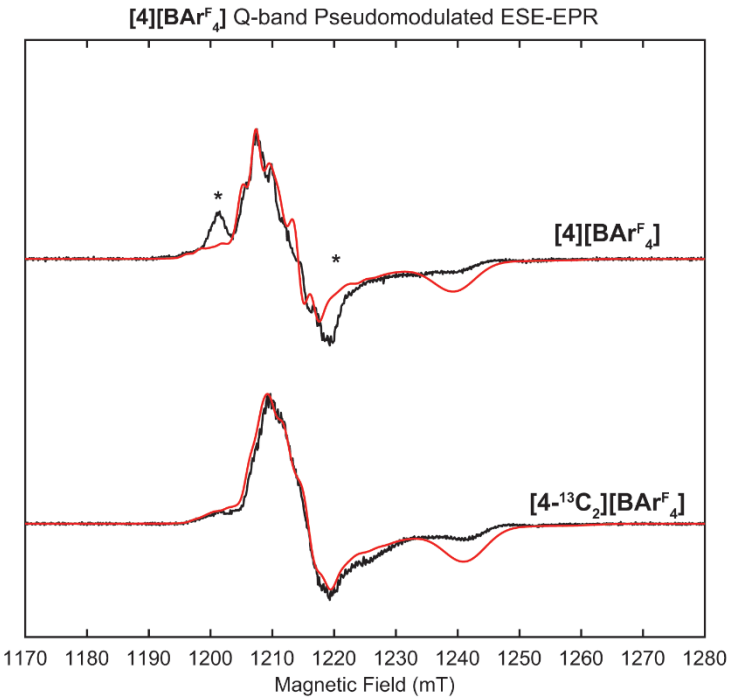

Figure S25—Q-band Pseudomodulated ESE-EPR spectra of **[4][BAr$^F_4$]** with natural abundance (top) and ^{13}C enrichment (bottom) represented in black with simulations using parameters in Table 4. Pseudomodulation function amplitude = 0.2 mT. Experimental conditions: microwave frequency = 34.089 GHz; π pulse length = 160 ns; interpulse delay τ = 300 ns; shot repitition time (srt) = 1 ms; temperature = 35 K. Asterisks indicate features associated with residual **[3][BAr$^F_4$]** due to incomplete CO loss.

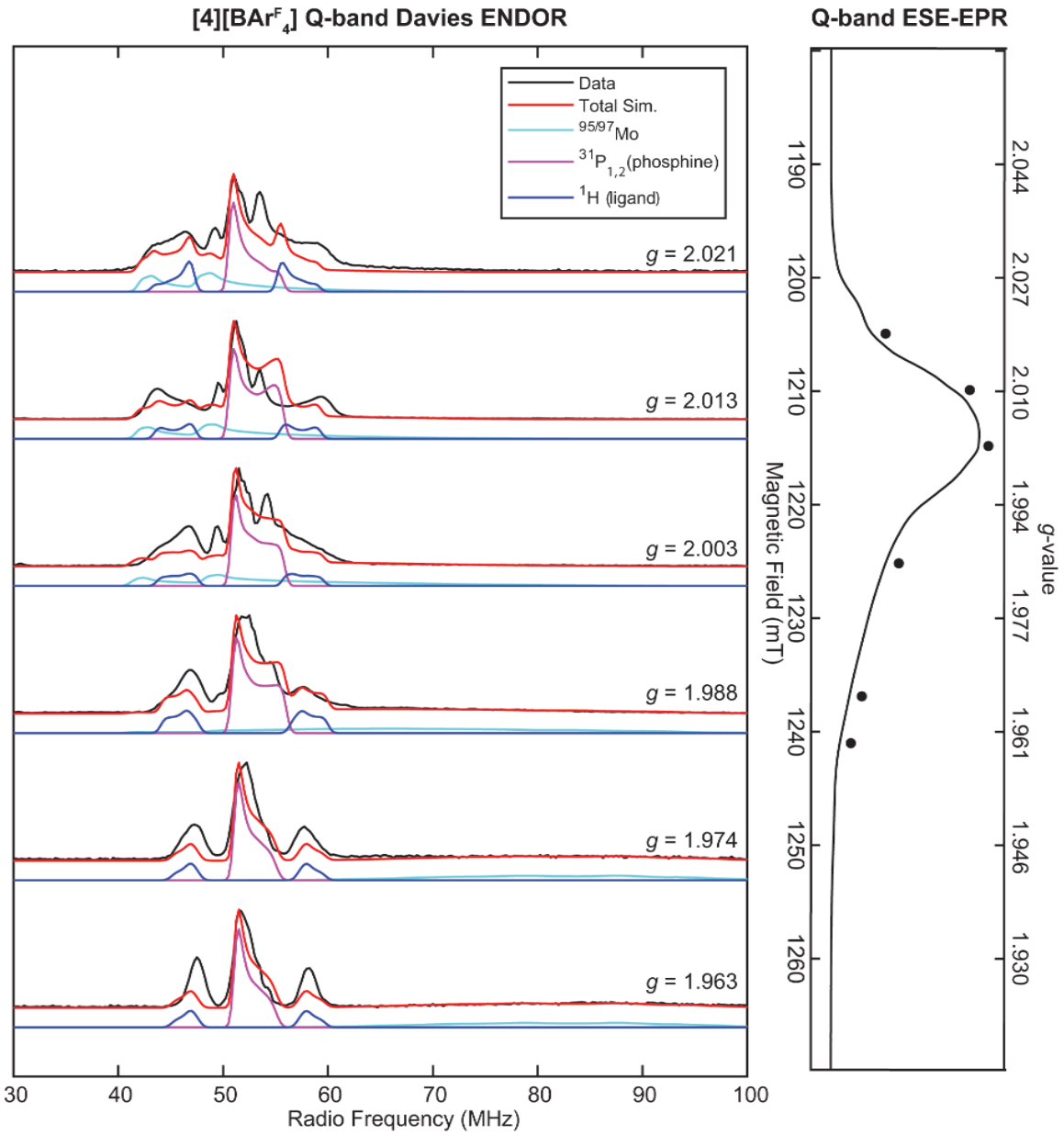

Figure S26—Field-Dependent Q-band Davies ENDOR spectra of natural abundance **[4][BAr$^F_4$]** (black) with simulations overlaid using parameters in Table 4. The electron spin echo (ESE) detected EPR spectrum is shown to the right, with fields at which ENDOR was acquired denoted with black circles. Acquisition parameters: temperature = 25 K; MW frequency = 34.092 GHz; MW π pulse length = 80 ns; interpulse delay τ = 240 ns; π_{RF} pulse length = 15 μs; T_{RF} delay = 2 μs; shot repetition time (srt) = 5 ms.

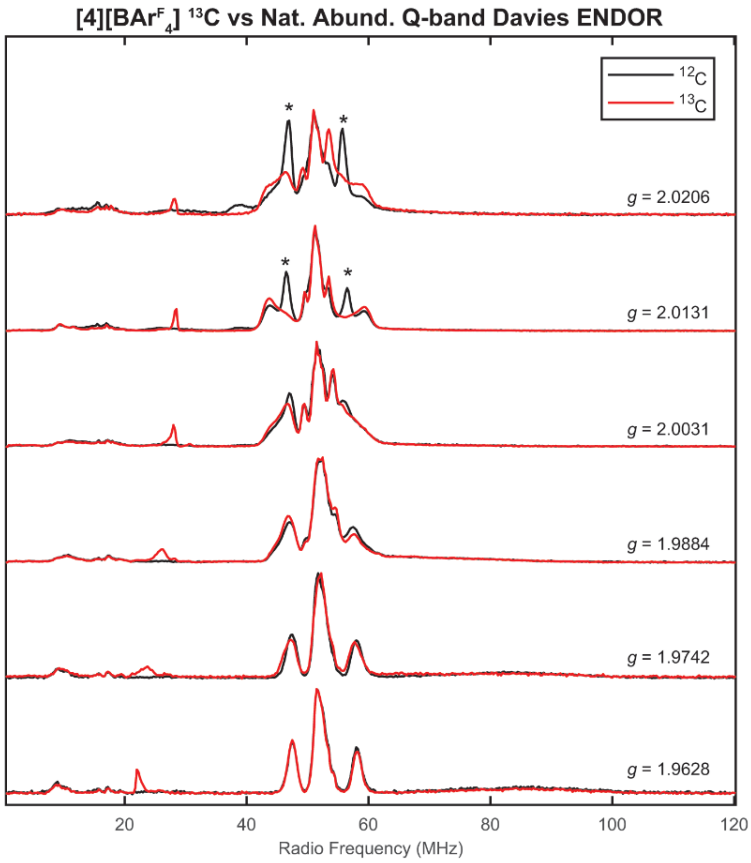

Figure S27— Field-Dependent Q-band Davies ENDOR spectra of natural abundance **[4][BAr$^F_4$]** (black) and **[4-^{13}C][BAr$^F_4$]** (red). Asterisks indicate features arising from residual **[3][BAr$^F_4$]** present in only the natural abundance sample. Acquisition parameters: temperature = 25 K; MW frequency = 34.092 GHz; MW π pulse length = 80 ns; interpulse delay τ = 240 ns; π_{RF} pulse length = 15 μs; T_{RF} delay = 2 μs; shot repetition time (srt) = 5 ms.

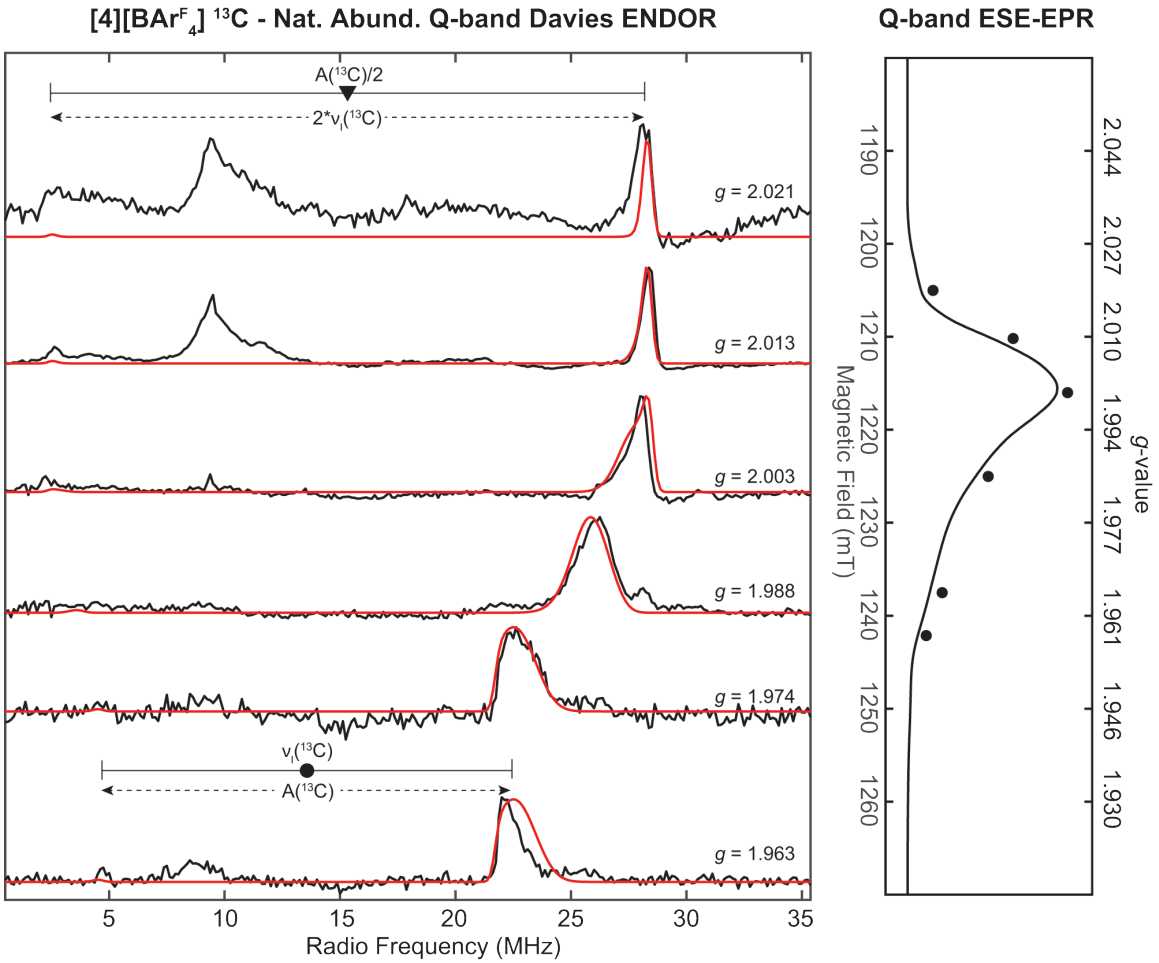

Figure S28—Field-Dependent ^{13}C-minus-natural abundance Q-band Davies ENDOR spectra of **[4][BAr$^F_4$]** (black), with simulations of ^{13}C coupling overlaid in red using parameters in Table 4. Acquisition parameters: temperature = 25 K; MW frequency = 34.092 GHz; MW π pulse length = 80 ns; interpulse delay τ = 240 ns; π_{RF} pulse length = 60 μs; T_{RF} delay = 2 μs; shot repetition time (srt) = 5 ms.

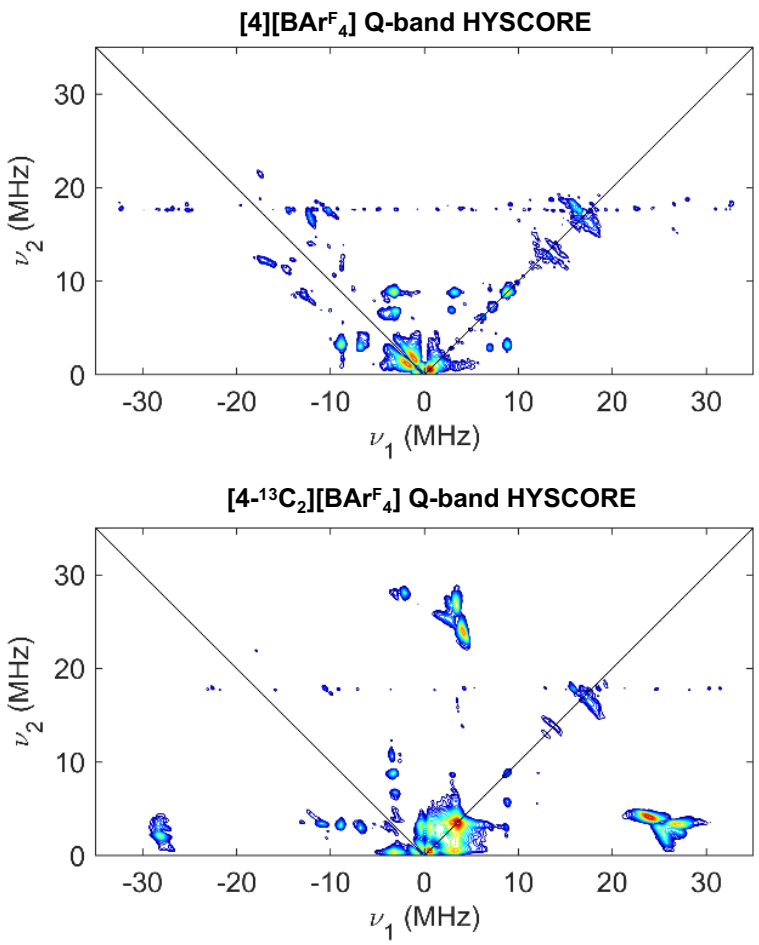

Figure S29—(Top) Q-band HYSCORE of **[4][BAr$^{F}_{4}$]** collected at 1216 mT (g = 2.003). (Bottom) Q-band HYSCORE of **[4-^{13}C][BAr$^{F}_{4}$]** collected at 1216 mT (g = 2.003). Acquisition parameters: temperature = 25 K; MW frequency = 34.089 GHz; MW pulse length ($\pi/2$, π) = 12 ns, 24 ns; τ = 100 ns, $t_1 = t_2$ = 100 ns; $\Delta t_1 = \Delta t_2$ = 8 ns; shot repetition time (srt) = 1 ms.

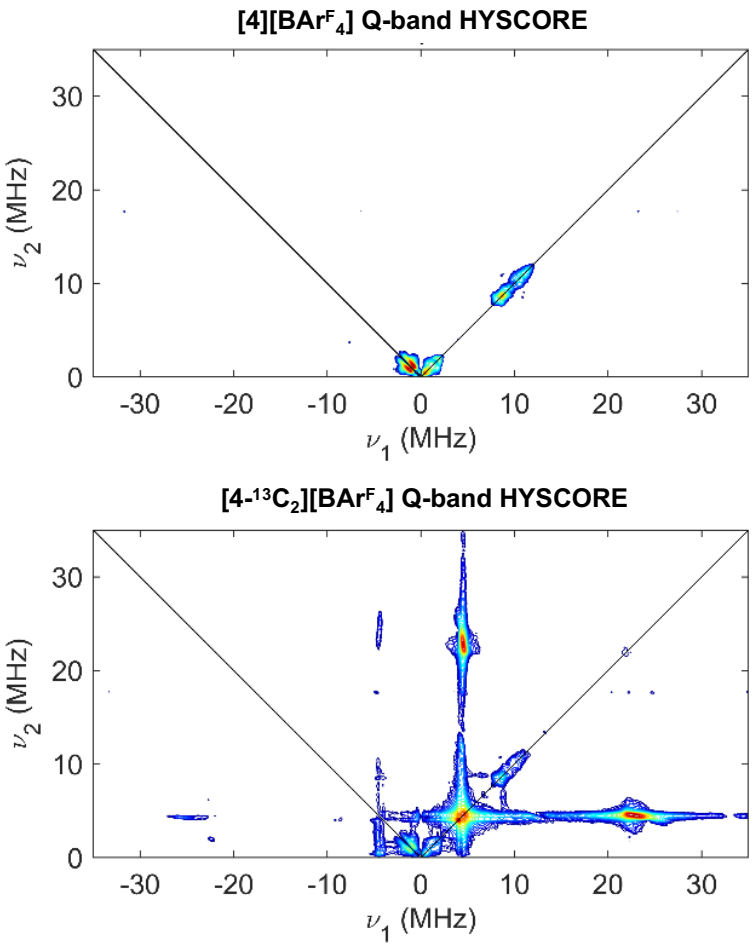

Figure S30—(Top) Q-band HYSCORE of **[4][BAr$^F_4$]** collected at 1241 mT (g = 2.963). (Bottom) Q-band HYSCORE of **[4-^{13}C][BAr$^F_4$]** collected at 1216 mT (g = 2.963). Acquisition parameters: temperature = 25 K; MW frequency = 34.089 GHz; MW pulse length ($\pi/2$, π) = 12 ns, 24 ns; τ = 100 ns, $t_1 = t_2$ = 100 ns; $\Delta t_1 = \Delta t_2$ = 8 ns; shot repetition time (srt) = 1 ms.

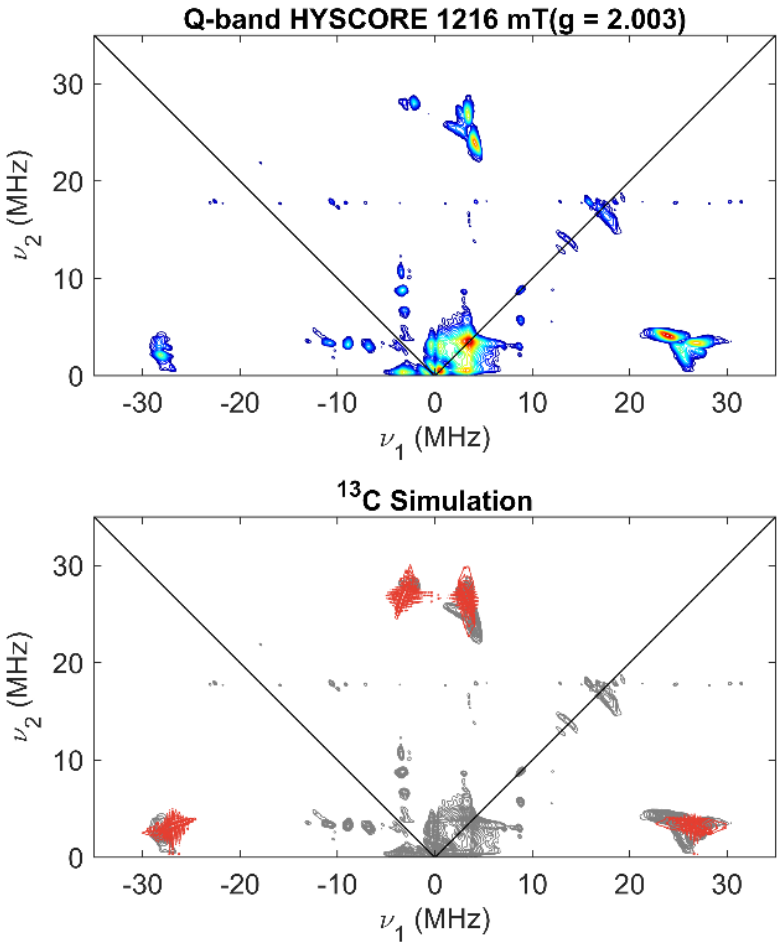

Figure S31—(Top) Q-band HYSCORE of **[4-^{13}C][BAr$^{F}_{4}$]** collected at 1216 mT (g = 2.003). (Bottom) Monochromatic representations of the HYSCORE data (grey), with ^{13}C simulation using parameters in Table 4 overlaid in red. Acquisition parameters: temperature = 25 K; MW frequency = 34.089 GHz; MW pulse length ($\pi/2$, π) = 12 ns, 24 ns; τ = 100 ns, $t_1 = t_2$ = 100 ns; $\Delta t_1 = \Delta t_2$ = 8 ns; shot repetition time (srt) = 1 ms.

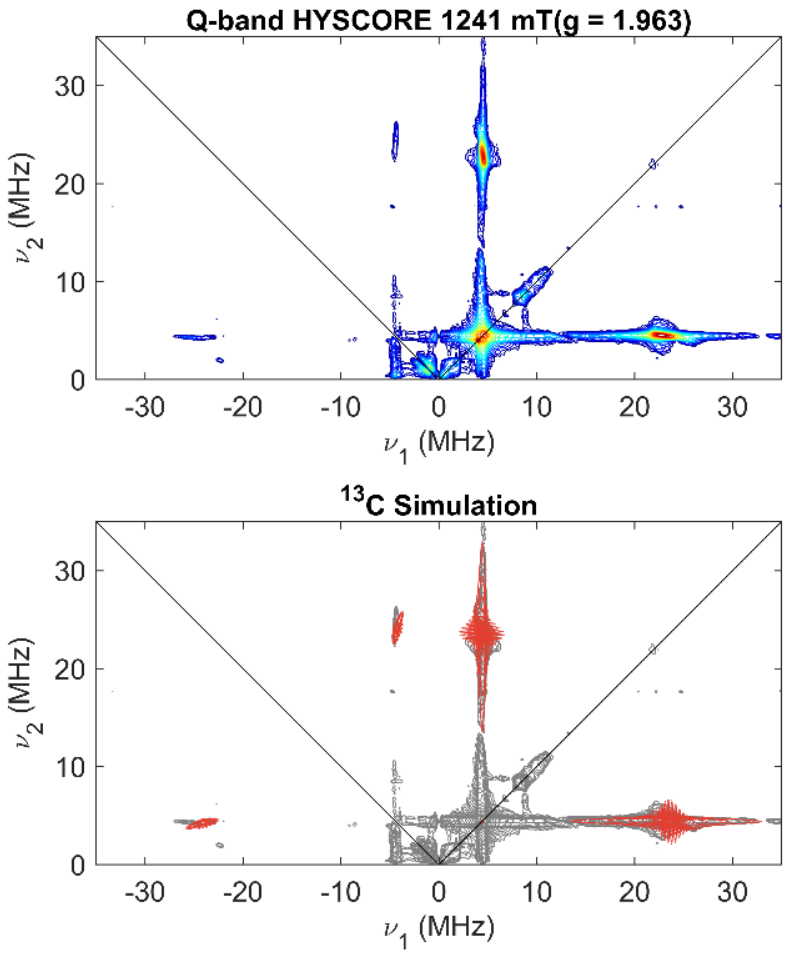

Figure S32—(Top) Q-band HYSCORE of ^{13}C-enriched **[4][BAr$_4^F$]** collected at 1241 mT (g = 2.963). (Bottom) Monochromatic representations of the HYSCORE data (grey), with ^{13}C simulation using parameters in Table 4 overlaid in red. Acquisition parameters: temperature = 25 K; MW frequency = 34.089 GHz; MW pulse length ($\pi/2$, π) = 12 ns, 24 ns; τ = 100 ns, $t_1 = t_2$ = 100 ns; $\Delta t_1 = \Delta t_2$ = 8 ns; shot repetition time (srt) = 1 ms.

IR Spectra

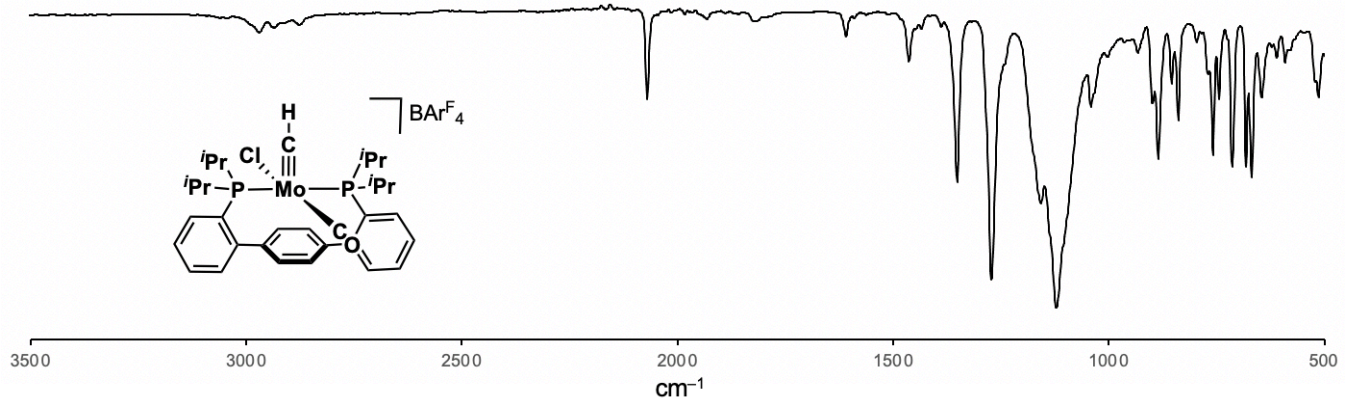

Figure S33—ATR-IR spectrum of **[2][BAr$^F_4$]**.

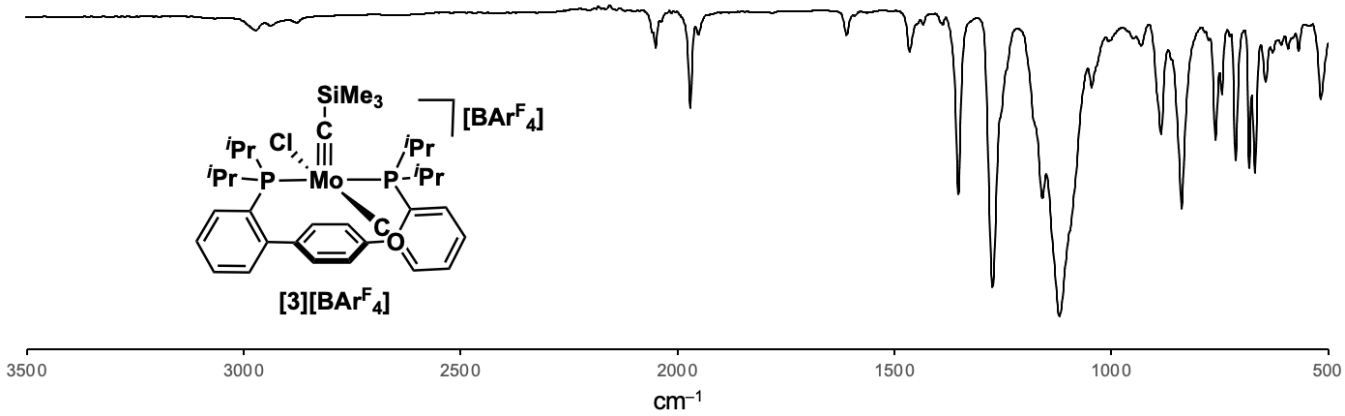

Figure S34—ATR-IR spectrum of **[3][BAr$^F_4$]**.

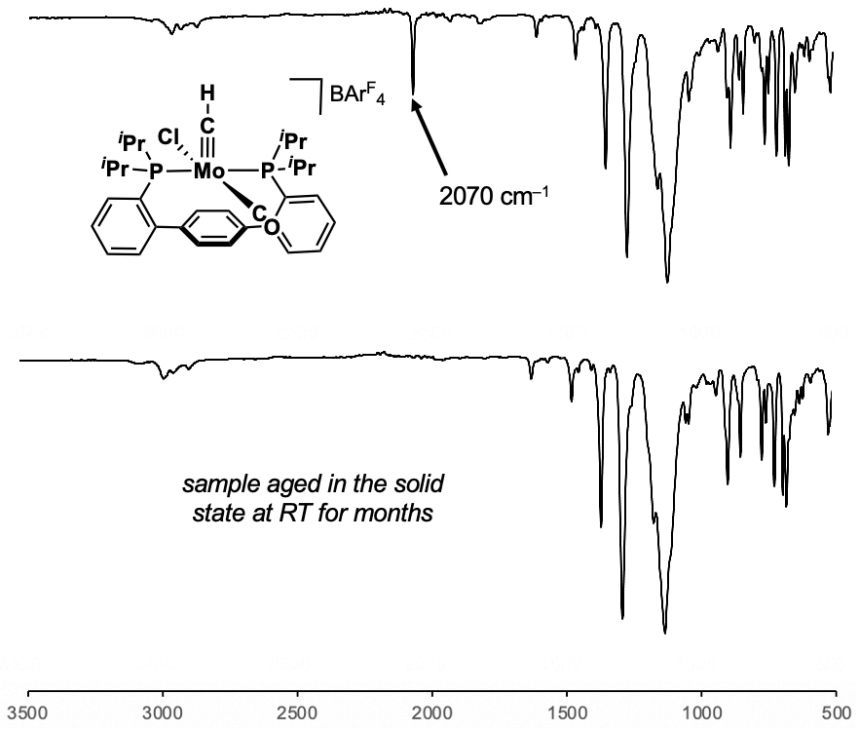

Figure S35—ATR-IR spectra of freshly-prepared **[2][BAr$^{F}_{4}$]** (top) and a sample aged at RT in the solid state for a period of months (bottom) showing loss of CO. An accompanying color change from green to purple is observed.

COMPUTATIONAL DETAILS

General methods.

Calculations were performed using an unrestricted Kohn-Sham approach to density functional theory (DFT) as implemented in ORCA, version 4.02,[8] Geometry optimizations and electronic structure calculations were performed using the revised BP86 functional and def2-TZVP basis set on all atoms.[9] Optimizations were performed ignoring molecular symmetry, starting from crystallographic coordinates, but using a truncated ligand model with PMe_2 substituents used in place of P^iPr_2. Frequency calculations were performed on optimized geometries to ensure true minima with real vibrational modes. Molecular orbitals were visualized using UCSF Chimera.[11] Löwdin spin populations were calculated in ORCA, using the Grid5 and Finalgrid6 specifications.

DFT-optimized structures and spin density plots

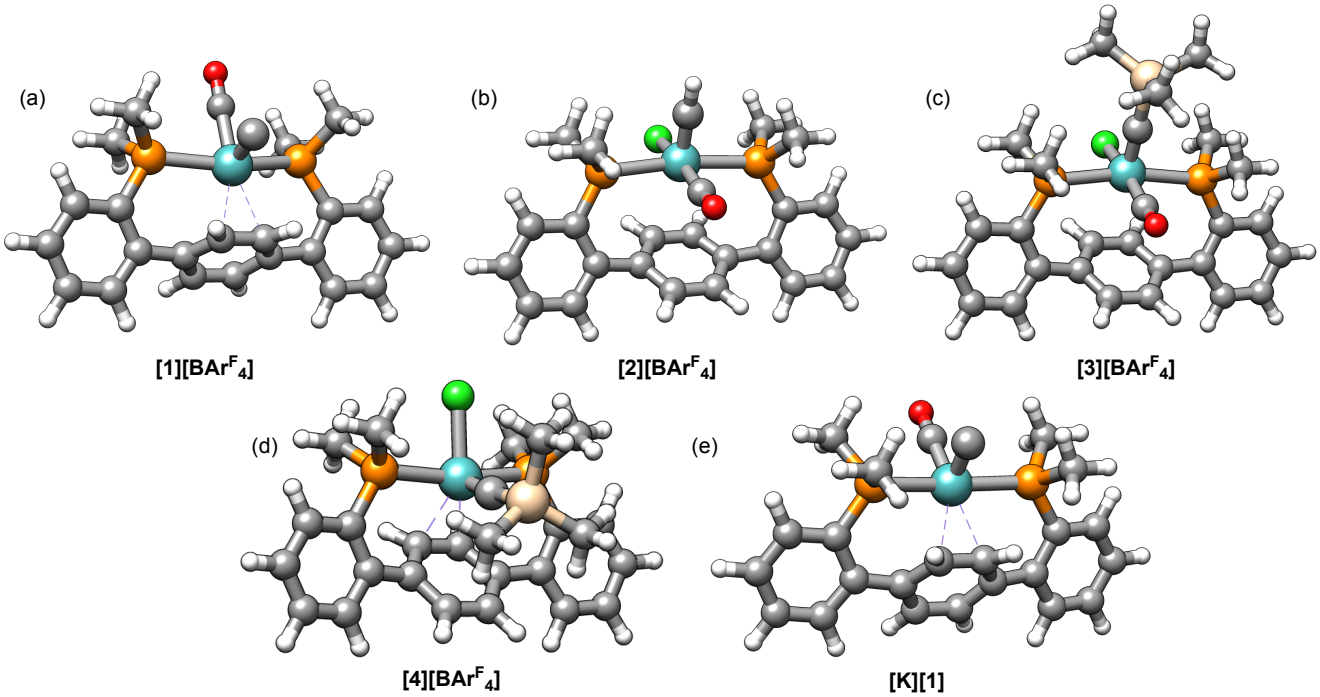

Figure S36—DFT-optimized structures for open-shell carbide and carbyne complexes studied (BP86/def2-TZVP). Atom colors: Grey: C; Light cyan: Mo; Orange: P; Red: O; Light green: Cl; Tan: Si.

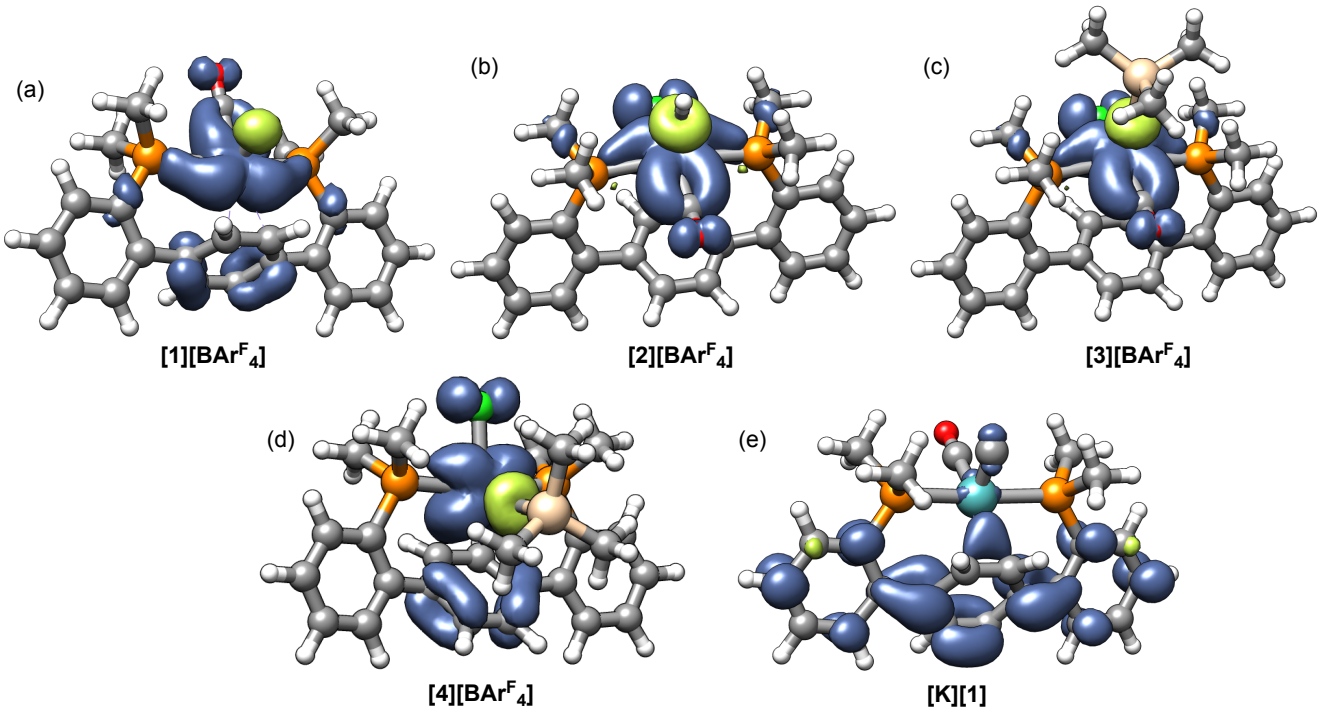

Figure S37—DFT-calculated spin density plots (BP86/def2-TZVP) for open-shell carbide and carbyne complexes studied. Isosurfaces shown at the 0.0016 e^- Å^{-3} level. Atom colors: Grey: C; Light cyan: Mo; Orange: P; Red: O; Light green: Cl; Tan: Si.

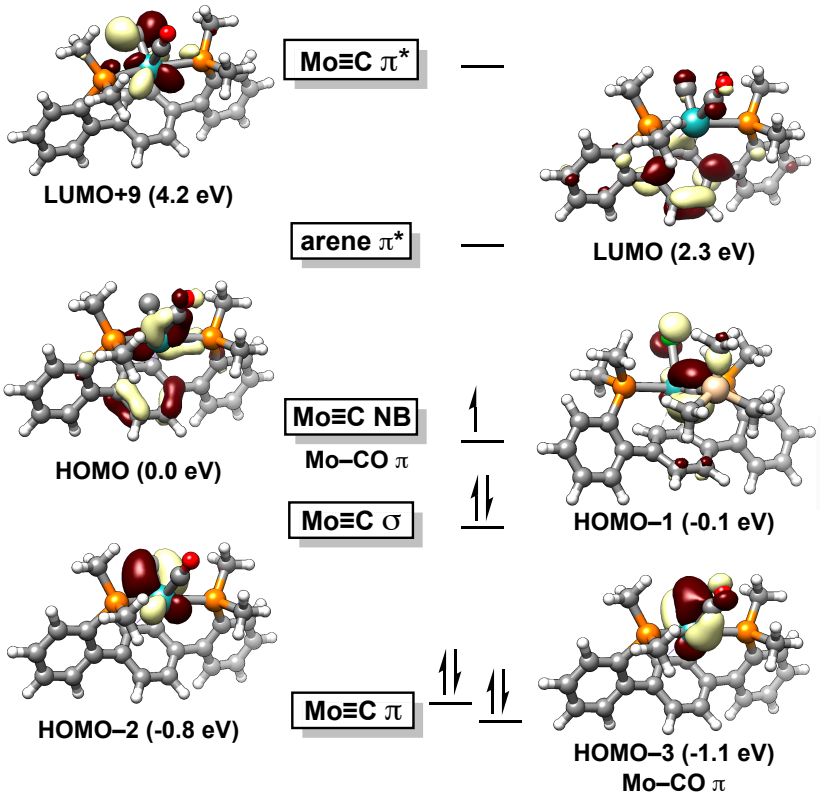

Figure S38—Qualitative MO diagram for **[1][BAr$^{F}_{4}$]** depicting the bonding interactions of Mo with the carbide ligand. Calculated α-molecular orbitals are depicted with isosurfaces at the 0.05 e^{-} $Å^{-3}$ level; the corresponding β-molecular orbitals are depicted in Figure S39. Orbital energies relative to the HOMO are given in eV.

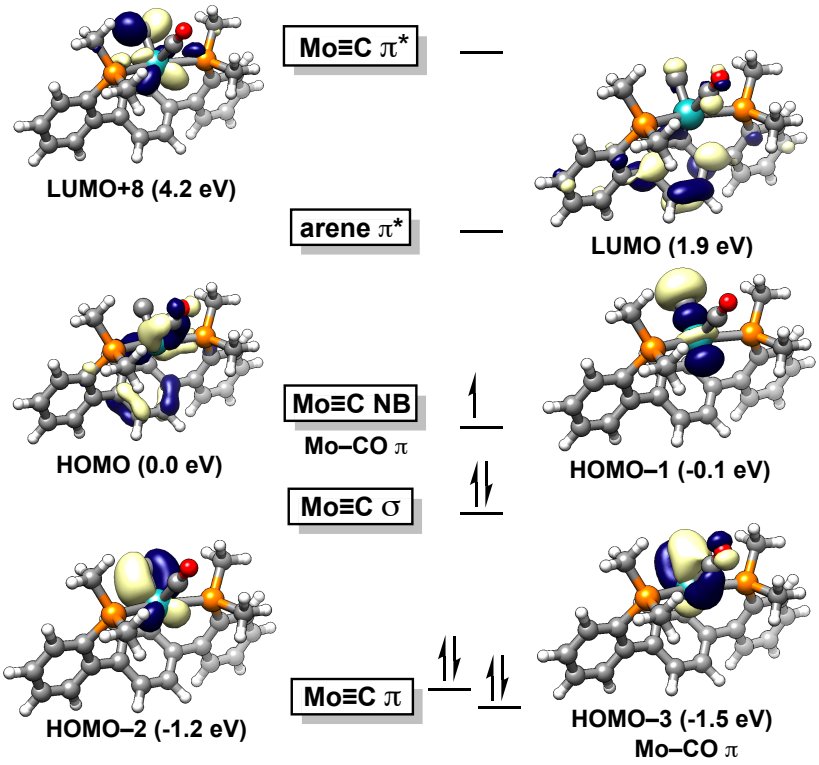

Figure S39—Qualitative MO diagram for **[1][BAr$^{F}_{4}$]** depicting only the β-molecular orbitals with isosurfaces at the 0.05 e^{-} $Å^{-3}$ level. Orbital energies relative to the HOMO are given in eV.

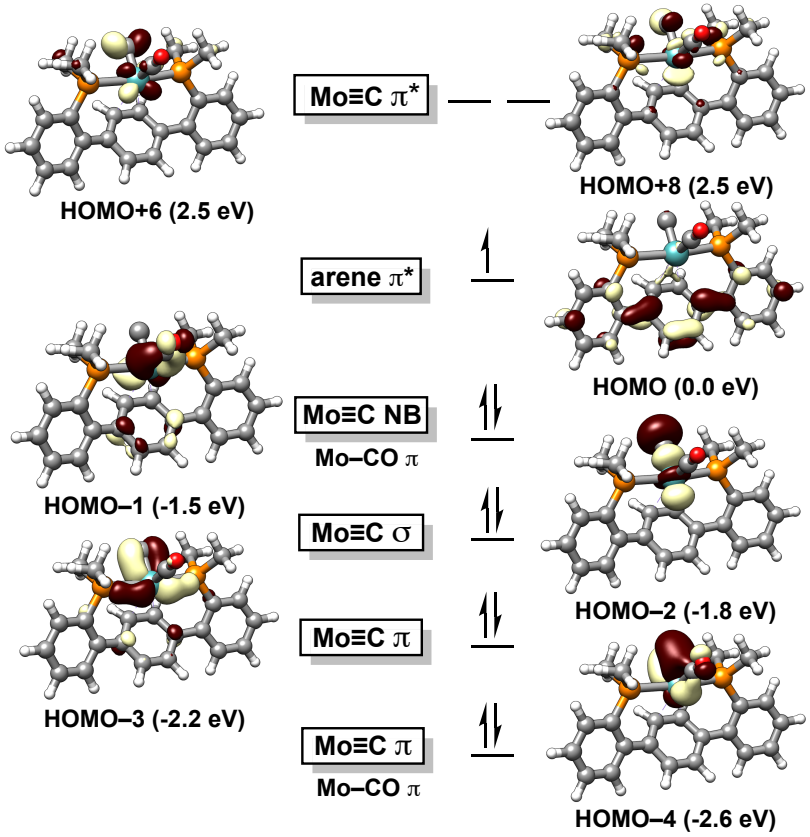

Figure S40—Qualitative MO diagram for **[K][1]** depicting the bonding interactions of Mo with the carbide ligand. Calculated α-molecular orbitals are depicted with isosurfaces at the 0.05 e^{-} $Å^{-3}$ level; the corresponding β-molecular orbitals are depicted in Figure S38. Orbital energies relative to the HOMO are given in eV.

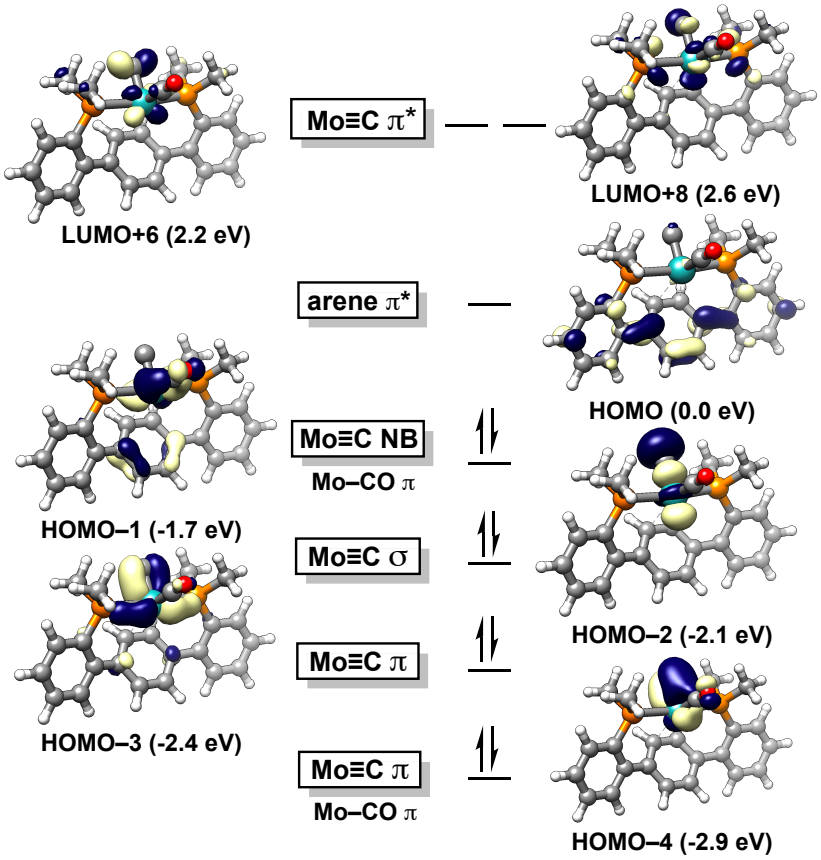

Figure S41—Qualitative MO diagram for **[K][1]** depicting only the β-molecular orbitals with isosurfaces at the 0.05 e^{-} $Å^{-3}$ level. Orbital energies relative to the HOMO are given in eV.

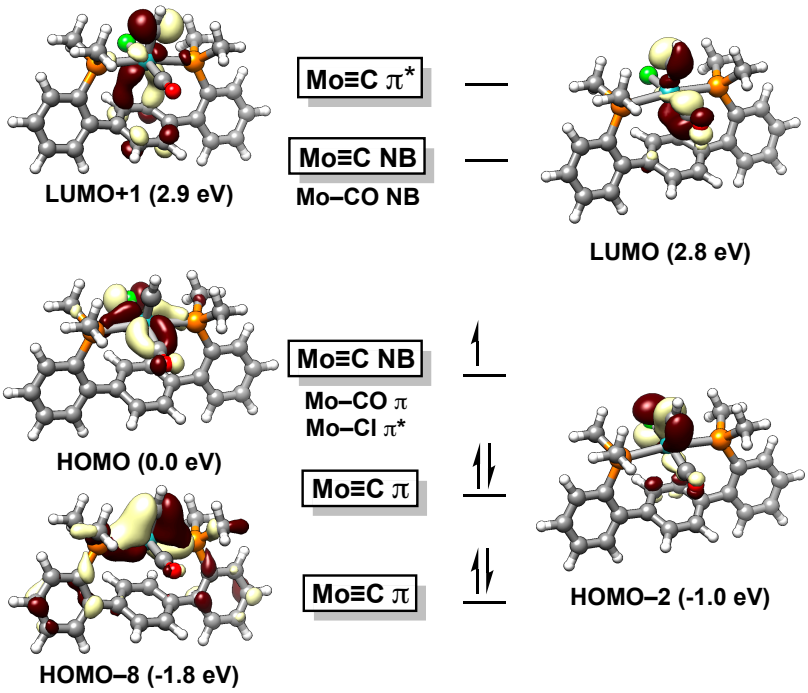

Figure S42—Qualitative MO diagram for **[2][BAr$^{F}_{4}$]** depicting the bonding interactions of Mo with the carbide ligand. Calculated α-molecular orbitals are depicted with isosurfaces at the 0.05 e^{-} $Å^{-3}$ level; the corresponding β-molecular orbitals are depicted in Figure S40. Orbital energies relative to the HOMO are given in eV.

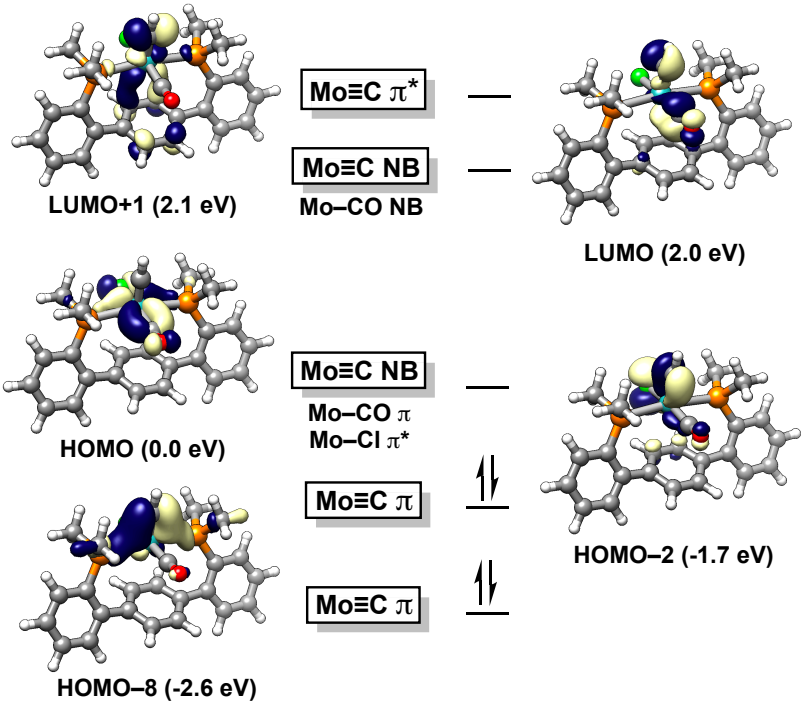

Figure S43—Qualitative MO diagram for **[2][BAr$^{F}_{4}$]** depicting only the corresponding β-molecular orbitals with isosurfaces at the 0.05 e^{-} $Å^{-3}$ level. Orbital energies relative to the HOMO are given in eV.

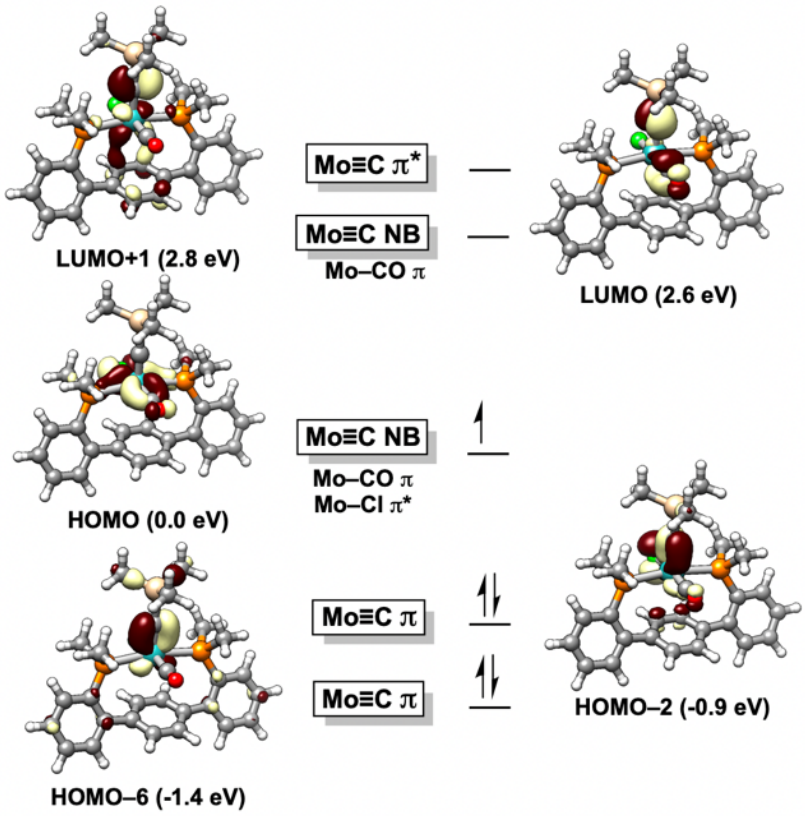

Figure S44—Qualitative MO diagram for **[3][BAr$^{F}_{4}$]** depicting the bonding interactions of Mo with the carbide ligand. Calculated α-molecular orbitals are depicted with isosurfaces at the 0.05 e^{-} $Å^{-3}$ level; the corresponding β-molecular orbitals are depicted in Figure S42. Orbital energies relative to the HOMO are given in eV.

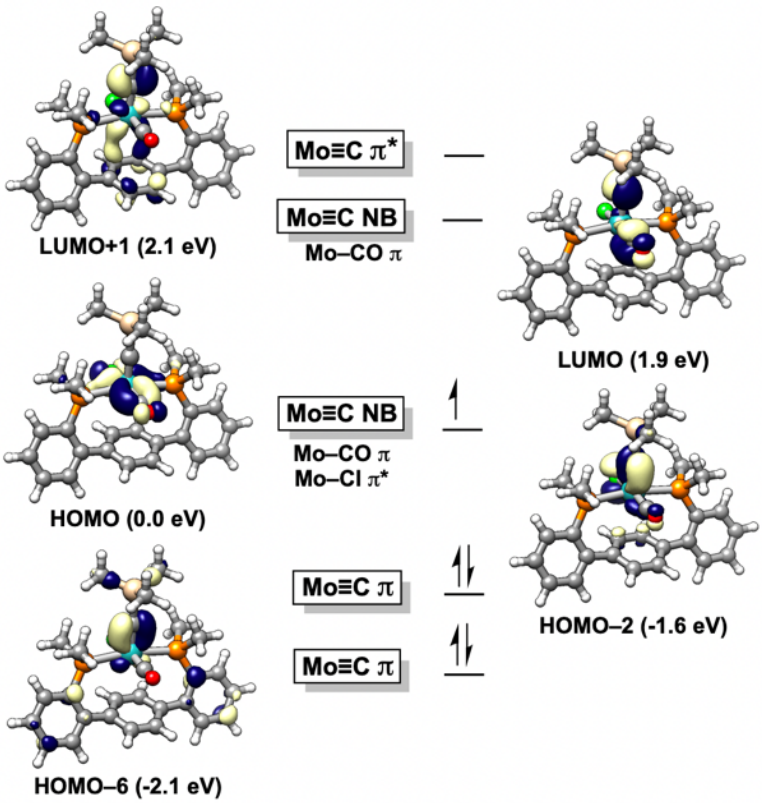

Figure S45—Qualitative MO diagram for **[3][BAr$^{F}_{4}$]** depicting only the corresponding β-molecular orbitals with isosurfaces at the 0.05 e^{-} $Å^{-3}$ level. Orbital energies relative to the HOMO are given in eV.

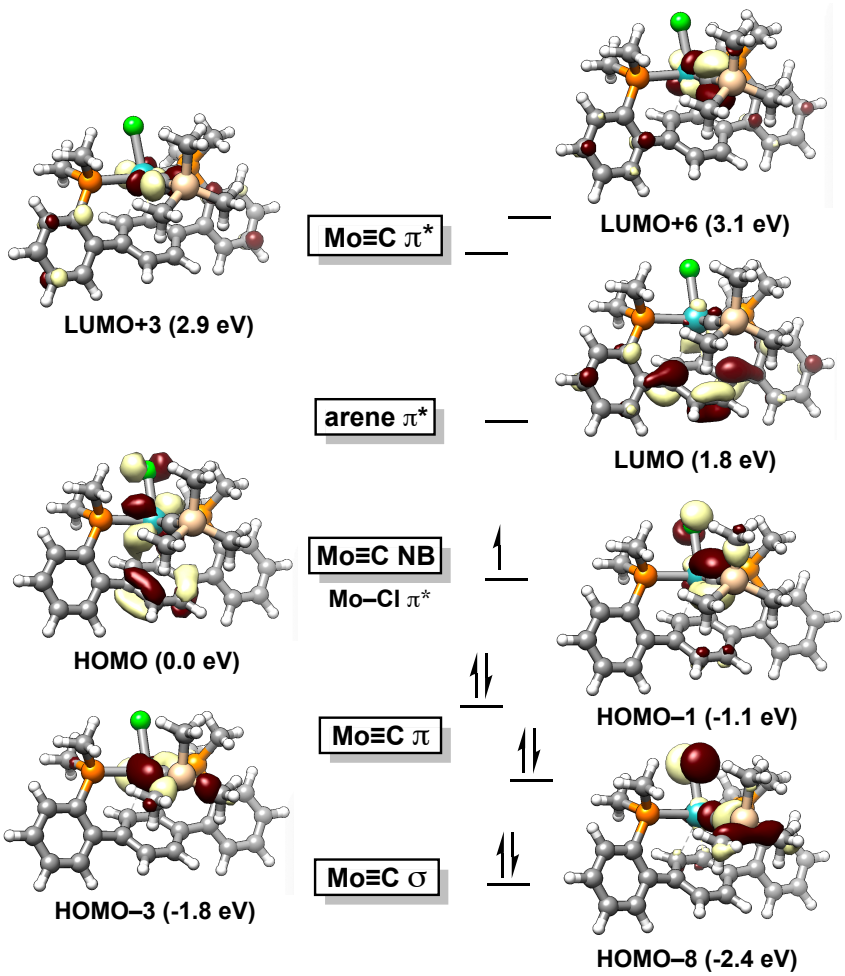

Figure S46—Qualitative MO diagram for **[4][BAr$^{F}_{4}$]** depicting the bonding interactions of Mo with the carbide ligand. Calculated α-molecular orbitals are depicted with isosurfaces at the 0.05 e^{-} $Å^{-3}$ level; the corresponding β-molecular orbitals are depicted in Figure S44. Orbital energies relative to the HOMO are given in eV.

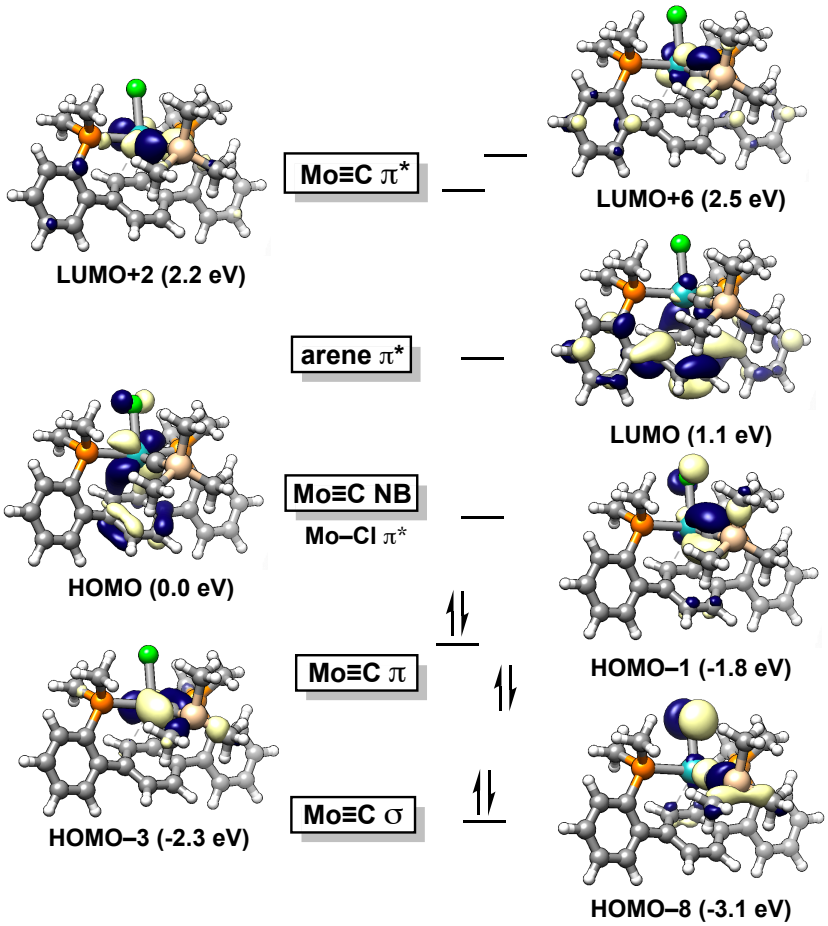

Figure S47—Qualitative MO diagram for **[4][BAr$^{F}_{4}$]** depicting only the β-molecular orbitals with isosurfaces at the 0.05 e^{-} $Å^{-3}$ level. Orbital energies relative to the HOMO are given in eV.

Expectation values of total spin, <S^2>

Table S3—Expectation values of total spin for open-shell carbide and carbyne complexes

Complex	<S^2>
[K][1]	0.7530
[1][BAr$^{F}_{4}$]	0.7554
[2][BAr$^{F}_{4}$]	0.7570
[3][BAr$^{F}_{4}$]	0.7564
[4][BAr$^{F}_{4}$]	0.7579

Cartesian Coordinates of DFT-Optimized Structures

Calculated Structure: [1][BAr$^{F}_{4}$]

Mo	0.00001743813280	-0.88841210000712	-0.44210506804316
P	-2.51773659219082	-1.11773516046169	0.02139602368151
P	2.51774034742371	-1.11778388118129	0.02120326770065
C	-3.51440704042076	0.43568674384183	-0.08474395960975
C	1.41780031431000	1.82984107395487	-0.00355095502626
C	3.51439856192696	0.43564988179348	-0.08486945252532
C	5.69536007101099	1.51936718886674	-0.05882096046152
H	6.78232843198124	1.44234771938675	-0.10025317833813
C	0.69991544051734	2.40424825621979	1.05758618305267
H	1.24239501173389	2.79657369440234	1.91909374904148
C	-4.91576150764980	0.36427865672700	-0.13049726456972
H	-5.41543726038117	-0.60225871576593	-0.20868598671649
C	-0.69988759914915	2.40426889044632	1.05759480191662
H	-1.24234315594327	2.79661814359745	1.91910686986288
C	0.70580740893464	1.36860088194162	-1.14464606409361
H	1.25105094358853	1.13699588045506	-2.05974446488060
C	-0.70583793130957	1.36858987858003	-1.14462278987071
H	-1.25110304629099	1.13699230975781	-2.05971016883158
C	5.08097672854068	2.76594004714128	0.08132328618393
H	5.68458434644806	3.67193302342694	0.14418772743829
C	-2.89313352316078	1.70235530092801	0.02355811887099
C	3.69041100886086	2.85476959825933	0.12703970714169
H	3.20772269107611	3.83019081728063	0.20676189112242
C	4.91575337784793	0.36424401215173	-0.13064562110839
H	5.41542500703603	-0.60229192735439	-0.20887921224237
C	2.89313105432118	1.70231470060657	0.02349818787285
C	-1.41780280626993	1.82986982795000	-0.00352313860906
C	-3.69041025888180	2.85481490254981	0.12706394861825
H	-3.20771918368253	3.83023878548268	0.20673769264930
C	-5.08097691550460	2.76598437979937	0.08137404806266
H	-5.68458300244220	3.67198034847765	0.14421056744113
C	-5.69536461331641	1.51940727229863	-0.05870963596998
H	-6.78233372799711	1.44238883228194	-0.10012423215962
C	-0.00005792007105	-2.75774932949966	0.34022448151079
O	-0.00001806200272	-3.85151486553281	0.71430764892766
C	-0.00003946006206	-1.66569104611243	-1.98490681479049
C	-2.94805323807756	-1.73014255346946	1.70311955590140
H	-2.51632352482430	-2.72864302893729	1.85353959408360
H	-2.53743645675450	-1.05115000368486	2.46156395531816
H	-4.03773163419380	-1.78604709650496	1.82852467563785
C	-3.33941808357302	-2.30855979472108	-1.10041797700403
H	-4.39965366416030	-2.44974918348018	-0.85253432959600
H	-3.23759053348184	-1.95745594193907	-2.13440572875493
H	-2.82277906934086	-3.27346388299809	-1.01628621417402
C	2.94811875040138	-1.73032772767518	1.70286275469889
H	2.53749688191648	-1.05141417108967	2.46137516097157
H	2.51640400373489	-2.72884867815224	1.85318941589346
H	4.03779835194348	-1.78623004787924	1.82825590035645

C	3.33939005734538	-2.30851911485889	-1.10072802495915
H	3.23753408213458	-1.95733737006840	-2.13468657736406
H	4.39963270662133	-2.44972933329475	-0.85288742045635
H	2.82274679334446	-3.27342609393697	-1.01665397380183

Calculated Structure: [K][1]

Mo	-0.00003629215258	-1.04337786968776	0.22167640589675
P	-2.50731189042098	-1.13059263454822	0.06862805422180
P	2.50727783662627	-1.13061289954719	0.06867092274614
C	-3.51923129472049	0.41406027032173	0.04469068199613
C	1.44628999572063	1.83055181435173	-0.23822483405061
C	3.51921175996564	0.41402923158546	0.04452472862378
C	5.69758542998512	1.49908452872376	0.35780268869294
H	6.77827847224749	1.41645648896138	0.48726692984018
C	0.69533013341955	2.85649681729346	0.38649406490847
H	1.21901262076333	3.60051829312579	0.99108611372676
C	-4.90862693423098	0.35290052194690	0.22792646418654
H	-5.39828698020328	-0.62261274294317	0.28762108777062
C	-0.69531222850531	2.85649994242127	0.38652295217978
H	-1.21895686012214	3.60052813128511	0.99114231905102
C	0.70891359642577	0.88984835293688	-1.06472121439350
H	1.22776111871755	0.44347325778073	-1.91670640493804
C	-0.70898390402044	0.88985433523196	-1.06469642633388
H	-1.22786455432356	0.44355669374391	-1.91670310668059
C	5.06586312871965	2.75669428758300	0.32786163275783
H	5.65779917943492	3.66987466926631	0.43190469412231
C	-2.87287749950730	1.69590349903606	-0.03059403710700
C	3.69523549844341	2.84685888456077	0.14486797859060
H	3.22589483237133	3.83118072418866	0.08586483660373
C	4.90862836801544	0.35286262186108	0.22757991250589
H	5.39828839462082	-0.62265397281224	0.28722504834847
C	2.87286133194087	1.69587473010828	-0.03074455756695
C	-1.44631588163293	1.83057048998345	-0.23816142050015
C	-3.69522444476189	2.84689010984615	0.14511787148867
H	-3.22588153206885	3.83120831831311	0.08607624722142
C	-5.06582955697406	2.75673693888783	0.32827147818663
H	-5.65775618616999	3.66991310438782	0.43239813397511
C	-5.69755418953053	1.49912828458648	0.35828029298179
H	-6.77823102198799	1.41649992145773	0.48788759756163
C	0.00004384122309	-1.97630071448498	1.97589442324425
O	0.00036022172006	-2.53039197753668	3.01209732533313
C	-0.00005888640397	-2.53253852417444	-0.69963447001772
C	-3.38878683376696	-2.20141188693527	1.29642932533666
H	-2.85922189403748	-3.16335760990584	1.32341177423193
H	-3.31786515860864	-1.74143944186270	2.29064858773863
H	-4.44572779148357	-2.37725896272336	1.04917366692139
C	-3.04008053274043	-1.94977190019954	-1.50204582450402
H	-4.13660850242662	-2.01501304353120	-1.57133682631970
H	-2.65882700768605	-1.37814514127263	-2.35804973997229
H	-2.57968432392243	-2.94693926528762	-1.53116277223858
C	3.38874435797023	-2.20125024572299	1.29666453863252

H	3.31745638515228	-1.74127399317656	2.29085433188323
H	2.85946028593647	-3.16335075838651	1.32360649556588
H	4.44577879014436	-2.37679638733818	1.04964236614188
C	3.04004636710776	-1.95001682706093	-1.50190006638385
H	2.65897472139027	-1.37836757077265	-2.35796978689903
H	4.13656488311434	-2.01546368503400	-1.57108229244535
H	2.57948063123279	-2.94710720883211	-1.53101819286322

Calculated Structure: [2][BAr$^{F}_{4}$]

Mo	-8.77154160712932	-4.12209465050665	-3.67306011230283
P	-9.23978202926913	-2.58253583763355	-1.62701304372685
P	-8.62543017195726	-5.75526431502938	-5.69613081842209
Cl	-7.76039102955745	-2.36048494185357	-4.89489793398782
O	-10.45855828866222	-6.38968199406614	-2.16076656333711
C	-11.10372178004900	-2.65811464095054	-4.27436146754339
H	-10.56476817020421	-1.71028481022134	-4.24841912661586
C	-11.69277110286931	-4.69934975811303	-5.47864877241449
C	-11.39065371332634	-5.66384850576587	-6.55784640944108
C	-10.07226047153406	-6.13144268912542	-6.78839905183596
C	-10.93820083176521	-3.51137882365119	-5.37064688092094
H	-10.27269008035340	-3.21546346217704	-6.18245468704226
C	-12.43320547388886	-6.12503888086352	-7.38141769939640
H	-13.44408912932232	-5.75360765571477	-7.20561220865228
C	-11.01294507260442	-1.02190279621022	-0.15188678796414
H	-10.12786981710594	-0.78286003368218	0.44001711928892
C	-12.19043312258001	-7.00537515975639	-8.43261595924518
H	-13.01332038011134	-7.33601652064120	-9.06719526352048
C	-9.84794630326008	-7.02172004249887	-7.85478058373312
H	-8.84351205212773	-7.39966461700125	-8.05260916770380
C	-10.90401440339322	-1.84646860327521	-1.28689373799751
C	-12.69315042488569	-4.93689553051760	-4.52618444199732
H	-13.30417012443089	-5.83791456845920	-4.60157662401938
C	-10.88898642155617	-7.44973484147286	-8.67679011643327
H	-10.68279875400559	-8.13222502036239	-9.50180751009184
C	-12.02867667062845	-2.96815665395654	-3.25413949013569
C	-12.85867864734948	-4.08379293328805	-3.42998580234101
H	-13.59664590705436	-4.33066441768621	-2.66491822879631
C	-12.23961990460040	-0.49745949956894	0.25166824660225
H	-12.29119930900335	0.14691205574396	1.12973740642934
C	-13.39501635382991	-0.80728819250817	-0.46937376097557
H	-14.36071043094771	-0.40536778404939	-0.16119189311502
C	-9.90746619234176	-5.55297829837180	-2.72968740950378
C	-13.30827054155412	-1.62250919622785	-1.59492379591396
H	-14.20457124622817	-1.84298860658502	-2.17696298743086
C	-12.07505131552938	-2.13970101480188	-2.03030537239879
C	-7.43765042722337	-4.92447317537160	-2.84612934167093
H	-6.65216217654787	-5.46577057218306	-2.30654486275222
C	-8.83739941733815	-3.42449481102350	-0.04412964571662
H	-9.50210906968787	-4.28549702854601	0.10034113649528
H	-7.79993579960240	-3.78015262746286	-0.08757728404702
H	-8.95137743914507	-2.74243498707094	0.80831517784170

C	-8.06618975038291	-7.42588161485439	-5.17418164910284
H	-8.81179936072785	-7.87798067200959	-4.50806858469482
H	-7.92027137660732	-8.08394502585025	-6.04048409371322
H	-7.11796452121445	-7.32660703576841	-4.63039189497834
C	-7.30875365210001	-5.20323830478707	-6.85008650793611
H	-7.14628963112856	-5.94285590411737	-7.64534734757431
H	-7.58916222417221	-4.23985436122178	-7.29223270005687
H	-6.37942239649864	-5.06347935400683	-6.28325173855738
C	-8.09708986913585	-1.14583857090951	-1.65081762908866
H	-8.19399704528512	-0.55048262551263	-0.73322493749468
H	-7.06784856336079	-1.51589894317408	-1.74150045510436
H	-8.31446000482522	-0.51875114528085	-2.52360670521277

Calculated Structure: [3][BAr$^{F}_{4}$]

Mo	2.60851649506000	7.54470446781656	8.62243118929533
Cl	0.70004192166491	6.87206099515831	9.86635826953570
P	3.16064184861737	9.46413970206901	10.30744579789129
P	2.45726041013319	5.45389636530909	7.06178895771662
Si	1.13619982467841	9.79074644142336	6.12353442239806
O	5.39408284089792	8.22085901272985	7.18814987584953
C	5.19149228464455	7.00758121184514	10.97767744634288
C	3.93700270271284	6.36739550627589	10.92563731610637
H	3.14112762719581	6.67639109124008	11.60396905636991
C	3.72662749200565	5.27891618598765	10.07561338206411
H	2.76824283652071	4.75969852377983	10.09890506646339
C	4.76460186562831	4.80189940454306	9.25102989275331
C	6.03901897534708	5.37095233941570	9.38680821010442
H	6.86120156387011	5.00166762448197	8.77188401934755
C	6.24962774118080	6.45890475195613	10.23868423914080
H	7.23419323868933	6.92734095192556	10.27925326221191
C	5.34602014977454	8.24198467562090	11.77562076338737
C	4.45728633950935	9.33597723095772	11.62729272172370
C	4.62656152602906	10.46040449842014	12.45631750520035
H	3.95741866198404	11.31728787769187	12.36486618136030
C	5.64729538361331	10.52010653580023	13.40357956812472
H	5.74664973563758	11.40097863727761	14.03816065915243
C	6.53964931924557	9.45262533545198	13.52656558326268
H	7.34500965133357	9.48972801224541	14.26053589241411
C	6.38688531627550	8.32989969580675	12.71740361657067
H	7.06177165407848	7.48039736959580	12.83237819601208
C	4.47452536279308	3.74841966785492	8.25525484556465
C	3.42094130265873	3.89041338172805	7.31908676772212
C	3.16115343725029	2.83170880240551	6.42934498528043
H	2.35957856392894	2.91403237691103	5.69390252011231
C	3.91826485580925	1.66141518808839	6.45044894411899
H	3.68585233102216	0.85363063367930	5.75617730539416
C	4.97373129700602	1.53610060876062	7.35656759027000
H	5.57616861727217	0.62763373569857	7.37795341671388
C	5.24620514789063	2.57307856611590	8.24517787910452
H	6.05037820950960	2.46876368251487	8.97508163798799
C	4.42094512742063	7.94299904991578	7.74125088328492

C	1.94207888801728	8.64429500371951	7.40691169077059
C	0.16058446177766	8.75367158353511	4.88885136555889
H	-0.44473277656645	9.43354380749272	4.26890211231196
H	-0.53321452576861	8.06004470489353	5.38323663887097
H	0.80566604100299	8.18407192275546	4.20616210814036
C	-0.03456141907235	10.92936941412738	7.06262813729096
H	-0.49257880766542	11.64096153941620	6.35848934470628
H	0.47918770939527	11.51641630378118	7.83617355364283
H	-0.84632926287102	10.36573513726726	7.54303438248716
C	2.49155839349060	10.75567400641435	5.24006986164210
H	3.29370326846450	10.10257114678642	4.87019752989317
H	2.94288540478026	11.52589084087538	5.88024081981796
H	2.05358881028428	11.26856890824892	4.36972606135383
C	0.70874372997324	4.90368162293471	6.95981040175842
H	0.37602232236621	4.56875457238423	7.94951101754310
H	0.09025641840085	5.76009637107204	6.66330208247609
H	0.58468091636859	4.09288665715493	6.23029025784467
C	2.89098863091977	5.86531083057509	5.32399970208363
H	3.95540009052189	6.12650808215101	5.26495727064571
H	2.69950655652274	5.01559471344235	4.65605258276189
H	2.29578222164848	6.72793155123800	5.00229734403232
C	1.63768143292781	9.95052418473724	11.21042882371551
H	0.86109414309341	10.20179849238060	10.47676654045447
H	1.28039120887395	9.10318034250238	11.80752929097269
H	1.82039964062659	10.81504844493069	11.86207607760447
C	3.65797415892043	11.00702112315968	9.44009205978070
H	3.76915081094601	11.84235214615144	10.14312935864973
H	4.61539283678188	10.84655995886152	8.92816245085506
H	2.89552703694962	11.25519644851204	8.69183326598090

Calculated Structure: [4][BAr$^{F}_{4}$]

Mo	1.71744658822197	9.89419534258960	11.72367451772919
P	1.48427289346082	11.41312239764665	9.67240217100304
P	1.44694411958341	8.18040135223116	13.60847422174878
Cl	0.99558985798024	8.16374634952699	10.29525158771680
Si	5.33781676494715	9.69710948361188	11.59963687673973
C	2.21674308871754	13.75727492419220	11.15842883465578
C	2.13585812523029	12.95413359336090	12.39096791006492
C	1.04484844658445	11.13722018624602	13.65880682739701
H	0.10803597580668	10.65284160262216	13.94394838950410
C	1.87126384046111	8.73374894721636	15.31771008628831
C	2.60406287939366	15.10911675305713	11.22871428242313
H	2.81714729290112	15.54817235636844	12.20452334805653
C	2.12239099667697	11.13908127498279	14.59859500372550
C	3.08833779336224	13.04335993452106	13.41224772045646
H	3.90407004335139	13.76160277276951	13.32020701213499
C	2.18910488382187	10.08413964083624	15.62490539988928
C	1.05184810714115	12.03797688353150	12.56256144184722
H	0.12066202224683	12.22843716220107	12.02379487900574
C	1.90944848158789	13.19624532421571	9.88981235462993
C	3.08193389372173	12.15240335057412	14.49540823782558

H	3.89333190970959	12.19579015873568	15.22311154241591
C	2.57347867153617	10.41044814041473	16.93953761488916
H	2.79439177938318	11.45074831238715	17.18315644312786
C	2.67313088625532	15.90194493331073	10.08643445886091
H	2.96096507031570	16.95048899897499	10.16941934391826
C	2.36115242225550	15.35349797119831	8.83991367098993
H	2.40923796206189	15.96604660272537	7.93905327083087
C	3.45942988341889	9.88498255115089	11.73387066017594
C	1.98897332473067	14.01215805095148	8.74959419749804
H	1.76519374955528	13.59767316622383	7.76516555763787
C	1.93828041409171	7.77170664520928	16.33851147479652
H	1.70663132889743	6.72775313139982	16.12077847659731
C	5.71416149914076	8.31965303988064	10.37560604624251
H	5.27992242837615	7.36238519605405	10.69585399371323
H	6.80311719790855	8.18320608809169	10.28750634905960
H	5.32250085215592	8.54708496995712	9.37439057000319
C	2.62999355999332	9.44194825844218	17.93802167210661
H	2.91587333887361	9.72307938806910	18.95213030264932
C	6.04219089758601	11.34101004945673	11.00781465490649
H	5.65975359108288	11.62077192539150	10.01625620634179
H	7.13810407987078	11.26807280958686	10.93219309142789
H	5.80815227608994	12.15710602074620	11.70538793523714
C	2.30798188932405	8.11580426410743	17.63882076297331
H	2.34632906944450	7.34954763834636	18.41371230591300
C	5.99877655236397	9.27854075520216	13.31353976808278
H	5.73651131063446	10.05035552818315	14.05040550926768
H	7.09678915060081	9.20621863928365	13.27876681451252
H	5.61639141514239	8.31515465776068	13.67876295242423
C	-0.23629185514223	11.44281667710138	9.02032123752135
H	-0.93038200488470	11.82713144653990	9.77927064904766
H	-0.30729127478466	12.07998572925805	8.12835211784738
H	-0.52815429543206	10.41614559541132	8.76123592660796
C	2.46193877866126	10.85699077976939	8.22498568997645
H	3.53102570737273	10.96400500035286	8.44440785637948
H	2.23866979011385	9.79425673882112	8.06132581217210
H	2.21616505910711	11.42179728294093	7.31628267662138
C	2.39814803654560	6.63515701204387	13.34973137422815
H	3.47100827243221	6.85221069865153	13.41548023751504
H	2.13553427613145	5.85906041490489	14.08036661326716
H	2.17191086704311	6.27087120606907	12.33873141120289
C	-0.28564578533578	7.57675278448566	13.75355181977761
H	-0.57919987449614	7.12720514633019	12.79535478336184
H	-0.37524656687705	6.82788235713984	14.55214355133590
H	-0.96676173645267	8.40822360663682	13.97767149369571

CRYSTALLOGRAPHIC INFORMATION

Supplementary crystallographic data for this paper can be obtained free of charge from the Cambridge Crystallographic Data Centre via www.ccdc.cam.ac.uk/data_request/cif (deposition numbers listed in Table S3 below).

Crystallographic and refinement Details

Crystals were mounted on a MiTeGen loop using Paratone oil, and then placed on the diffractometer under a nitrogen stream. Low-temperature diffraction data (ϕ-and ω-scans) were collected on a Bruker AXS KAPPA APEX II diffractometer coupled to an PHOTON 100 CMOS detector with graphite monochromated Mo K_α radiation (λ = 0.71073 Å) for the structure of **[K][1]** and on a Bruker AXS D8 VENTURE KAPPA diffractometer coupled to a PHOTON II CPAD detector with Mo K_α radiation (λ = 0.71073 Å) or Cu K_α radiation (λ = 1.54178 Å) from an IμS micro-source for the structure of **[2][BAr$^F_4$]–[4][BAr$^F_4$]**. Data collection, integration, and scaling were carried out using the Bruker APEXIII software.[12] Absorption corrections were applied using SADABS.[13] Space groups were determined on the basis of systematic absences and intensity statistics. Structures were solved in the Olex^2 software interface[14] by intrinsic phasing using SHELXT (incorporated into SHELXTL)[15] and refined to convergence. Unless otherwise indicated, all hydrogen atoms were included into the model at geometrically calculated positions and refined using a riding model. Graphical representations of structures were generated using the Diamond 3 visualization software.[16]

Details for [K][1]: Brown, single crystalline blocks of **[K][1]** (0.40x0.35x0.15 mm) were grown by slow mixing of pentane layered onto a 2-MeTHF solution at –40 °C. **[K][1]** crystallized in the monoclinic space group *C*2/*c* with two molecules in the asymmetric unit along with two molecules of 2-MeTHF. One K^+ cation was encapsulated by a crown ether that was disordered over two positions (87:13 ratio) and a molecule of 2-MeTHF that had a single atom disordered over two positions (82:18 ratio). The other K^+ cation was encapsulated by a non-disordered crown ether and a molecule of 2-MeTHF that was disordered over two positions (62:38 ratio). The remaining two molecules of free (unbound) 2-MeTHF were disordered over two or three positions, respectively (63:36 or 48:32:20 ratios). Disordered atoms were refined with the help of similarity restraints on the 1,2- and 1,3-distances and displacement parameters (SIMU command in Olex^2) as well as enhanced rigid bond restraints for anisotropic displacement parameters (RIGU). Additionally, the sum of the occupation factors for the triply-disordered 2-MeTHF molecule was confined to unity using the SUMP command.

Details for [2][BAr$^F_4$]: Dichroic yellow-green, single-crystalline blocks of **[2][BAr$^F_4$]** (0.16x0.1x0.09 mm) were grown by vapor diffusion of hexanes into solutions in THF at –40 °C. **[2][BAr$^F_4$]** crystallized in the monoclinic space group $\underline{P}2_1$ with one molecule in the asymmetric unit. All hydrogen atoms were included into the model at geometrically calculated positions and refined using a riding model, except the methylidyne H atom, which was located in the electron difference density map and refined freely.

Details for [3][BAr$^F_4$]: Small brown, single-crystalline blades of **[3][BAr$^F_4$]** (0.25x0.06x0.02 mm) were grown via vapor diffusion of pentane into a saturated ether solution of **[3][BAr$^F_4$]** at –40 °C. The crystals were unstable to degradation under the collection conditions, preventing collection of a full dataset. Even after refining to convergence, and despite the presence of high-angle data (d_{min} 0.79), the dataset was of insufficient quality to allow for refinement of a high-quality structure. The refined model is nevertheless

of sufficient quality to confirm the atom connectivity of **[3][BAr$^{F}_{4}$]**, though it should be considered unreliable for the inference of bond metrics.

[3][BAr$^{F}_{4}$] crystallized in the triclinic space group $\underline{P}\bar{1}$ with four molecules in the asymmetric unit. Two of the four [BAr$^{F}_{4}$]$^{-}$ counterions were refined with the help of similarity restraints on several of the anisotropic displacement parameters for the arene carbon atoms, as executed by the SIMU command in Olex^{2}.

Details for [4][BAr$^{F}_{4}$]: Single crystalline red blocks of **[4][BAr$^{F}_{4}$]** (0.24x0.15x0.09 mm) were grown via vapor diffusion of pentane into a saturated diethyl ether solution of **[4][BAr$^{F}_{4}$]** at –40°C. **[4][BAr$^{F}_{4}$]** crystallized in the triclinic space group P_c with two molecules in the asymmetric unit. The crystal used for **[4][BAr$^{F}_{4}$]** was twinned. The twin components were separated and assigned using Olex^{2}. The crystal structure for **[4][BAr$^{F}_{4}$]** was refined with racemic twinning as applied using a TWIN law with a batch scale factor (BASF) of 0.48.

One of the two molecules of **[4][BAr$^{F}_{4}$]** in the asymmetric unit is disordered with the Mo(IV) carbyne [P2Mo(≡CSiMe$_3$)(CO)][BAr$^{F}_{4}$], which has an identical structure except that a CO ligand replaces the Cl ligand in **[4][BAr$^{F}_{4}$]**. The disordered groups were satisfactorily modelled in a 60:40 ratio and refined with the help of similarity restraints for the CO atoms, as executed by the SIMU command in Olex^{2}. Over the two molecules in the asymmetric unit (one of which exhibits no disorder), the total carbonyl ligand occupancy is 80%; thus, the total ratio of **[4][BAr$^{F}_{4}$]**:[P2Mo(≡CSiMe$_3$)(CO)][BAr$^{F}_{4}$] in the crystal is 80:20.

Details for [K][6]: Single crystalline brown blocks of **[K][6]** were grown via vapor diffusion of pentane into the reaction mixture in THF at –40°C. **[K][6]** crystallized in the orthorhombic space group C222$_1$.

Details for [K]$_6$[1]$_2$[5]: Crystalline brown blocks of **[K]$_6$[1]$_2$[5]** were grown via layering of pentane into the reaction mixture in THF at –40°C. The space group identified was $P_{\bar{1}}$. Unfortunately, crystals grown by this method were reproducibly polycrystalline. While analysis of data subsets enabled determination of atom connectivity, the overall quality was insufficient for reliable determination of bond metrics.

Table S4—Crystal and refinement data for open-shell carbide and carbyne complexes.

	[K][1]	[2][BAr$^F_4$]	[3][BAr$^F_4$]	[4][BAr$^F_4$]
CCDC Number	2076055	2076057	2076058	2076060
Empirical formula	$C_{108}H_{168}K_2Mo_2O_{18}P_4$	$C_{64}H_{53}BClF_{24}MoOP_2$	$C_{67}H_{61}BClF_{24}MoOP_2Si$	$C_{66.2}H_{61}BCl_{0.8}O_{0.2}P_2Si$
Formula weight	2148.37	1498.20	1570.38	1540.90
T (K)	100	100	100	100
***a*, Å**	33.715(7)	12.3780(18)	17.5768(17)	18.608(4)
***b*, Å**	13.023(3)	17.656(3)	21.819(4)	18.995(7)
***c*, Å**	52.537(12)	14.650(2)	35.488(4)	19.316(5)
α, °	90	90	88.536(7)	90
β, °	107.154(10)	92.396(1)	89.560(6)	101.144(9)
γ, °	90	90	89.499(11)	90
Volume, Å^3	22041(8)	3198.9(9)	13604(3)	6699(3)
Z	8	2	8	4
Crystal system	monoclinic	monoclinic	triclinic	monoclinic
Space group	*C*2/c	*P*2$_1$	*P*$\bar{1}$	*P$_c$*
***d*$_{calc}$, g/cm^3**	1.295	1.555	1.533	1.528
2θ range, °	1.622 to 59.808	4.614 to 74.508	4.052 to 152.062	4.564 to to 73.654
***μ*, mm^{-1}**	0.424	0.409	3.524	0.402
GooF	1.357	1.067	1.092	1.045
***R*$_1$,^{a} *wR*$_2$ ^{b} [I>2 σ(I)]**	0.0955, 0.1862	0.0382, 0.0871	0.1431, 0.3113	0.0615, 0.1565
Radiation Type	Mo-Kα	Mo-Kα	Cu-Kα	Mo-Kα

[a] $R_1 = \sum||F_o| - |F_c||/\sum|F_o|$. [b] $wR_2 = [\sum[w(F_o^2-F_c^2)^2]/\sum[w(F_o^2)^2]]^{1/2}$

Table S5—Crystal and refinement data for C–C coupled products.

	[K][6]	[K]$_6$[1]$_2$[5]
CCDC Number	2091130	N/A
Empirical formula	$C_{36}H_{48}K_{0.5}MoO_2P_2$	$C_{39.5}K_{1.5}MoO_{2.5}P_2$
Formula weight	690.99	731.92
T (K)	100	100
***a*, Å**	13.232(3)	17.757(5)
***b*, Å**	24.039(6)	20.221(5)
***c*, Å**	22.7625(14)	25.354(6)
α, °	90	99.024(18)
β, °	90	103.06(2)
γ, °	90	100.688(18)
Volume, Å^3	7240(3)	8524(4)
Z	8	8
Crystal system	orthorhombic	triclinic
Space group	*C*222$_1$	P-1
***d*$_{calc}$, g/cm^3**	1.268	1.141
2θ range, °	7.354 to 161.902	4.546 to 146.004
***μ*, mm^{-1}**	4.348	4.770
GooF	1.275	1.083
***R*$_1$,^{a} *wR*$_2$ ^{b} [I>2 σ(I)]**	0.0388, 0.1338	0.1264, 0.3081
Radiation Type	Cu-Kα	Cu-Kα

[a] $R_1 = \sum||F_o| - |F_c||/\sum|F_o|$. [b] $wR_2 = [\sum[w(F_o^2-F_c^2)^2]/\sum[w(F_o^2)^2]]^{1/2}$

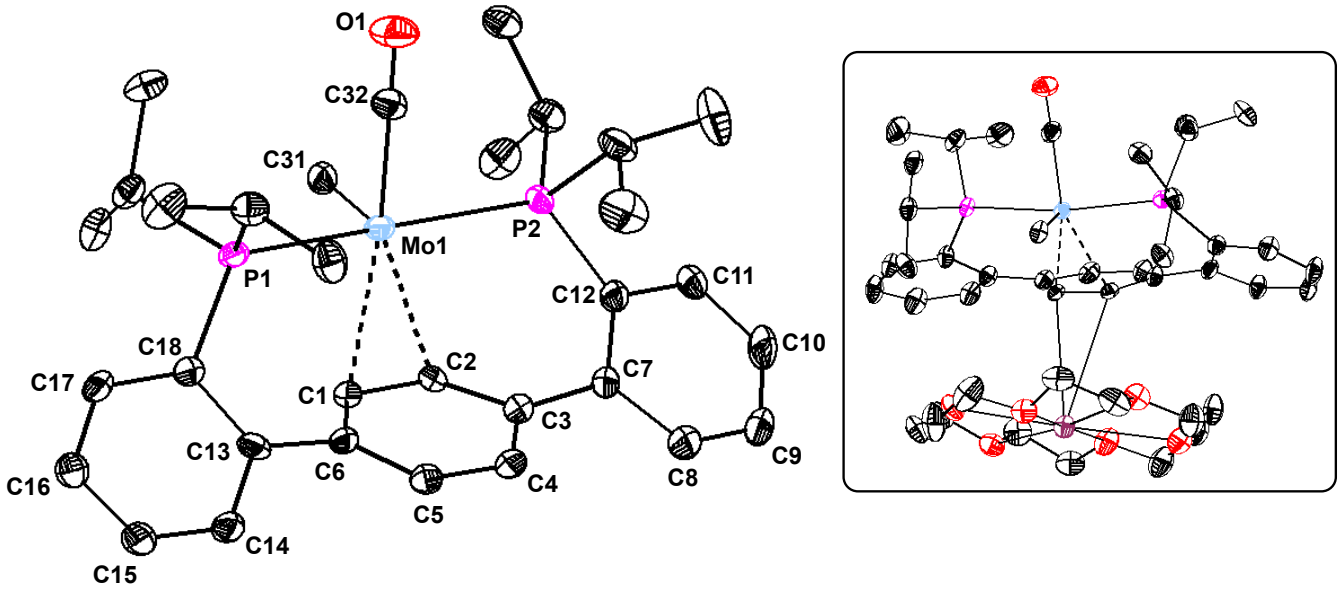

Figure S48—Structural drawing of **[K(18-crown-6)][1]** with anisotropic displacement ellipsoids shown at the 50% probability level. Hydrogen atoms, encapsulated K^+ counterion, and 2-MeTHF solvate molecules are omitted for clarity. Inset, right: Complete structure of **[K(18-crown-6)][1]** showing arene binding to encapsulated K^+ cation. A disordered 2-MeTHF solvates bound to the K^+ cation is omitted for clarity.

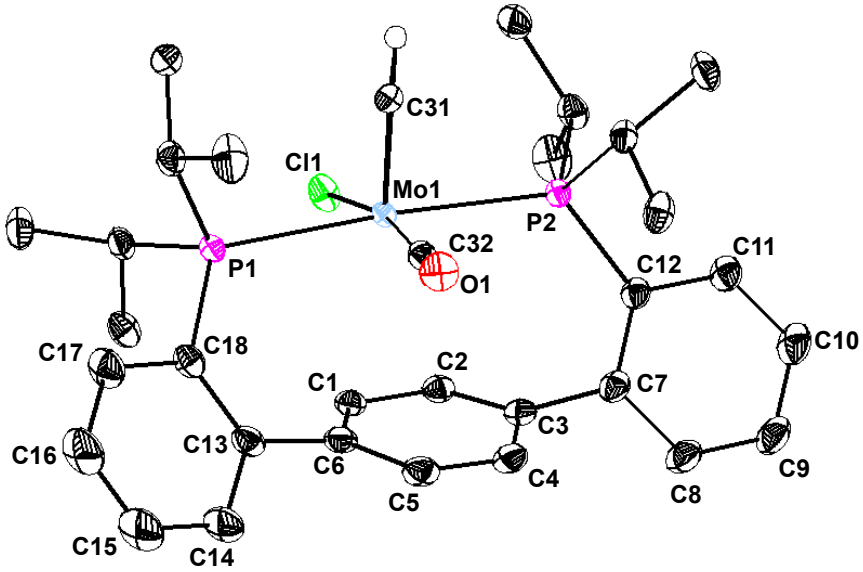

Figure S49—Structural drawing of **[2][BAr$^F_4$]** with anisotropic displacement ellipsoids shown at the 50% probability level. Hydrogen atoms and $[BAr^F_4]^-$ counterion are omitted for clarity, except the methylidyne H atom (H31), which was located in the electron density map and refined freely.

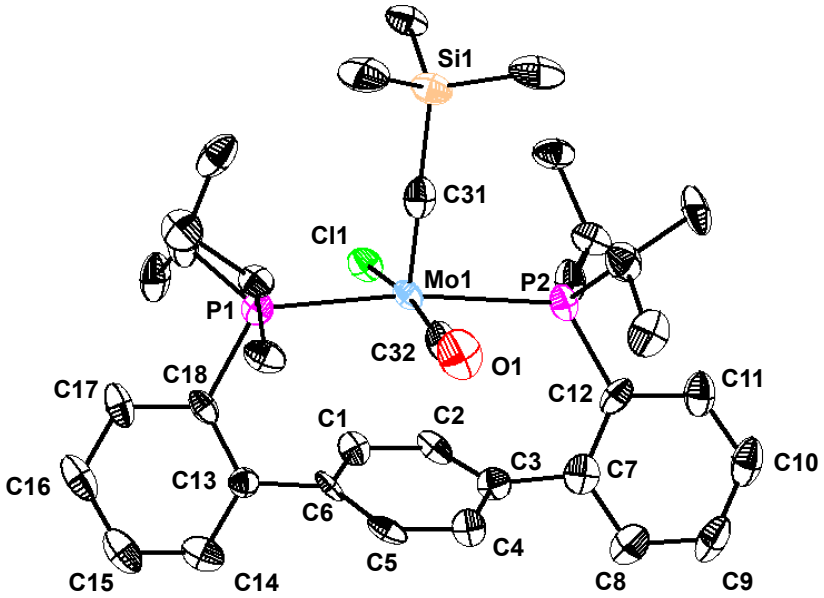

Figure S50—Structural drawing of **[3]**$^{+}$ with anisotropic displacement ellipsoids shown at the 50% probability level. Hydrogen atoms and $[BAr^{F}_{4}]^{-}$ counterion are omitted for clarity.

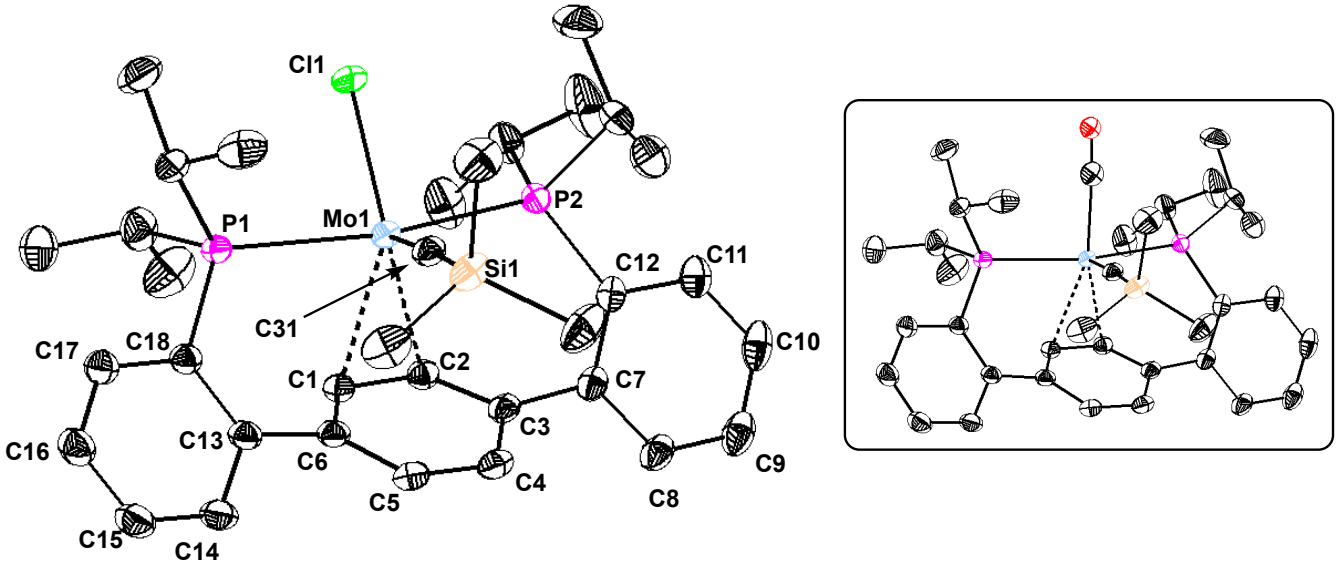

Figure S51—Structural drawing of **[4][BAr$^{F}_{4}$]** with anisotropic displacement ellipsoids shown at the 50% probability level. The structure is disordered with $[P2Mo(CSiMe_3)(CO)]^{+}$ (20%; inset, right). Hydrogen atoms and $[BAr^{F}_{4}]^{-}$ counterions are omitted for clarity.

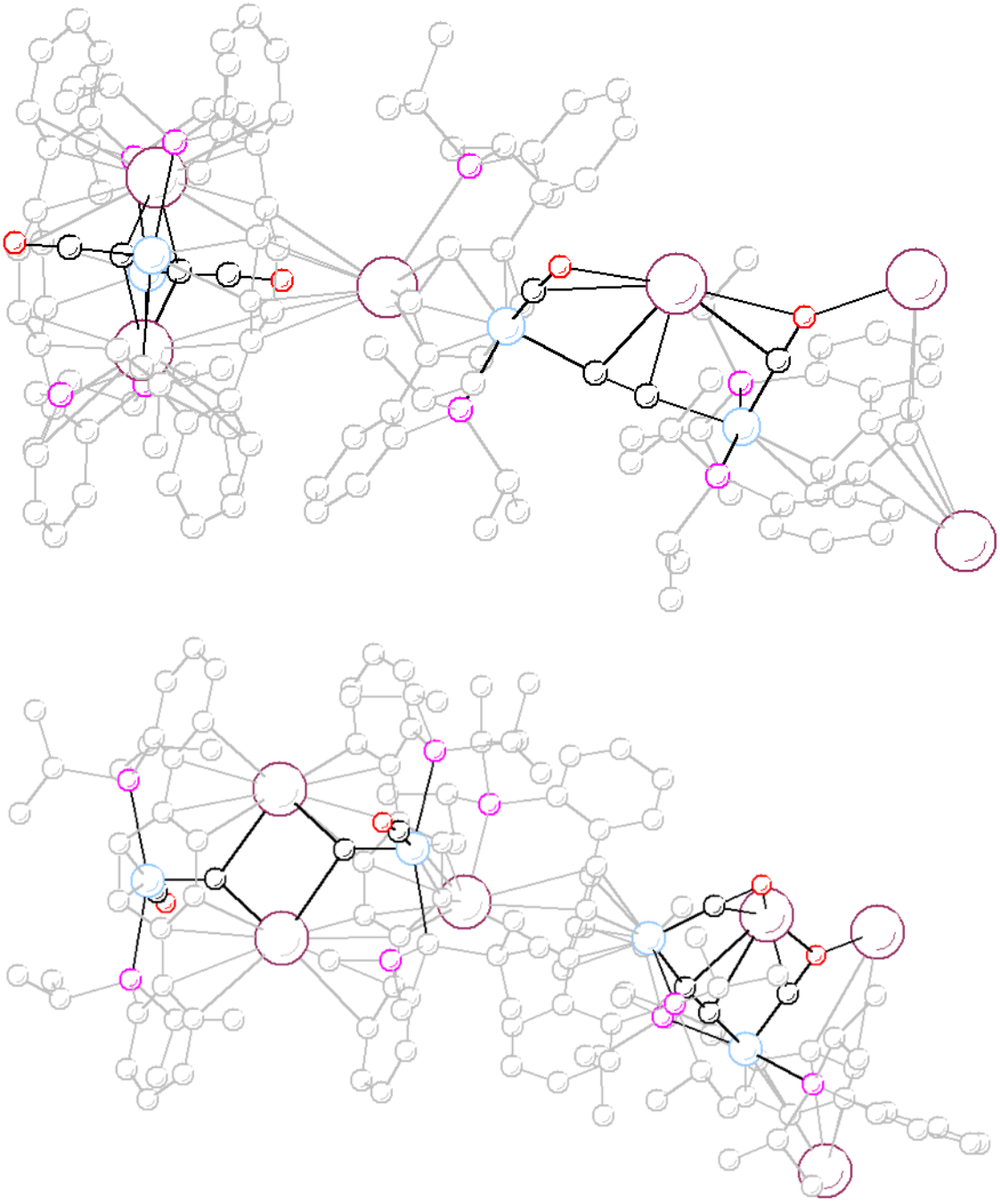

Figure S52—Structural drawing of **[K$_3$][5][1]$_2$** (2-methylTHF solvate) as a ball-and-stick representation. Carbon atoms assigned to carbide, CO, and μ^2-CC ligands in black; all other carbon atoms on the P2 ligand are shown in grey for clarity. Light blue: Mo; pink: P; red: O; purple: K. (Top) Perspective showing μ^2-CC bridge between Mo3 and Mo4. Hydrogen atoms and 2-methyl THF solvate molecules are omitted for clarity. (Bottom) Perspective showing mutually opposing carbide ligands on Mo1 and Mo2 bridged in a C_2K_2 diamond-shaped core.

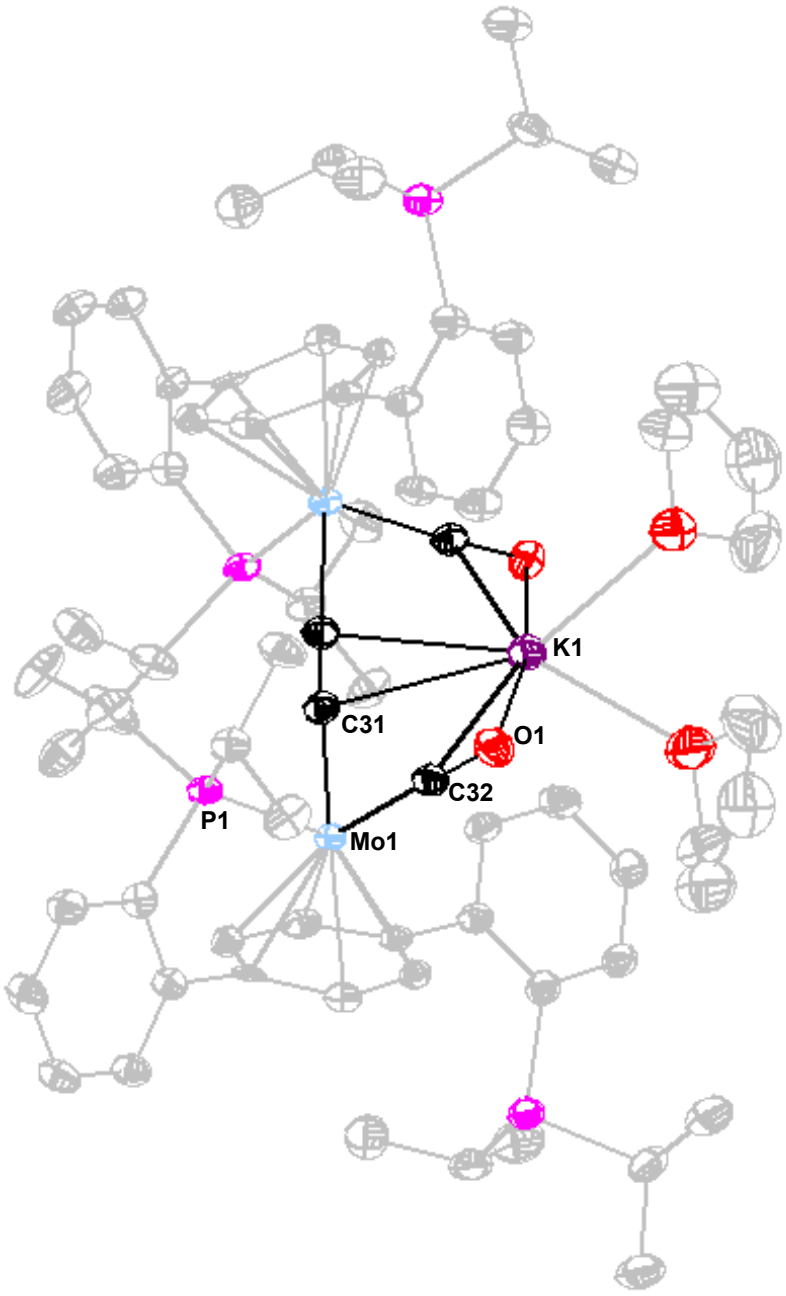

Figure S53—Structural drawing of **[K][6]** with 50% probability anisotropic displacement ellipsoids. Hydrogen atoms are omitted for clarity. All carbon atoms are color in grey except the C–C coupled and CO carbons, which are colored in black for clarity.

Table S6. Key bond lengths (Å) and angles (°) for open-shell complexes [2][BAr$^{F}_{4}$]–[4][BAr$^{F}_{4}$] and [K(18-crown-6)][1], compared with those of previously reported Mo(IV) silylcarbyne and methylidyne complexes 2/2' and 3/3' (Chart S2).

Complex	Mo1–C31	Mo–C32	C32–O1	Mo1–C1	Mo1–C2	C1–C2	Mo1–Cl1	Mo–P$_{avg}$
[2][BAr$^{F}_{4}$]	1.753(2)	2.095(2)	1.128(3)	-	-	-	2.3615(7)	2.605
[4][BAr$^{F}_{4}$]	1.734(9)	-	-	2.423(2)	2.445(6)	1.363(9)	2.355(2)	2.571
[K(18-c-6)[1]	1.739(5)	1.974(6)	1.157(8)	2.444(6)	2.449(5)	1.390(7)	-	2.523
2	1.764(2)	1.930(4)	1.197(6)	-	-		2.526	2.560
3	1.767(2)	1.974(2)	1.138(3)	-	-		2.5380(6)	2.572
2'	1.718(2)	1.972(2)	1.155(2)	2.523(2)	2.526(2)	1.395(1)	2.579(1)	2.567
3'	1.796(1)	1.976(1)	1.158(1)	2.5235(8)	2.5204(7)	1.396(2)	2.5881(4)	2.600

Chart S2–Structures of complexes 2' and 3'.

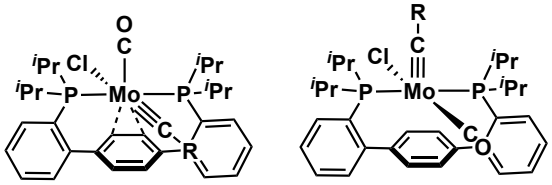

R = H: **2'**; R = SiMe$_3$: **3'** R = H: **2**; R = SiMe$_3$: **3**

Table S7—Key bond lengths for the arene moiety in **[K][1]** relative to comparator complexes: Mo(IV) methylidyne and silylcarbyne complexes **2'** and **3'** (Chart S2).

	Mo1–C1	Mo1–C2	C1–C2	C2–C3	C3–C4	C4–C5	C5–C6
[K][1]	2.444(5)	2.449(5)	1.390(7)	1.445(8)	1.409(7)	1.374(7)	1.408(8)
2'	2.510(2)	2.531(2)	1.396(2)	1.419(2)	1.382(2)	1.407(2)	1.383(2)
3'	2.5235(8)	2.5204(7)	1.395(1)	1.424(1)	1.383(1)	1.407(2)	1.382(1)
[4][BAr$^{F}_{4}$]	2.428(2)	2.439(2)	1.405(3)	1.416(3)	1.396(4)	1.401(4)	1.395(3)
DFT	2.521	2.521	1.424	1.458	1.437	1.404	
	C6–C1	**C3–C7**	**C7–C8**	**C8–C9**	**C9–C10**	**C10–C11**	**C11–C12**
[K][1]	1.446(7)	1.433(7)	1.421(9)	1.359(9)	1.41(1)	1.39(1)	1.403(7)
2	1.426(2)	1.480(2)	1.409(2)	1.402(2)	1.392(2)	1.388(2)	1.390(2)
3'	1.421(1)	1.477(2)	1.404(1)	1.385(2)	1.385(2)	1.391(1)	1.403(2)
[4][BAr$^{F}_{4}$]	1.408(3)	1.477(3)	1.400(3)	1.384(4)	1.381(5)	1.380(4)	1.407(4)
	C12–C7	**C6–C13**	**C13–C14**	**C14–C15**	**C15–C16**	**C16–C17**	**C17–C18**
[K][1]	1.432(8)	1.459(7)	1.416(8)	1.369(9)	1.39(1)	1.388(9)	1.397(8)
2	1.409(2)	1.479(2)	1.403(2)	1.390(2)	1.386(2)	1.390(2)	1.402(2)
3'	1.417(1)	1.475(2)	1.405(1)	1.386(2)	1.391(1)	1.388(2)	1.404(2)
[4][BAr$^{F}_{4}$]	1.404(3)	1.470(3)	1.400(3)	1.390(4)	1.380(4)	1.386(4)	1.409(4)

REFERENCES

1. Pangborn, A. B.; Giardello, M. A.; Grubbs, R. H.; Rosen, R. K.; Timmers, F. J. Safe and convenient procedure for solvent purification. *Organometallics* **1996,** *15* (5), 1518-1520.
2. Buss, J. A.; Bailey, G. A.; Oppenheim, J.; VanderVelde, D. G.; Goddard, W. A.; Agapie, T. CO Coupling Chemistry of a Terminal Mo Carbide: Sequential Addition of Proton, Hydride, and CO Releases Ethenone. *J. Am. Chem. Soc.* **2019,** *141* (39), 15664-15674.
3. Buss, J. A.; Agapie, T. Four-electron deoxygenative reductive coupling of carbon monoxide at a single metal site. *Nature* **2016,** *529* (7584), 72-75.
4. Heinekey, D. M.; Radzewich, C. E. Synthesis and Reactivity of the Cationic Methylene Complex [Cp2ReCH2]+. *Organometallics* **1998,** *17* (1), 51-58.
5. Fulmer, G. R.; Miller, A. J. M.; Sherden, N. H.; Gottlieb, H. E.; Nudelman, A.; Stoltz, B. M.; Bercaw, J. E.; Goldberg, K. I. NMR Chemical Shifts of Trace Impurities: Common Laboratory Solvents, Organics, and Gases in Deuterated Solvents Relevant to the Organometallic Chemist. *Organometallics* **2010,** *29* (9), 2176-2179.
6. Stoll, S.; Schweiger, A. EasySpin, a comprehensive software package for spectral simulation and analysis in EPR. *Journal of Magnetic Resonance* **2006,** *178* (1), 42-55.
7. Gaussian 09, Revision C.01, Frisch, M. J.; Trucks, G. W.; Schlegel, H. B.; Scuseria, G. E.; Robb, M. A.; Cheeseman, J. R.; Scalmani, G.; Barone, V.; Mennucci, B.; Petersson, G. A.; Nakatsuji, H.; Caricato, M.; Li, X.; Hratchian, H. P.; Izmaylov, A. F.; Bloino, J.; Zheng, G.; Sonnenberg, J. L.; Hada, M.; Ehara, M.; Toyota, K.; Fukuda, R.; Hasegawa, J.; Ishida, M.; Nakajima, T.; Honda, Y.; Kitao, O.; Nakai, H.; Vreven, T.; Montgomery, Jr., J. A.; Peralta, J. E.; Ogliaro, F.; Bearpark, M.; Heyd, J. J.; Brothers, E.; Kudin, K. N.; Staroverov, V. N.; Kobayashi, R.; Normand, J.; Raghavachari, K.; Rendell, A.; Burant, J. C.; Iyengar, S. S.; Tomasi, J.; Cossi, M.; Rega, N.; Millam, J. M.; Klene, M.; Knox, J. E.; Cross, J. B.; Bakken, V.; Adamo, C.; Jaramillo, J.; Gomperts, R.; Stratmann, R. E.; Yazyev, O.; Austin, A. J.; Cammi, R.; Pomelli, C.; Ochterski, J. W.; Martin, R. L.; Morokuma, K.; Zakrzewski, V. G.; Voth, G. A.; Salvador, P.; Dannenberg, J. J.; Dapprich, S.; Daniels, A. D.; Farkas, Ö.; Foresman, J. B.; Ortiz, J. V.; Cioslowski, J.; Fox, D. J. Gaussian, Inc., Wallingford CT, 2009.
8. Neese, F. The ORCA program system. *WIREs Computational Molecular Science* **2012,** *2* (1), 73-78.
9. (a) Perdew, J. P.; Ruzsinszky, A.; Csonka, G. I.; Constantin, L. A.; Sun, J. Workhorse Semilocal Density Functional for Condensed Matter Physics and Quantum Chemistry. *Phys. Rev. Lett.* **2009,** *103* (2), 026403. (b) Perdew, J. P.; Ruzsinszky, A.; Csonka, G. I.; Constantin, L. A.; Sun, J. Erratum: Workhorse Semilocal Density Functional for Condensed Matter Physics and Quantum Chemistry [Phys. Rev. Lett. 103, 026403 (2009)]. *Phys. Rev. Lett.* **2011,** *106* (17), 179902.
10. Hanwell, M. D.; Curtis, D. E.; Lonie, D. C.; Vandermeersch, T.; Zurek, E.; Hutchison, G. R. Avogadro: an advanced semantic chemical editor, visualization, and analysis platform. *J. Cheminform.* **2012,** *4* (1), 17.
11. Pettersen, E. F.; Goddard, T. D.; Huang, C. C.; Couch, G. S.; Greenblatt, D. M.; Meng, E. C.; Ferrin, T. E. UCSF Chimera—A visualization system for exploratory research and analysis. *J. Comput. Chem.* **2004,** *25* (13), 1605-1612.
12. APEX3, Version 1 User Manual, M86-EXX229, Bruker Analytical X-ray Systems, Madison, WI, May 2016.
13. Sheldrick, G.M. "SADABS (version 2008/1): Program for Absorption Correction for Data from Area Detector Frames", University of Göttingen, 2008.
14. Dolomanov, O. V.; Bourhis, L. J.; Gildea, R. J.; Howard, J. A. K.; Puschmann, H. OLEX2: a complete structure solution, refinement and analysis program. *J. Appl. Cryst.* **2009,** *42* (2), 339-341.
15. Sheldrick, G. Crystal structure refinement with SHELXL. *Acta Cryst. C* **2015,** *71* (1), 3-8.
16. Brandenburg, K. (1999). DIAMOND. Crystal Impact GbR, Bonn, Germany.